Report No. FHWA-KS-19-01 ▪ FINAL REPORT ▪ September 2019

Strain-Based Fatigue Crack Monitoring of Steel Bridges using Wireless Elastomeric Skin Sensors

Jian Li, Ph.D., P.E.
Caroline Bennett, Ph.D., P.E.
William Collins, Ph.D., P.E.
The University of Kansas

Simon Laflamme, Ph.D.
Iowa State University

Hongki Jo, Ph.D.
The University of Arizona

A Transportation Pooled Fund Study - TPF-5(328)

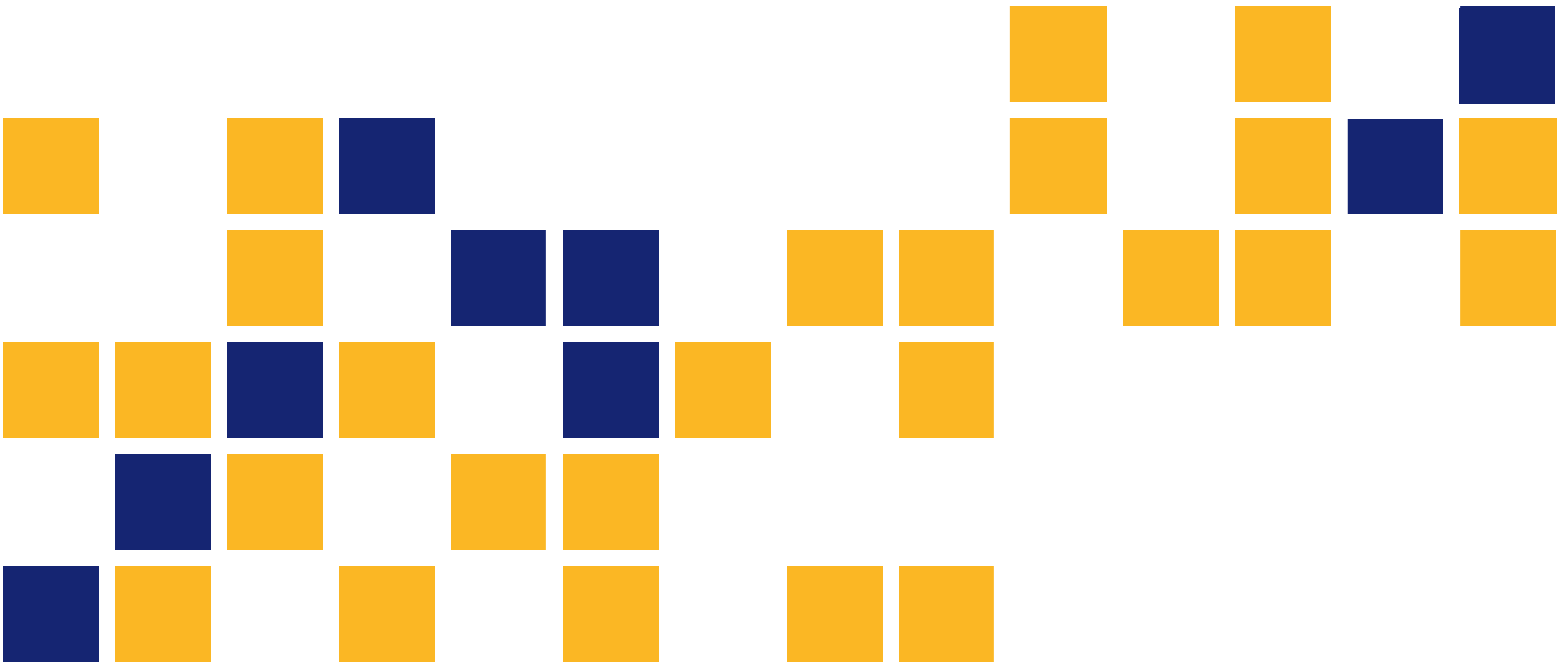

Kansas Department of Transportation

1 Report No. FHWA-KS-19-01	**2 Government Accession No.**	**3 Recipient Catalog No.**
4 Title and Subtitle Strain-Based Fatigue Crack Monitoring of Steel Bridges using Wireless Elastomeric Skin Sensors		**5 Report Date** September 2019 **6 Performing Organization Code**
7 Author(s) Jian Li, Ph.D., P.E., Caroline Bennett, Ph.D., P.E., William Collins, Ph.D., P.E., Simon Laflamme, Ph.D., Hongki Jo, Ph.D.		**8 Performing Organization Report No.**
9 Performing Organization Name and Address The University of Kansas Department of Civil, Environmental & Architectural Engineering 1530 West 15th St Lawrence, Kansas 66045-7609		**10 Work Unit No. (TRAIS)** **11 Contract or Grant No.** C2067
12 Sponsoring Agency Name and Address Kansas Department of Transportation Bureau of Research 2300 SW Van Buren Topeka, Kansas 66611-1195		**13 Type of Report and Period Covered** Final Report September 2015–August 2018 **14 Sponsoring Agency Code** RE-0699-01 TPF-5(328)

15 Supplementary Notes

For more information write to address in block 9.
Pooled Fund Study TPF-5(328) sponsored by the following DOTs: Kansas, Minnesota, North Carolina, Oklahoma, Pennsylvania, and Texas.
Appendices are available separately upon request to KDOT#Research.Library@ks.gov.

16 Abstract

Fatigue cracks that develop in steel highway bridges under repetitive traffic loads are one of the major mechanisms that degrade structural integrity. If bridges are not appropriately inspected and maintained, fatigue cracks can eventually lead to catastrophic failures, in particular for fracture-critical bridges. Bridge owners, such as state Departments of Transportation (DOTs), typically rely on trained bridge inspectors to visually inspect steel bridges for fatigue cracking so that appropriate repairs can be applied before cracks reach critical sizes. However, visual inspections can be prone to error due to inconsistent skills and result interpretation among inspectors. Advanced approaches for detecting and/or monitoring of fatigue cracks have been investigated in both the structural health monitoring (SHM) and nondestructive testing (NDT) communities. An important challenge with the existing methods is their reliance on extensive human operations to collect critical measurements in the field, making it challenging to implement long-term continuous crack monitoring of steel bridges.

In this report, a wireless elastomeric skin sensor is proposed to monitor fatigue cracks in steel bridges. The wireless elastomeric skin sensor consists of three components: (1) a large-area strain-based skin sensor, termed soft elastomeric capacitor (SEC), serving as the fundamental sensing unit for crack monitoring; (2) a newly-developed data acquisition (DAQ) board for measuring the small capacitance change from the SEC under fatigue cracking; and (3) a wireless sensing platform (Xnode) for transferring SEC's signal from the DAQ board to the base station in the field. Validation of the wireless elastomeric skin sensor is completed through several numerical and experimental investigations of the fundamental sensing unit, SEC, for fatigue crack monitoring. We validate the integrated monitoring system through a field deployment on a steel highway bridge.

Compared with the off-the-shelf DAQ system, the newly-developed sensor board can collect SEC measurements with better noise performance. More importantly, the developed sensor board can be integrated with the wireless sensing platform Xnode to transfer the collected SEC signals to the base station through wireless communication. This capability will significantly improve the flexibility of the monitoring system by reducing the cabling work in the field. As a result, the integration of wireless capacitive sensing and the SEC technology enables a wireless elastomeric skin sensor for fatigue sensing of steel bridges.

Data collected in the field showed that, through the trigger-based sensing mechanism, the wireless crack monitoring system was able to collect data continuously and autonomously from the SEC sensors and the strain gauge under the traffic loading. By processing the raw measurements using the proposed algorithm, Crack Growth Indices (CGIs) of each monitored location could be continuously collected and statistically monitored for long-term monitoring of fatigue cracks of steel bridges.

Several further development needs were identified to achieve more robust, accurate, and flexible crack monitoring. First, an improved understanding of the SEC sensor behavior under folded configuration is needed to strategically adjust the CGI algorithm when the SECs are attached to corners and joints. Second, the capacitance sensor board is currently based on analogy circuits, meaning the balancing and shunt calibration are performed manually. Converting the analog circuit to a digital one will enable software control and automation of these processes, hence greatly improving the efficiency and flexibility of the wireless sensing. Third, deployment of the sensor network at more diverse structural configurations and more extensive analyses of long-term field data are necessary to ensure adaptability of the proposed CGI algorithm.

17 Key Words Fatigue Cracking, Structural Health Monitoring, Steel Bridges, Nondestructive Tests		**18 Distribution Statement** No restrictions. This document is available to the public through the National Technical Information Service www.ntis.gov.	
19 Security Classification (of this report) Unclassified	**20 Security Classification (of this page)** Unclassified	**21 No. of pages** 156 + Appendices	**22 Price**

Form DOT F 1700.7 (8-72)

This page intentionally left blank.

Strain-Based Fatigue Crack Monitoring of Steel Bridges using Wireless Elastomeric Skin Sensors

Final Report

Prepared by

Jian Li, Ph.D., P.E.
Caroline Bennett, Ph.D., P.E.
William Collins, Ph.D., P.E.
The University of Kansas

Simon Laflamme, Ph.D.
Iowa State University

Hongki Jo, Ph.D.
The University of Arizona

A Report on Research Sponsored by

THE KANSAS DEPARTMENT OF TRANSPORTATION
TOPEKA, KANSAS

and

THE UNIVERSITY OF KANSAS
LAWRENCE, KANSAS

September 2019

NOTICE

The authors and the state of Kansas do not endorse products or manufacturers. Trade and manufacturers names appear herein solely because they are considered essential to the object of this report.

This information is available in alternative accessible formats. To obtain an alternative format, contact the Office of Public Affairs, Kansas Department of Transportation, 700 SW Harrison, 2nd Floor – West Wing, Topeka, Kansas 66603-3745 or phone (785) 296-3585 (Voice) (TDD).

DISCLAIMER

The contents of this report reflect the views of the authors who are responsible for the facts and accuracy of the data presented herein. The contents do not necessarily reflect the views or the policies of the state of Kansas. This report does not constitute a standard, specification or regulation.

Abstract

Fatigue cracks that develop in steel highway bridges under repetitive traffic loads are one of the major mechanisms that degrade structural integrity. If bridges are not appropriately inspected and maintained, fatigue cracks can eventually lead to catastrophic failures, in particular for fracture-critical bridges. Bridge owners, such as state Departments of Transportation (DOTs), typically rely on trained bridge inspectors to visually inspect steel bridges for fatigue cracking so that appropriate repairs can be applied before cracks reach critical sizes. However, visual inspections can be prone to error due to inconsistent skills and result interpretation among inspectors. Advanced approaches for detecting and/or monitoring of fatigue cracks have been investigated in both the structural health monitoring (SHM) and nondestructive testing (NDT) communities. An important challenge with the existing methods is their reliance on extensive human operations to collect critical measurements in the field, making it challenging to implement long-term continuous crack monitoring of steel bridges.

In this report, a wireless elastomeric skin sensor is proposed to monitor fatigue cracks in steel bridges. The wireless elastomeric skin sensor consists of three components: (1) a large-area strain-based skin sensor, termed soft elastomeric capacitor (SEC), serving as the fundamental sensing unit for crack monitoring; (2) a newly-developed data acquisition (DAQ) board for measuring the small capacitance change from the SEC under fatigue cracking; and (3) a wireless sensing platform (Xnode) for transferring SEC's signal from the DAQ board to the base station in the field. Validation of the wireless elastomeric skin sensor is completed through several numerical and experimental investigations of the fundamental sensing unit, SEC, for fatigue crack monitoring. We validate the integrated monitoring system through a field deployment on a steel highway bridge.

Compared with the off-the-shelf DAQ system, the newly-developed sensor board can collect SEC measurements with better noise performance. More importantly, the developed sensor board can be integrated with the wireless sensing platform Xnode to transfer the collected SEC signals to the base station through wireless communication. This capability will significantly improve the flexibility of the monitoring system by reducing the cabling work in the

field. As a result, the integration of wireless capacitive sensing and the SEC technology enables a wireless elastomeric skin sensor for fatigue sensing of steel bridges.

Data collected in the field showed that, through the trigger-based sensing mechanism, the wireless crack monitoring system was able to collect data continuously and autonomously from the SEC sensors and the strain gauge under the traffic loading. By processing the raw measurements using the proposed algorithm, Crack Growth Indices (CGIs) of each monitored location could be continuously collected and statistically monitored for long-term monitoring of fatigue cracks of steel bridges.

Several further development needs were identified to achieve more robust, accurate, and flexible crack monitoring. First, an improved understanding of the SEC sensor behavior under folded configuration is needed to strategically adjust the CGI algorithm when the SECs are attached to corners and joints. Second, the capacitance sensor board is currently based on analogy circuits, meaning the balancing and shunt calibration are performed manually. Converting the analog circuit to a digital one will enable software control and automation of these processes, hence greatly improving the efficiency and flexibility of the wireless sensing. Third, deployment of the sensor network at more diverse structural configurations and more extensive analyses of long-term field data are necessary to ensure adaptability of the proposed CGI algorithm.

Acknowledgments

The authors of this report would like to gratefully acknowledge the agencies that supported the work done under Transportation Pooled Fund Study TPF-5(328): Kansas Department of Transportation (KDOT), Federal Highway Administration (FHWA), Iowa Department of Transportation (Iowa DOT), Minnesota Department of Transportation (MnDOT), North Carolina Department of Transportation (NCDOT), Oklahoma Department of Transportation (ODOT), Pennsylvania Department of Transportation (PennDOT), and Texas Department of Transportation (TxDOT).

The authors are especially grateful to the lead agency, KDOT, for their support of the work performed under this project, and for knowledgeable guidance and input provided by Mr. Mark Hoppe, Mr. John Jones, Mr. Dan Wadley, and Mr. Loren Risch. Support for the fieldwork on the test bridge provided by Mr. John Waller and Mr. Albert Horn is also greatly appreciated.

The authors would also like to thank the technical liaison from the FHWA, Dr. Justin Ocel, for his continuous feedback and support to this project. Meanwhile, we also thank the representatives from state DOTs for providing valuable feedback through emails and our regular quarterly project meetings, including Lianxiang Du (TxDOT), Joseph Fishbein (MnDOT), Karl Johnson (MnDOT), Wes Kellogg (ODOT), Thomas Koch (NCDOT), Guozhou Li (PennDOT), and Michael Todsen (Iowa DOT).

The authors are grateful to the graduate students who have contributed their talents to this project, including Dr. Xiangxiong Kong, Dr. Parisa Asadollahi, and Mr. Jong-Hyun Jeong. The authors also want to thank the following people for their variety of help on the experimental work in this project, including Danqing Yu, Duncan MacLachlan, Hayder Al-Salih, Sam Tankel, and Sdiq Anwar Taher at the University of Kansas; Austin Downey, Sari Kharroub, and Hussam Saleem at Iowa State University; and Prof. Jian Xu at Wuhan Polytechnic University. Finally, we would like to thank technicians Kent Dye, Matt Maksimowicz, and David Woody at the University of Kansas for their invaluable assistances in the laboratory.

Table of Contents

List of Tables

List of Figures

This page intentionally left blank.

Chapter 1: Introduction

1.1 Fatigue Cracks in Steel Bridges

Civil infrastructures are critical for maintaining vital societal functions. Many older bridges in the United States are prone to structural damage due to carrying a significant amount of service loads over long periods of time. According to the recent infrastructure report issued by the American Society of Civil Engineers (ASCE) in early 2017, the overall score for American bridges is a C+ with over 9% of the nation's bridges rated structurally deficient (ASCE, 2017). These bridges require significant investment in maintenance, rehabilitation, or replacement. Otherwise, structural damage (e.g., cracks, corrosion, or excessive deformation) in critical structural members could impair structural integrity and lead to catastrophic failures (Biezma & Schanack, 2007).

Among the various damage mechanisms in steel bridges, fatigue cracks are extremely common (Fisher, 1984). Caused by the repetitive traffic loads, fatigue cracks are one of the major mechanisms that degrade structural integrity. Fatigue cracks in their initial phase are usually small in size and hence are difficult to be detected. Moreover, depending on loading conditions and structural layouts, these cracks may develop rapidly and weaken structural integrity. If bridges are not appropriately inspected and maintained, fatigue cracks can eventually lead to catastrophic failures, in particular for fracture-critical bridges (Haghani, Al-Emrani, & Heshmati, 2012).

In the United States, one predominant type of cracking on steel bridges is distortion-induced fatigue cracking, which is caused by out-of-plane loading in the web gap region under differential movement between adjacent girders (Connor & Fisher, 2006). Due to the lack of consideration in early bridge design specifications, distortion-induced fatigue cracks are a common issue in many steel bridges built prior to the mid-1980s in the United States (Zhao & Roddis, 2004).

1.2 Challenges for Fatigue Cracks Detection and Monitoring

Bridge owners, such as state Departments of Transportation (DOTs) in the United States, typically rely on trained bridge inspectors to visually inspect steel bridges for fatigue cracking

(National Bridge Inspection Standards, 2004) so that appropriate repairs can be applied before cracks reach critical sizes. However, visual inspections can be prone to error due to inconsistent skills and results interpretation among inspectors (Zhao & Haldar, 1996). For instance, a study by the Federal Highway Administration (FHWA) reported that only two of 49 bridge inspectors across the United States correctly identified fatigue cracks in steel bridges in Virginia and Pennsylvania (Holusha & Chang, 2007).

Advanced approaches for detecting and/or monitoring of fatigue cracks have been investigated in both the structural health monitoring (SHM) and nondestructive testing (NDT) communities. As a result, both the accuracy and robustness of crack detection can be improved by using sensing technologies. Examples include acoustic emission (Roberts & Talebzadeh, 2003), piezoelectric sensor (Ihn & Chang, 2004), Lamb wave (Staszewski, Lee, & Traynor, 2007), and vibration analysis (Blunt & Keller, 2006).

In the context of distortion-induced fatigue crack detection in steel bridges, Yu, Ziehl, Matta, and Pollock (2013) reported an acoustic emission approach for identifying fatigue damage at the fillet weld in representative cruciform joints of steel bridges; and Alavi, Hasni, Jiao, Borchani, and Lajnef (2017) demonstrated a self-powered sensing approach based on a piezo-floating-gate (PFG) sensor for detecting distortion-induced fatigue cracks. An important challenge with these methods is their reliance on extensive human operations to collect critical measurements (acoustic emission data, voltage, or digital videos) in the field, making it challenging to implement long-term continuous crack monitoring of steel bridges.

1.3 Strain-Based Crack Sensing Technologies

Direct strain sensing technologies have the potential to be very effective for crack detection since crack opening leads to abrupt strain change in the localized area. For this reason, both traditional metal foil gages (Tikka, Hedman, & Siljander, 2003) and fiber optic sensors (Glisic & Inaudi, 2012) have been evaluated for crack detection. One general agreement is that cracks can be effectively detected using direct strain measurement if they are in direct contact with or close proximity to the sensor. Since the location of fatigue cracks are not known as *a priori*, to effectively detect cracks, a large number of foil gages would be needed. Fiber optic

sensors are able to monitor strain over a long distance, but may still be limited considering cracks can occur randomly over a large two-dimensional surface. In addition, the limited ductility of the sensing materials leads to breakage of the sensors under cracking, which prevents monitoring of further crack activities.

In the context of fatigue crack detection in steel bridges, Ghahremani, Sadhu, Walbridge, and Narasimhan (2013) adopted strain gauge measurements on a large-scale bridge girder to evaluate the depth characteristics of distortion-induced fatigue cracks, and Bennett, Matamoros, Barrett-Gonzalez, and Rolfe (2014) successfully used strain gages to detect the initiation of distortion-induced fatigue cracks in a test of a scaled bridge. However, a general limitation of traditional metal foil strain gauges is their relatively small footprint, making them less cost-effective when attempting to monitor fatigue damage over a large structural surface.

Recently, novel strain sensors which measure strains over a large area have shown their potential in crack detection. These sensors, often referred to as sensing skins, share one common feature of large size but operate under a wide variety of principles. Examples include carbon nanotube based sensors (Loh, Kim, Lynch, Kam, & Kotov, 2007; Dai, Thostenson, & Schumacher, 2015), resistive sensor sheets (Yao & Glisic, 2015), printable conductive polymer (Loh et al., 2007), patch antenna sensors (Mohammad & Huang, 2010; Yi et al., 2013), and soft elastomeric capacitive (SEC) sensors (Laflamme et al., 2014; Laflamme, Kollosche, Connor, & Kofod, 2012).

In particular, the SEC sensor is a highly scalable sensor due to its ease of fabrication and low cost materials. It is also highly stretchable, enabling a wide strain measurement range; the linearity of the SEC signal has been demonstrated for up to 20% strain (Laflamme et al., 2013). Additionally, SECs are mechanically robust, making them suitable for long-term monitoring. Prior studies have demonstrated that SECs are able to monitor static (Laflamme et al., 2012) and dynamic (Saleem, Downey, Laflamme, Kollosche, & Ubertini, 2015) strain in various civil structural components and can monitor strain maps under in-plane stress conditions (Downey, Laflamme, & Ubertini, 2016).

1.4 Capacitance Measurement Methods

Recent studies have demonstrated that the SEC sensor has sufficient durability for structural crack monitoring, promising the performance in mesoscale sensing of static/dynamic strain responses for both concrete and steel structures (Laflamme et al., 2013; Saleem et al., 2015). However, high-sensitivity sensing demand for micron-level strain deformation of typical civil structures and lack of appropriate data acquisition tool for capacitance measurement limit the use of the SEC sensors for civil structural monitoring applications (Laflamme et al., 2014).

There are various techniques available for measuring capacitance, with oscillator-based capacitance sensing being one of the most well-known methods using RC circuit suitable for wide-range capacitive sensor interfaces. However, it requires high-performance, high-frequency, and an extremely low-jitter clock for small range capacitance variation measurement (Mantenuto, De Marcellis, & Ferri, 2014). Another method is the Wheatstone bridge-based sensing approach, measuring electrical capacitance by balancing two legs of a bridge circuit, one of which includes the unknown-value capacitor. Several investigations have been conducted for the bridge-based capacitance measurement approach (Holmberg, 1995; Mantenuto et al., 2014; Yazdi, Kulah, & Najafi, 2004). Nevertheless, neither of these existing approaches have been validated for wireless civil infrastructure monitoring applications that demand extremely low-level capacitance measurements with a high sampling rate.

1.5 Wireless Sensing Technologies

Structural health monitoring using wireless sensors has emerged as a promising solution that can overcome the limitations of traditional wired methods with many attractive features such as wireless communication, on-board computation, battery power, ease of installation, and so on. Recent successful implementations of wireless sensors for structural health monitoring have demonstrated the efficacy of the technology in measuring structural acceleration, strain, and displacement responses over full-scale applications (Jang et al., 2010; Jo, Sim, Nagayama, & Spencer, 2012; Jo, Park, Spencer, & Jung, 2013; Moreu et al., 2015; Moreu et al., 2016).

Wireless smart sensing (WSS) platforms for SHM have been developed during the past years. Smart sensing platforms are generally featured by several characteristics: (1) on-board

central processing unit (CPU); (2) small size; (3) wireless communication and data transmission; and (4) low-cost (Spencer, Ruiz-Sandoval, & Kurata, 2004). Many WSS platforms have been developed and applied for SHM applications such as the Mica series, iMote series, and Xnode.

The Xnode is an advanced wireless sensing platform with several critical features such as reliable wireless communication, high-fidelity analog-to-digital (AD) converter, expandable data storage, high-precision synchronized sensing, user-configurable middleware software library, automated long-term operation of wireless network, and so on. It is equipped with an LPC4357 (ARM Cortex M0/M4) microprocessor at frequency up to 204 MHz, 24-bit low-noise AD converter (TI ADS131E8), 2.4-Ghz low-power wireless radio transceiver (Atmel AT 86RF233), and it supports up to five analog input channels. In addition, it has a high-capacity rechargeable battery with solar panel support as well as a power supply port to feed 3.3 V to external sensor boards (Spencer, Park, Mechitov, Jo, & Agha, 2017).

Based on advanced wireless sensing platforms, many kinds of accompanying sensor boards have been developed to interact with the wireless sensing platforms for achieving diverse sensing capabilities. Because the measurement environment, frequency range, and budget may be different for purpose, various types of external sensor boards for WSS were developed for acceleration, high-sensitivity strain, and environmental measurements (Jo et al., 2012; Jo et al., 2013; Sim, Spencer, Jo, & Carbonell-Márquez, 2011). However, despite these successful implementations, many advantages of capacitive-based strain sensing are still left untapped using wireless sensor technologies.

1.6 Research Objectives

The overall objectives of research work in this report are to provide state DOTs a practical and cost-effective long-term fatigue crack monitoring methodology using a wireless elastomeric skin sensor. This research is intended to demonstrate the value-added of fatigue crack monitoring of steel bridges using wireless skin sensors over the traditional bridge inspection in the following ways:

1. The ability to collect objective information regarding fatigue crack activity under in-service loading of bridges in continuous manner, improving the

assessment, safety, and reliability of fractural-critical bridges, and providing early warning regarding evolving internal defects.

2. The ability to improve prioritization of bridge repairs (condition-based maintenance) and retrofit for fatigue cracks so as to maximize the effectiveness of limited resources
3. The ability to better assess the effectiveness of various fatigue repair and retrofit techniques for steel bridges through long-term crack monitoring.

1.7 Organization of the Report

This report is organized in the following order: Chapter 2 investigates a numerical approach to simulate SEC's response under fatigue cracking. Chapter 3 illustrates and experimentally validates a crack monitoring algorithm for monitoring fatigue crack growth through small-scale C(T) specimens. Chapter 4 further investigates the SEC-based crack detection in a context of large-scale bridge girder to cross frame connection. Chapter 5 illustrates the development of a wireless capacitive sensing board. Chapter 6 validates the entire monitoring system through a field deployment in a steel bridge. Chapter 7 concludes the report. Figure 1.1 summarizes the organization of this report.

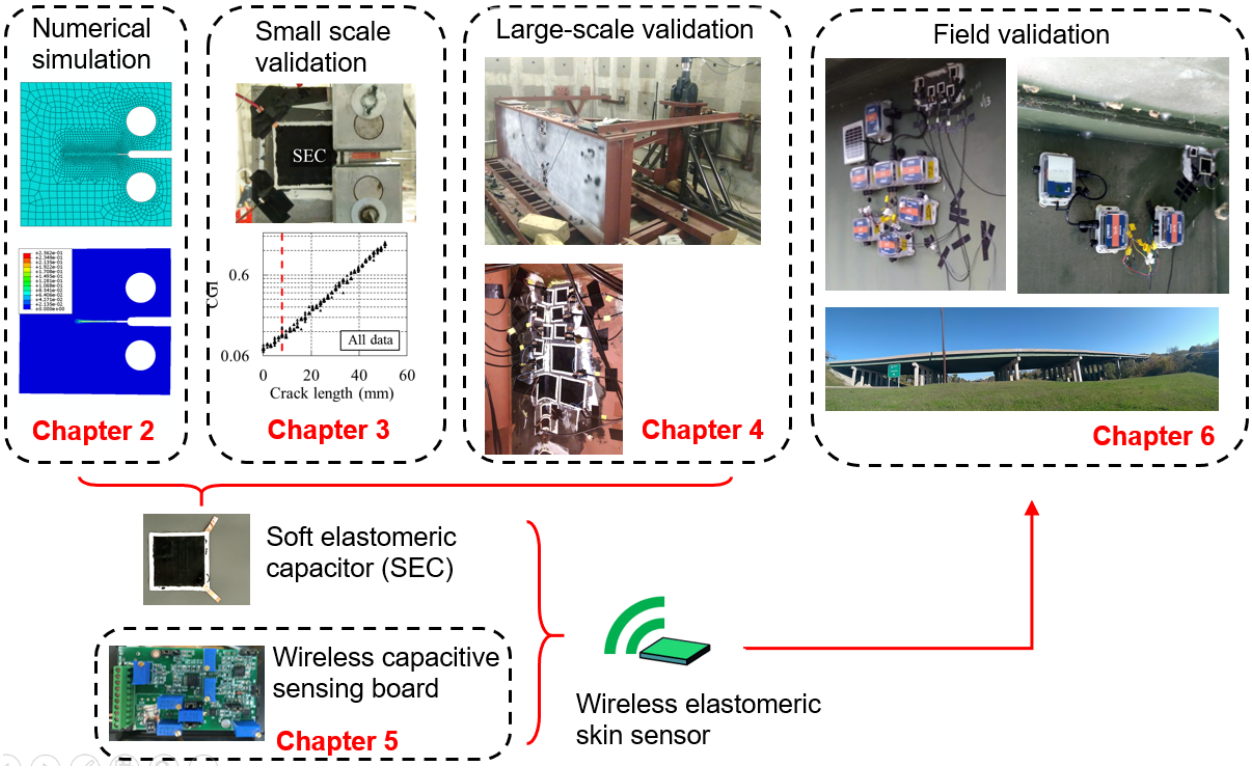

Figure 1.1: Organization from Chapter 2 to Chapter 6 of the Report

Chapter 2: Numerical Simulation of Soft Elastomeric Capacitors under Fatigue Cracking

2.1 Overview

In order to deploy soft elastomeric capacitors (SEC) in steel bridges for monitoring of fatigue cracks, it is critical to develop numerical models capable of linking the sensor's signal to a fatigue crack geometry. This would directly map a sensor network's response to a damage quantification, information which could easily be interpreted by infrastructure operators and managers to conduct condition-based maintenance procedures. Such numerical models could also be used in the design of a dense sensor network of SECs or similar skin-type sensors for the selection and placement of different sensor geometries throughout the network. In this chapter, a numerical method based on finite element (FE) analysis is developed to simulate the SEC's capacitance response under fatigue cracks. An element removal technique in conjunction with a damage evolution model is adopted to simulate fatigue crack propagation in structural components. The SEC sensor is not explicitly included in the FE model. Instead, the FE model of the structural component is meshed in a way such that the deformation of the SEC sensor can be obtained directly from the FE model. A numerical algorithm is proposed to convert the deformation into capacitance response of the SEC sensor. The proposed numerical method is then validated based on experimental data from a C(T) specimen. Finally, a parametric study is performed to investigate the effect of changing the size of SEC sensor on its ability to detect fatigue cracks. The main contribution of this chapter is the efficient and reliable numerical method for investigating the SEC sensor's performance under fatigue cracks generated under different structural configurations, boundary conditions, and loading conditions. The proposed method extends to other measurement devices of similar sensing principle.

2.2 Soft Elastomeric Capacitor

This section provides a brief background on the SEC technology. Its sensing principle is first described, followed by the presentation of typical results on its fatigue crack sensing capability. These results will later be used in the development of the numerical model.

2.2.1 Sensing Principle

The SEC sensor is a flexible capacitor transducing a material elongation into a measurement change in capacitance. A detailed description of the sensor's fabrication procedure can be found in Laflamme et al. (2013). Briefly, its dielectric is composed of a styrene-ethylene/butylene-styrene (SEBS) block co-polymer filled with titania, and is sandwiched between two conductive plates fabricated from SEBS filled with carbon black (Figure 2.1). The SEC sensor can be fabricated in different sizes. In this chapter, the sensor dimension is 76 mm × 76 mm (3 in. × 3 in.), with an effective sensing area of 63.5 mm × 63.5 mm (2.5 in. × 2.5 in.). Figure 2.1(c) is a picture of the SEC sensor used in this chapter, in which two copper tapes are embedded in the top and bottom electrodes (conductive plates) for connecting to the data acquisition system.

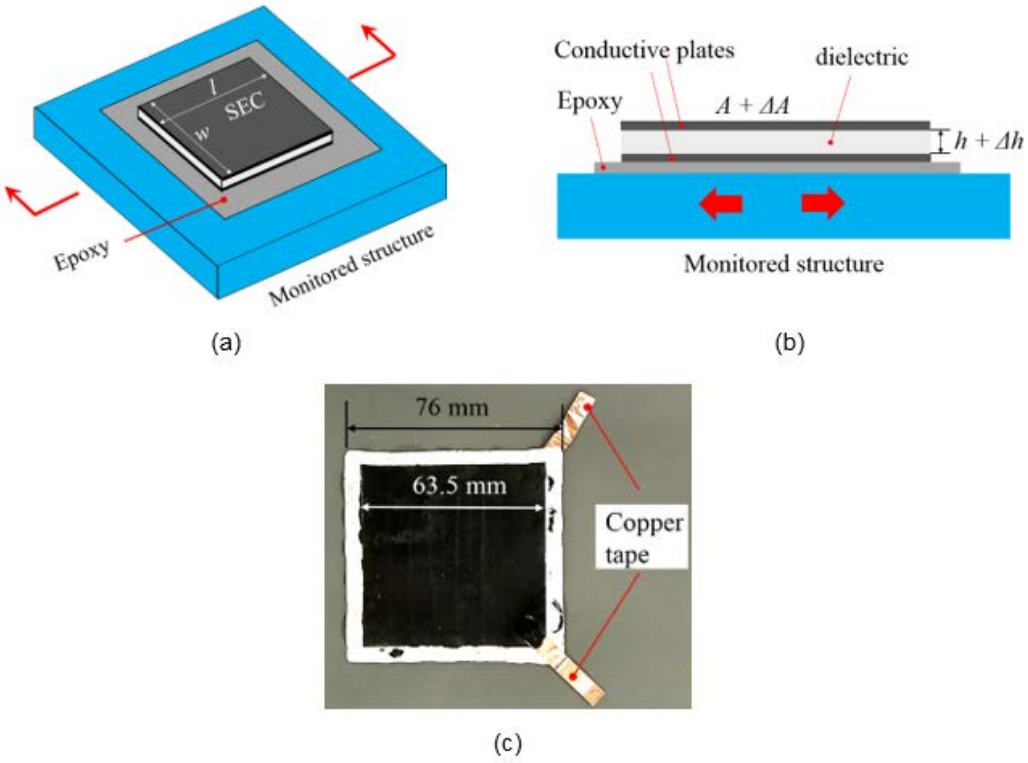

Figure 2.1: (a) Schematic of the SEC Sensor; (b) SEC Sensor Under a Tensile Strain; (c) Picture of the SEC Sensor

The SEC can be attached to a structural surface using bonding agents such as epoxy. As illustrated in Figure 2.1(b), when the structure deforms, the surface strain provokes a change in the SEC's geometry by altering its area A and thickness h. This change in geometry yields a change in the sensor's capacitance C:

$$C = \frac{e_0 e_r A}{h} \qquad \textbf{Equation 2.1}$$

Where:

e_0 is the permittivity of air,

e_r is the permittivity of the dielectric,

$A = w \cdot l$ is the sensing area of width w and length l, and

h is the thickness of the dielectric.

2.2.2 Experimental Validation for Crack Detection

Previously, the SEC sensor has been verified for fatigue crack detection through experimental tests of C(T) specimens (Kharroub et al., 2015; Kong, Li, Laflamme, & Bennett, 2015; Kong, Li, Laflamme, Bennett, & Matamoros, 2015; Kong, Li, Bennett, Collins, & Laflamme, 2016). The C(T) specimens were made from A36 steel with a thickness of 6.35 mm. The dimensions of the specimen are shown in Figure 2.2(a). To generate a fatigue crack, the specimen was connected to a pair of clevises which were mounted to a uniaxial load frame (Figure 2.2(b)). One SEC sensor was attached to one side of the specimen by epoxy, as shown in Figure 2.2(c). A commercial off-the-shelf data acquisition board (ACAM Pcap02) was connected to the top and bottom plates of the sensor to measure capacitance change of the sensor. A 2-Hz cyclic load with a constant load range from 2.89 kN (0.65 kip) to 28.9 kN (6.5 kip) was applied to the specimen. Capacitance measurements were sampled at 25 Hz.

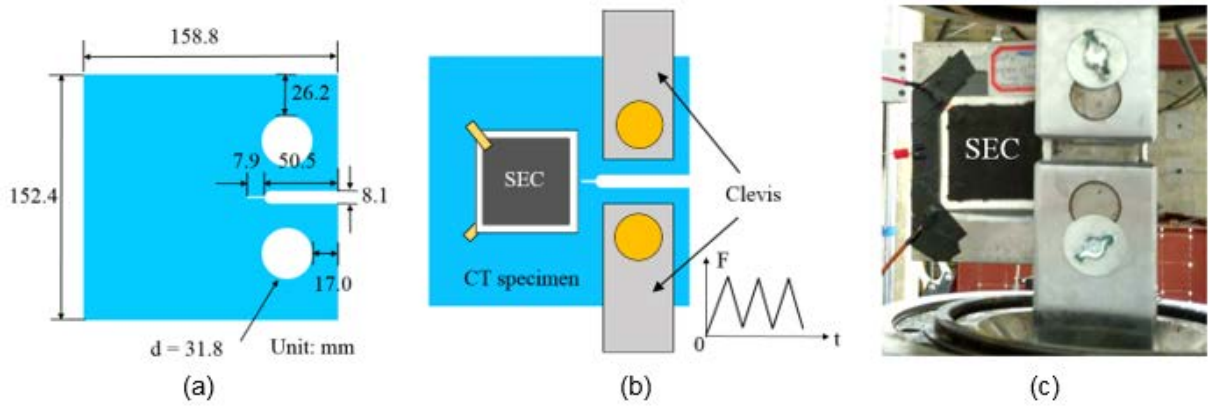

Figure 2.2: (a) Dimensions of the C(T) Specimen; (b) Schematic of Test Setup; (c) Picture of the Test Setup

Figure 2.3(a) shows a crack generated during the test. Figure 2.3(b) shows the sensor's response in terms of the peak-to-peak percentage change of capacitance (*PP C/C₀*), corresponding to different crack lengths with 1.59 mm ($^1/_{16}$ in.) increments. The crack length is taken as the distance measured between the tip of the crack and the edge of the sensing area, as illustrated in Figure 2.4. This distance reflects the length of the crack covered by the sensing area, which is about 7.9 mm ($^5/_{16}$ in.) away from the notch of the specimen. The peak-to-peak amplitude is selected because it provides a more robust measure of capacitance change over long-term monitoring, since the absolute capacitance of the SEC sensor may be subject to drift due to humidity and temperature changes. The result indicates that the SEC sensor is capable of detecting crack growth by showing an increasing change in *PP C/C₀* with increasing crack length.

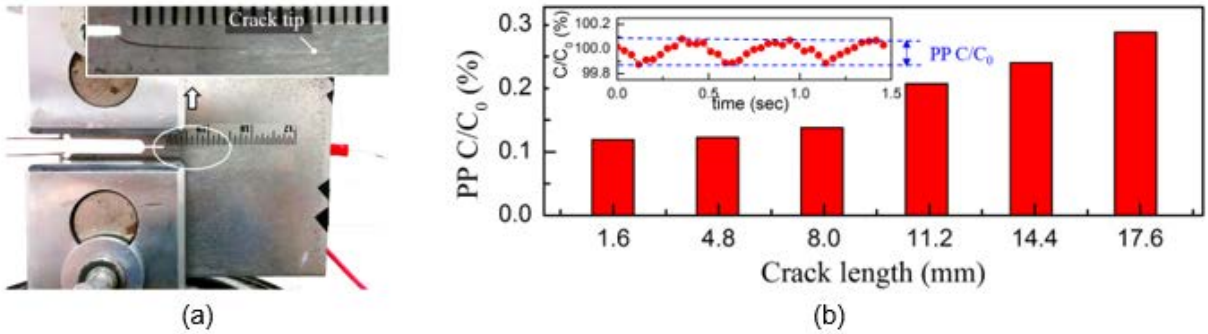

Figure 2.3: (a) Crack Growth in the C(T) Specimen; (b) Percentage Change of Capacitance Versus Crack Length

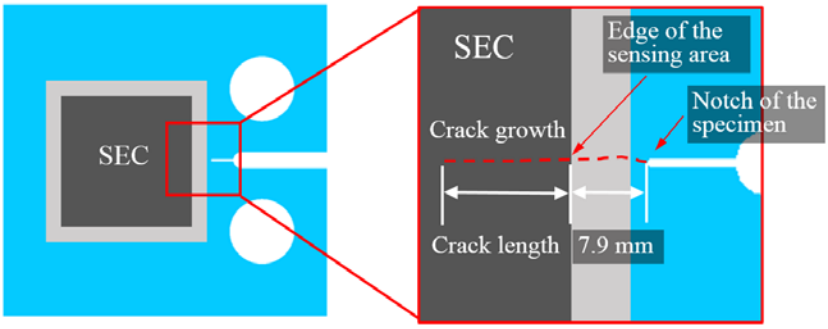

Figure 2.4: Illustration of Crack Length Definition

2.3 Methodology for Numerical Simulation

This section presents the methodology used for the numerical simulations. First, the numerical approach is described. It is followed by a description of the procedure used in simulating crack growth. Lastly, the model of the SEC's electrical response is derived.

2.3.1 Numerical Approach

Figure 2.5 illustrates the overall procedure of the proposed numerical method using a C(T) specimen as an example. A four-step procedure is established: (1) identify crack-prone region of the structural member to determine the location for the SEC sensor; (2) create an FE model of the structural member to simulate the crack growth based on the element deletion method discussed in Section 2.3.2; (3) collect deformation results from the analysis of all elements within the location of the sensor; and (4) compute the capacitance response of the SEC using the algorithm derived in Section 2.3.3. With this procedure, the SEC sensor is assumed to be perfectly bonded to the structure, and its deformation taken as identical to the deformation of the structural member. The proposed numerical method is not limited to small scale C(T) specimens. It can be implemented on more complex structures of different scales, geometric configurations, and boundary conditions.

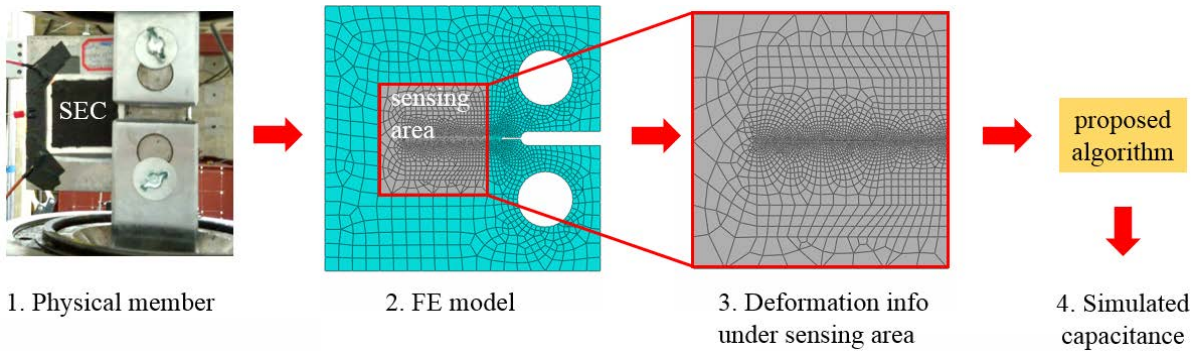

Figure 2.5: Procedure of the Numerical Approach

2.3.2 Crack Growth Simulation

In this chapter, finite element software package Abaqus 6.13 (Dassault Systèmes, 2013) is selected to simulate crack growth. In particular, the element deletion method is adopted to generate cracks in the model, which requires a damage evolution law defined in the material property so that the elements can accumulate damage and be removed from the model once they reach failure point. Several case studies in the literature indicate that the element deletion method can be applied in various applications such as the prediction of crack growth in structural components (Song, Wang, & Belytschko, 2008; Simonsen & Törnqvist, 2004), simulation of metal cutting process (Movahhedy, Gadala, & Altintas, 2000), progressive collapse of building structures (Bao, Kunnath, El-Tawil, & Lew, 2008; Kong, Shi, & Cheng, 2014), and so on.

The principle of the element deletion method is illustrated in Figure 2.6. The material is initially defined as a bilinear model. Then, a damage evolution mechanism is added to the model by defining an initial damage point and a failure point. Under such a damage mechanism, the element starts to accumulate damage once it passes the initial damage point, and it becomes completed damaged after reaching the failure point. Then, the failure elements are completely deleted by the Abaqus program automatically using an element removal technique. By continuously removing the damaged elements, crack propagation can be numerically simulated, as shown in Figure 2.6(b).

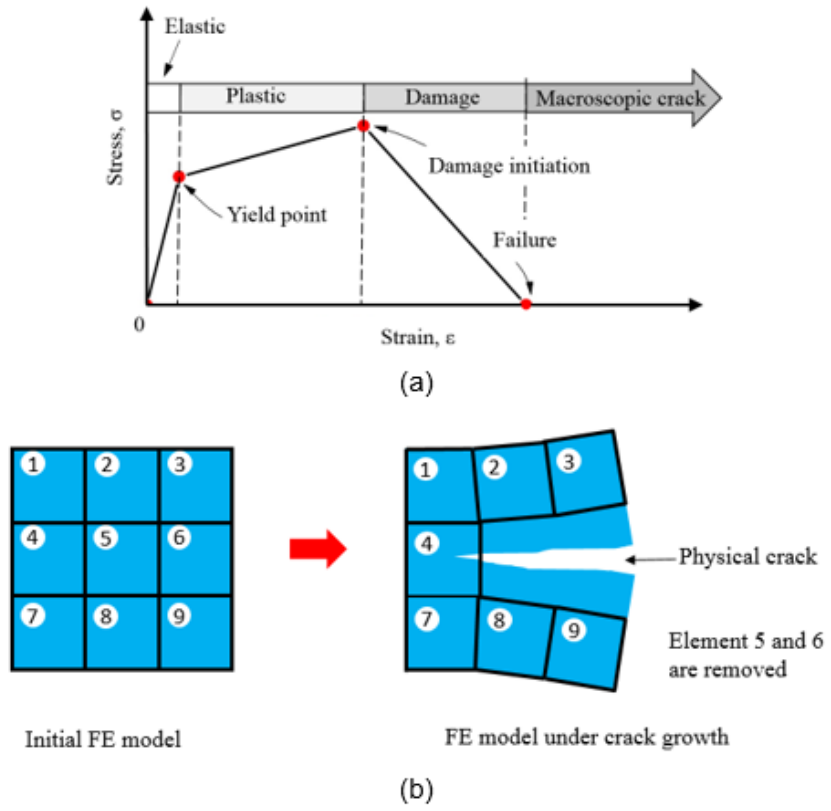

Figure 2.6: Crack Simulation Through the Element Deletion Method
(a) Damage evolution model; (b) Simulation of crack growth by deleting elements where each numbered square is an element

2.3.3 Proposed Algorithm for Capacitance Calculation

An algorithm is required to convert FE analysis results into the sensor's response. Equation 2.1 is the sensing principle of the SEC sensor, by which the capacitance can be computed once the sensing area A and sensor's thickness h are known. However, because the SEC sensor is not physically modeled, this equation cannot be applied directly since h is not available. Equation 2.2 (Laflamme et al., 2013) and Equation 2.3 (Kharroub et al., 2015) describe the relationships between capacitance change and strain change for uniaxial and biaxial strain fields, respectively, where C_0 is the initial capacitance, ε_x and ε_y are the two principle strains, and v is the Poisson's ratio of the sensing material with a typical value of 0.49.

$$\frac{\Delta C}{C_0} = 2\varepsilon$$

Equation 2.2

$$\frac{\Delta C}{C_0} = \frac{1}{1-\nu}\left(\varepsilon_x + \varepsilon_y\right)$$

Equation 2.3

However, both equations are still difficult to be implemented in the FE analysis, because the strain result in FE analysis is commonly reported as the average strain of the element, while the true strain is difficult to obtain. Furthermore, the strain level highly relies on the mesh distribution, which may affect the accuracy of computation results. To overcome these challenges, a modified equation is proposed as follows.

The proposed equation for capacitance calculation directly builds a relationship between sensor's capacitance response and change of the sensing area. From Equation 2.1, the capacitance change of the SEC sensor under deformation can be expressed as:

$$\frac{\Delta C}{C_0} = \frac{C_1 - C_0}{C_0} = \frac{e_0 e_r \left(\frac{A_1}{h_1} - \frac{A_0}{h_0}\right)}{e_0 e_r \frac{A_0}{h_0}} = \frac{A_1 h_0}{A_0 h_1} - 1$$

Equation 2.4

Where:

C_0, A_0, and h_0 are the initial capacitance, sensing area, and thickness of the SEC sensor, respectively.

C_1, A_1, and h_1 are the corresponding values after the sensing skin deforms.

As mentioned previously, the Poisson's ratio of the sensing material is 0.49. The sensing skin can therefore be assumed as incompressible under deformation ($A_0\ h_0 = A_1\ h_1$). The thickness terms can be eliminated using:

$$h_0 = \frac{A_1 h_1}{A_0}$$

Equation 2.5

Substituting Equation 2.5 into Equation 2.4, the capacitance change of the sensing skin becomes:

$$\frac{\Delta C}{C_0} = \frac{A_1^2}{A_0^2} - 1$$

Equation 2.6

Equation 2.6 is under the assumption that the sensor deforms uniformly within the area *A*. In practice, however, the SEC sensor is likely to experience highly nonuniform deformation or

strain under fatigue cracks. To accommodate nonuniform deformation, the sensing area is discretized using finite element meshes. Assuming each element of the sensing area experiences uniform deformation, Equation 2.6 can be applied to each individual element. Within the sensing area *A*, the capacitance change of the i^{th} element can be expressed as:

$$\frac{\Delta C_i}{C_{0i}} = \left(\frac{A_{1i}^{\ 2}}{A_{0i}^{\ 2}} - 1\right)$$

Equation 2.7

The initial capacitance for each individual element C_{0i} is proportional to the area of the element A_{0i}:

$$C_{0i} = \frac{A_{0i}}{A_0} C_0$$

Equation 2.8

Substituting Equation 2.8 into Equation 2.7, the capacitance change of the i^{th} element becomes:

$$\Delta C_i = \frac{A_{0i}}{A_0} C_0 \left(\frac{A_{1i}^{\ 2}}{A_{0i}^{\ 2}} - 1\right)$$

Equation 2.9

The total capacitance change ΔC of the sensing area *A* is the summation of the capacitance change from all *n* elements, which can be expressed as:

$$\Delta C = \sum_{i=1}^{n} \Delta C_i = \frac{C_0}{A_0} \sum_{i=1}^{n} A_{0i} \left(\frac{A_{1i}^{\ 2}}{A_{0i}^{\ 2}} - 1\right)$$

Equation 2.10

Finally, the relative capacitance change becomes:

$$\frac{\Delta C}{C_0} = \frac{1}{A_0} \sum_{i=1}^{n} A_{0i} \left(\frac{A_{1i}^{\ 2}}{A_{0i}^{\ 2}} - 1\right)$$

Equation 2.11

The advantage of Equation 2.11 is two-fold. First, it requires knowledge of only the areas of each element before and after deformation, which can be obtained directly from displacements of the nodes from the FE model. Second, a physical FE model of the SEC sensor is not required because the thickness of the sensor *h* is eliminated in the equation.

Based on Equation 2.11, the proposed procedure for capacitance simulation can be established based on FE results. As illustrated in Figure 2.5, the initial area A_{0i} and deformed

area A_{1i} of each individual element can be collected from the FE model, which are then substituted into Equation 2.11 to compute capacitance change. Additionally, since the SEC sensor remains uncracked even though the underneath substrate has cracked, the area change of all deleted elements during crack propagation (i.e., element 5 and 6 as illustrated in Figure 2.5) are included in the computation. This is done to take into account sensor's measurement over the crack path even though they are physically removed from the model for crack simulation.

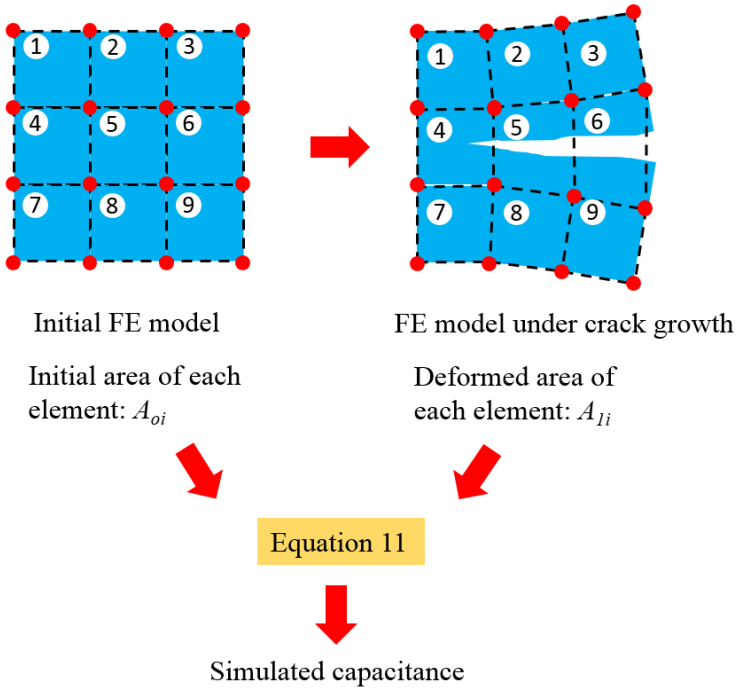

Figure 2.7: Proposed Procedure for Simulating Capacitance Response of the SEC Sensor Based on FE Analysis

2.4 Validation of the Numerical Approach

In this section, the proposed numerical approach is validated through an experimental test with a small-scale C(T) specimen. Since the accuracy of the simulated response of the SEC sensor is highly related to the accuracy of the size of the simulated crack, i.e., crack length and crack width, a two-stage validation is necessary. It includes (1) validation of the crack growth simulation method presented in Section 2.3.2 by verifying the capability of the FE model to predict the crack growth in the tested C(T) specimen; and (2) validation of the capacitance calculation method presented in Section 2.3.3 using the experimentally measured capacitance. In

what follows, the FE analysis is first introduced, followed by the presentation of the two-stage validation.

Table 2.1: Definition of Material Properties in the FE Model

Material property	Value
Young's modulus	2.0×10^5 N/mm^2 (29,000 ksi)
Poisson's ratio	0.26
Yield stress	414 N/mm^2 (60 ksi)
Stress at initial damage point (max tensile stress)	552 N/mm^2 (80 ksi)
Strain at initial damage point	20%
Stress at failure point	0 N/mm^2 (0 ksi)
Strain at failure point	35%

An FE model of the C(T) specimen is created in Abaqus 6.13. The geometric dimensions of the FE model are the same as the test specimen, as shown in Figure 2.2(a). To simulate crack growth, material properties of A36 steel considering damage evolution theory are defined in Table 2.1. Physical meanings of some material properties are illustrated in Figure 2.6(a). The yield stress and maximum tensile stress of the material are determined by uniaxial tensile test of a coupon specimen.

Two types of shell elements are employed for the model, including four-node (S4R) and three-node (S3) elements. Figure 2.8 shows the mesh distribution of the FE model, where a denser mesh is adopted along the crack path. The smallest element is at the tip of the notch (Figure 2.8(a)) with a size of 0.25 mm × 0.25 mm (0.01 in. × 0.01 in.), while elements at the corners have the largest size of 7.9 mm (0.31 in.). The model contains a total of 4,095 elements. To generate a fatigue crack, a cyclic load with a constant load range from 2.89 kN (0.65 kip) to 28.9 kN (6.5 kip) is applied to the FE model through the interior edges of both holes. The Abaqus/Standard module is selected as the solver for this analysis with variable step length.

Figure 2.8(b) shows a crack generated during the simulation, in which a series of elements are identified as failure elements and then removed automatically. Figure 2.8(c) shows the plastic strain at the tip of the crack. These results indicate that the crack growth is successfully simulated using the element deletion method.

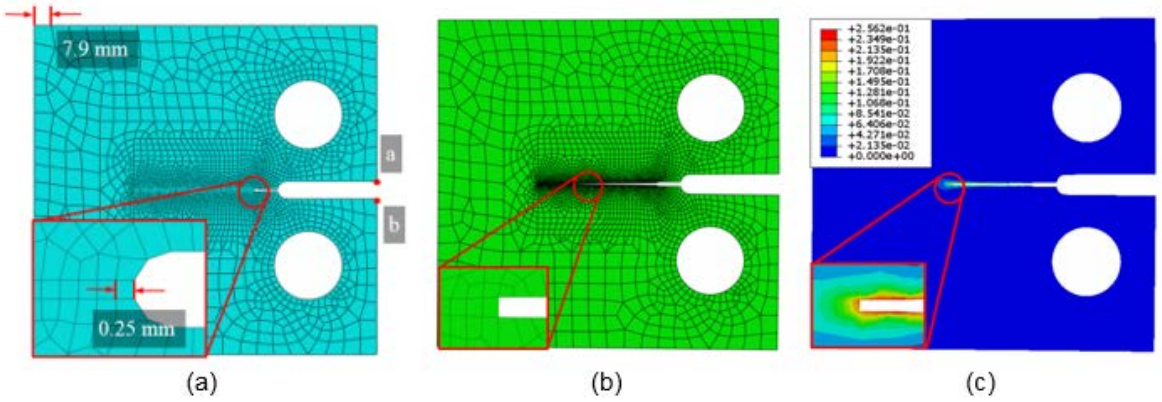

Figure 2.8: (a) Mesh Distribution and Typical Element Sizes; (b) Simulation of Crack Growth; (c) Plastic Strain at the Crack Tip

2.4.1 Stage 1 Validation: Accuracy of Simulated Crack

The purpose of this validation is to verify the capability of the FE model to predict crack size in the tested specimen. This validation procedure is conducted by comparing the compliance at the front face of the C(T) specimen when the crack reaches certain lengths. Figure 2.9(a) shows the experimental setup, where a clip-on displacement gage (Epsilon Model 3541) is mounted at the front face of the C(T) specimen through two knife edges to monitor the crack opening. Meanwhile, displacements at two points *a*, *b* at the same location in the FE model (Figure 2.8(a)) are collected for computing the crack opening in simulation. The compliance (Saxena & Hudak, 1978) at the front face of the C(T) specimen is defined as the ratio between the increment of crack opening ΔU measured by the clip gage and the increment of the applied load ΔF applied on the specimen (Figure 2.9(a)). Figure 2.9(b) shows a comparison of the FE model and the experimental dataset in terms of crack length vs. compliance. The crack lengths are measured by the adhesive measuring tape, starting from the tip of the notch (Figure 2.9(a)). The comparison shows a close match between test and FE model, indicating that the FE model can accurately predict the size of crack during crack growth.

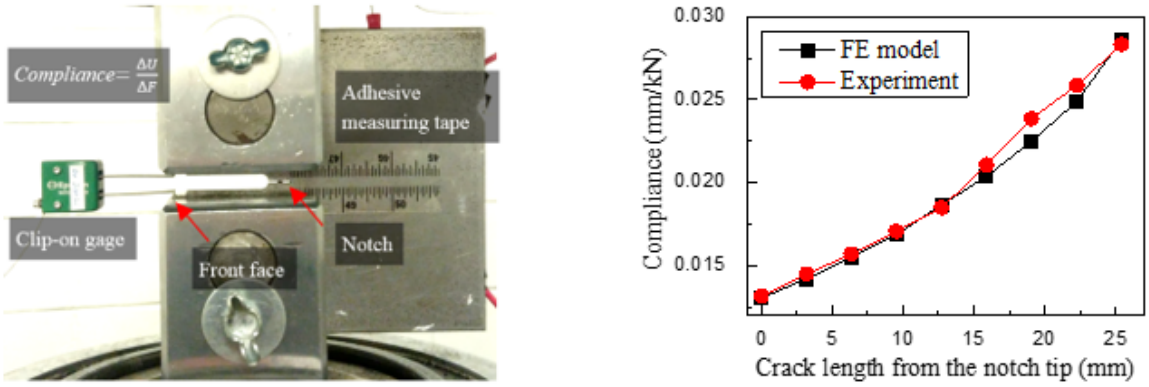

Figure 2.9: (a) Installation of the Clip-On Displacement Gage (the SEC Sensor is Attached to the Back Side of the Specimen); (b) Compliance Comparison Between Numerical and Test Results

2.4.2 Stage 2 Validation: Accuracy of Sensor's Capacitance Response

Once the mechanical behavior of the FE model has been validated, the simulated sensor's capacitance response can be evaluated. The experimental data presented in Section 2.2.2 is used for this validation.

As mentioned in Section 2.2.2, the peak-to-peak percentage change of capacitance (*PP C/C₀*) is selected as a measure for detecting crack growth. The reason is that the absolute capacitance of the SEC sensor is prone to drift due to environmental factors such as temperature and humidity change during long-term monitoring. Figure 2.10 shows the comparison between simulation results and raw experimental data when the crack grows for each 3.2 mm ($^1/_8$ in.) increment in length. The crack length in these plots is taken as the distance measured between the tip of the crack and the edge of the sensing area (Figure 2.4). Comparison in Figure 2.10 shows substantial agreement between test data and simulation in both amplitude and phase. It demonstrates also that the crack growth can be monitored by the steady increment of *PP C/C₀*. For instance, a 0.1% capacitance change can be observed at 1.6 mm ($^1/_{16}$ in.) crack length, while the capacitance change increases by 3 times when the crack length reaches 17.5 mm ($^{11}/_{16}$ in.).

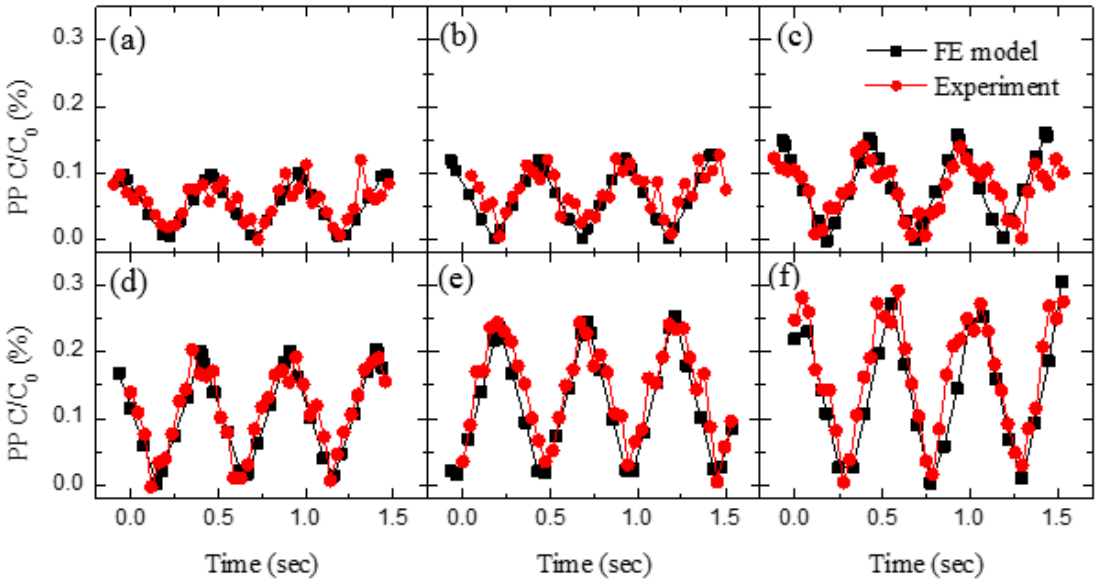

Figure 2.10: Comparison of the Peak-to-Peak Percentage Change of Capacitance Between Simulation Results and Experimental Data When the Crack Length Reaches Different Lengths

(a) 1.6 mm; (b) 4.8 mm; (c) 7.9 mm; (d) 11.1 mm; (e) 14.3 mm; (f) 17.5 mm

The comparison is further investigated in Figure 2.11 in terms of the *PP C/C₀* during the crack growth. The result indicates that the proposed numerical approach can predict a steady increment of capacitance change as the crack grows. This is in agreement with the experimental data also showing a similar trend, despite a smaller increment observable over short crack sizes (from 1.6 mm [$^1/_{16}$ in.] to 8.0 mm [$^5/_{16}$ in.]). This feature can be attributed to the noise content in the raw capacitance measurements, which challenges the identification of changes in the electrical signal under low strain.

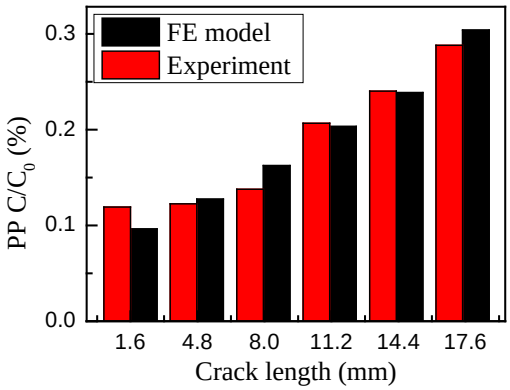

Figure 2.11: Comparison of the Peak-to-Peak Percentage Change of Capacitance Between Simulation and Experiment During the Crack Growth

Through the two-stage validation, the proposed methodology for numerical simulation has been verified for its ability to accurately predict sizes of the crack during propagation and the associated capacitance response of the SEC sensor. Following this validation, the methodology is applied to perform a parametric study to evaluate the effect of changing the size of the SEC sensor on its ability to detect fatigue cracks.

2.5 Crack Monitoring with Different Sensor Sizes

The SEC sensor can be fabricated or cut into different sizes to accommodate various application needs. Sensors with larger size can monitor larger structural surfaces prone to cracking. However, the electrical sensitivity of the sensor, $\frac{\Delta C}{(\varepsilon_x+\varepsilon_y)} = \frac{C}{1-\nu}$, against crack growth decreases with increasing sensor size. In addition, the data acquisition (DAQ) system may be optimized for capacitance measurement when customized to a specific measurement range which is directly related to the sensor size. The motivation of this parametric study is to quantitatively evaluate the effect of the size of SEC sensors on the effectiveness of crack detection, and to provide guidance for dense sensor network optimization for practical applications.

Figure 2.12 shows four FE models of the C(T) specimen with different sizes of SEC sensor, which include 63.5 mm × 63.5 mm (2.50 in. × 2.50 in.) (full size), 47.6 mm × 47.6 mm (1.87 in. × 1.87 in.) (56% size), 31.8 mm × 31.8 mm (1.25 in. × 1.25 in.) (25% size), and 15.9 mm × 15.9 mm (0.63 in. × 0.63 in.) (6% size). Based on the geometric dimensions and material properties of the SEC sensor, the initial capacitance of the full-size SEC sensor is 900

pF from Equation 2.1, which is a typical value of the full size SEC sensor. Since the initial capacitance of the SEC sensor is proportional to the sensing area, initial capacitances of the 56% size, 25% size, and 6% size SEC sensors are computed as 506.3 pF, 225 pF, and 56.3 pF, respectively. The FE models are loaded with the same loading protocol described in Section 2.4. The capacitance responses of the SEC sensor are computed through the proposed algorithm.

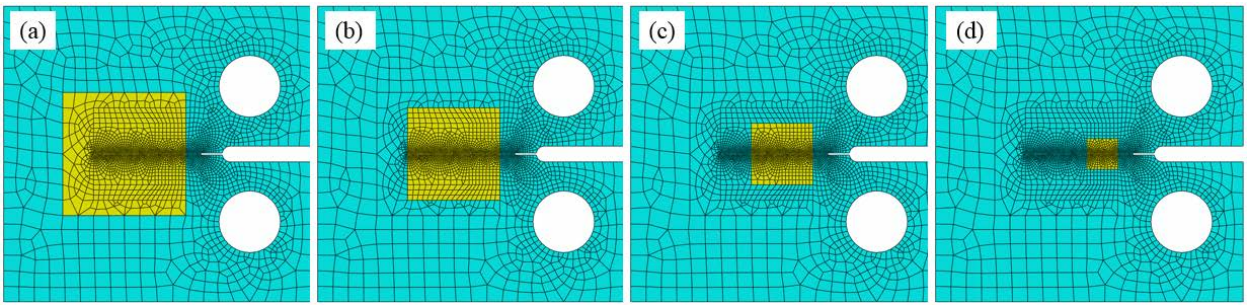

Figure 2.12: FE Models with Different Sizes of Sensing Area
(a) 63.5 mm × 63.5 mm (full size); (b) 47.6 mm × 47.6 mm (56% size); (c) 31.8 mm × 31.8 mm (25% size); (d) 15.9 mm × 15.9 mm (6% size)

Results of this parametric study are shown in Figure 2.13. The crack length is measured as the distance between the tip of the crack and the edge of the sensing area (Figure 2.4). Both peak-to-peak percentage change (*PP C/C₀*) and peak-to-peak change of capacitance (*PP C*) are plotted in the figure against different sizes of the SEC sensor for three different crack lengths: 1.6 mm ($^1/_{16}$ in.), 7.9 mm ($^5/_{16}$ in.), and 14.3 mm ($^9/_{16}$ in.). Results indicate that both *PP C/C₀* and *PP C* increase as the crack grows in length. Take the 6% size SEC sensor as an example, as the crack grows from 1.6 mm to 14.3 mm, *PP C/C₀* increases from approximately 0.5% to 2.0%, and *PP C* increases from approximately 0.25 pF to 1.1 pF. Moreover, when the sensor size decreases, the peak-to-peak change in capacitance (*PP C*) decreases as well. However, the peak-to peak percentage change of capacitance (*PP C/C₀*) increases, indicating that a smaller SEC sensor is more sensitive to cracking. For instance, for the 14.4 mm crack, the sensitivity of the 6% size sensor is approximately eight times higher than the full-size sensor. The tradeoff is that it covers only 6% of structural surface compared with the full-size sensor. In practical applications, the optimal sensor size should be determined to achieve adequate sensitivity while maintaining as large of a coverage area as possible. A network may also be composed of several SECs of

various size, depending on the required crack localization resolution. Figure 2.13 can also be used to predict the expected measurement range for detecting cracks under different lengths. The information can be used to optimize design of the DAQ system for capacitance measurement.

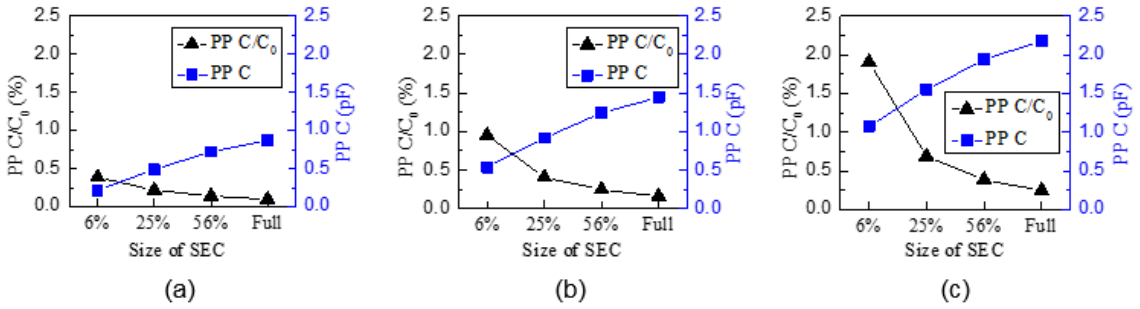

Figure 2.13: Capacitance Change in Terms of PP C/C_0 and PP C for Different Sizes of Sensor when Crack Reaches Different Lengths
(a) 1.6 mm; (b) 7.9 mm; (c) 14.3 mm

2.6 Conclusions

This chapter furthers the understanding of a novel measurement method developed for detecting, localizing, and quantifying damage over mesosurfaces. This technology, the soft elastomeric capacitor (SEC), is a highly scalable strain gauge designed to be deployed in dense sensor network configurations to mimic biological sensing skin. The contribution of this chapter is the development of a numerical approach to predict the SEC sensor's response under fatigue cracks.

The proposed approach consists of two parts: (1) simulating crack growth in the structure with FE analysis using an element deletion method; and (2) converting the FE analysis result into capacitance change of the SEC sensor. The numerical approach is validated by experimental data from a small scale C(T) specimen. The validation demonstrated that the numerical model of the C(T) specimen predicts accurate crack sizes during its propagation, and the proposed algorithm computes accurate capacitance response of the SEC sensor based on the FE result. The validated method is then applied to investigate the effect of changing the size of the SEC sensor on its ability to detect fatigue cracks. For the same crack size, smaller sensors are less sensitive in terms of peak-to-peak capacitance change, but more sensitive in terms of peak-to-peak percentage capacitance change. However, the coverage area may be greatly reduced by using a

smaller sensor. The size of sensor therefore needs to be optimized to cover strategic areas at the desired resolution. The proposed approach enables dense sensor network applications of the SEC by linking the sensor's signal to a fatigue crack location and size. Being able to map a signal to engineering metrics is particularly helpful to infrastructure operators and managers by empowering them with the capacity to conduct condition-based maintenance.

Chapter 3: Small-Scale Experimental Investigation of Soft Elastomeric Capacitors for Fatigue Crack Monitoring

3.1 Overview

The objective of this chapter is to determine whether soft elastomeric capacitors (SECs) are capable of being used as a fatigue monitoring device in common steel bridge applications. To accomplish this, the crack detection ability of the SEC was investigated in the context of high-cycle fatigue cracking, representative of cracking commonly encountered in steel bridges. Compared to low-cycle fatigue cracks, high-cycle fatigue cracks are generally subject to lower stress levels, are dominated by elastic deformation, and thus require a larger number of cycles to initiate and propagate. Importantly, crack openings under high-cycle fatigue are much smaller than those generated by low-cycle fatigue. As a result, monitoring high-cycle fatigue cracking with the SEC can be expected to be a more challenging proposition than monitoring low-cycle fatigue cracking, since the sensor should produce smaller responses under smaller crack openings. Long-term robustness is also critical to deploying an effective crack monitoring strategy in order to ensure functionality over the life of the structure being monitored.

To address these challenges, it was hypothesized that peak-to-peak amplitude (pk-pk amplitude) could be used as an indicator for monitoring crack growth, which would exhibit low sensitivity to capacitance drift. A crack monitoring algorithm based on frequency analysis was developed for accurately identifying the pk-pk amplitude and then calculating the Crack Growth Index (CGI). The approach relies on measurements from the SEC's response as well as the applied fatigue loading. Load can either be directly measured when possible in a laboratory setting or indirectly measured via structural strain in the field. To experimentally evaluate the proposed algorithm, loading protocols were designed to generate high-cycle fatigue cracks in compact, C(T), specimens that are similar to those one would see in full-scale steel bridges subject to traffic loading. The objective is to limit the plastic deformation at the crack tip throughout the fatigue testing. Finally, the hypothesis and the proposed algorithm, were experimentally evaluated using steel C(T) specimens instrumented with SECs for a series of high-cycle fatigue tests to examine whether crack growth could be successfully monitored based on the proposed approach.

3.2 Background

The SEC is a flexible capacitor formed by a dielectric layer sandwiched between two conductive layers acting as electrodes. The dielectric is composed of a styrene-ethylene/butylene-styrene (SEBS) block co-polymer filled with titania, and the conductive layers are fabricated by the same SEBS, filled with carbon black (Figure 3.1(b)). The SEC is attached onto the surface to be monitored, typically using off-the-shelf bi-component epoxy. Strain produces a geometric change in the sensor, producing a corresponding change in capacitance (Figure 3.1(a)). SECs can be fabricated in various sizes. A dimension of 76 mm × 76 mm (3 in. × 3 in.) was adopted in this chapter. The effective sensing area, or the area of the conductive layer, is 63.5 mm × 63.5 mm (2.5 in. × 2.5 in.). Figure 3.1(c) shows a picture of one SEC with two strips of copper tape embedded in the top and bottom conductive plates for connecting to the data acquisition (DAQ) system. A detailed description of the fabrication procedure of the sensor can be found in Laflamme et al. (2013).

As illustrated in Figure 3.1(b), when the monitored structure is under a tensile (or compressive) force, the surface strain provokes a change in the SEC's area A and thickness h, leading to a change ΔC in capacitance C. Starting with the approximation of the SEC as a pure capacitor:

$$C = \frac{e_0 e_r A}{h} \qquad \textbf{Equation 3.1}$$

Where:
e_0 is the permittivity of air,
e_r is the permittivity of the dielectric,
$A = w \cdot l$ is the sensing area of width w and length l, and
h is the thickness of the dielectric.

It can be shown that, under uniaxial strain ε, the change in capacitance is given by Kharroub et al. (2015):

$$\frac{\Delta C}{C} = \frac{1}{1-\nu}\varepsilon \qquad \textbf{Equation 3.2}$$

Where: ν is the SEC's Poisson ratio (ν approx. 0.49, with 1/(1-ν) approx. 2).

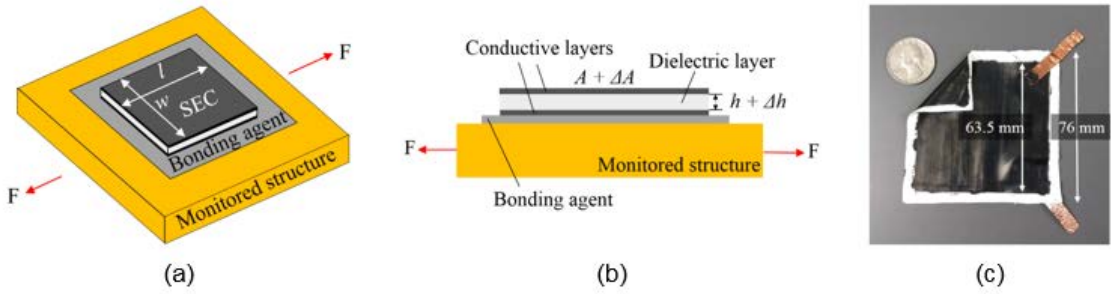

Figure 3.1: (a) Schematic of the SEC; (b) SEC Under a Tensile Strain; (c) Picture of the SEC

The authors approached this investigation with a hyporeport that the strain sensing ability of the SEC could be extended to fit the purpose of fatigue crack monitoring in steel bridges. Figure 3.2 demonstrates a supporting principle using a steel plate as an example. The fatigue load *F* is assumed to have a constant load range, and a fatigue crack initiates at the left edge of the plate and propagates to the right. The SEC is deployed on the plate prior to the crack initiation. Points *a*, *b*, and *c* represent three stages of crack propagation when the crack tip first reaches these locations.

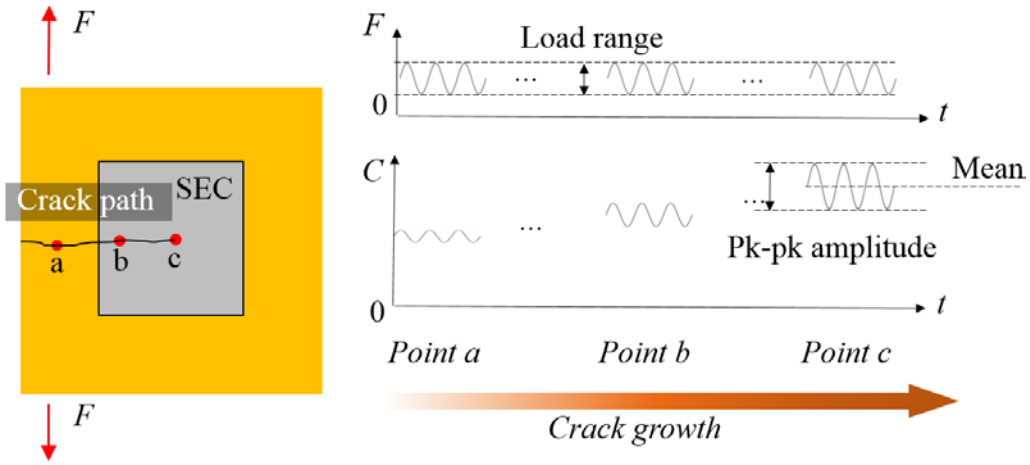

Figure 3.2: Schematic of the Sensing Principle for Crack Monitoring

The crack monitoring capabilities of the SEC can conceptually be thought of as occurring across three stages of crack growth:

1. When the crack is approaching the SEC (point a), the sensor can be treated as a large area strain gage, where localized strain changes can be measured by a change in capacitance C.

2. When the crack grows into the sensing area (point b), the crack opening beneath the sensing skin produces a stretch in the SEC, and thus causes an additional increase in capacitance. Therefore, larger responses in terms of both the mean and the pk-pk amplitude should be observable.
3. When the crack propagates further (point c), higher responses for both mean capacitance and pk-pk amplitude should be measurable. This is due to the fact that the crack weakens the local stiffness of the plate (i.e., the crack opens more under same range of the load).

A challenge associated with SECs is that measurements can be subject to capacitance drift (Ubertini et al., 2014) during long-term monitoring due to environmental factors, such as temperature or humidity changes, and to an intrinsic electrical behavior found in many sensors fabricated from smart materials (Cai et al., 2013; Kang, Schulz, Kim, Shanov, & Shi, 2006).

To ensure robustness against capacitance drift, the pk-pk amplitude of the capacitance measurement (as illustrated in Figure 3.2) was hypothesized to be an indicator of cracking useful for long-term monitoring of fatigue cracking. By extracting only the pk-pk amplitude, the drift effect in the mean capacitance can be filtered out. To illustrate, denote $C_{pk\text{-}pk}$ as the pk-pk amplitude of the sensor's capacitance. $C_{pk\text{-}pk}/C_m$ is then the percentage change of capacitance of the SEC reflecting the amount of strain transmitted to the SEC, where C_m is the mean capacitance. Using the sensing principle (Equation 3.3):

$$\frac{C_{pkpk}}{C_m} = 2\varepsilon \qquad \textbf{Equation 3.3}$$

Now, assume that the excitation load range ΔF is constant over the long-term period, but that the capacitance drifts by ΔC_m, as illustrated in Figure 3.3. Such a drift would provoke a change to the pk-pk amplitude ΔC_{pkpk} as well. Since the monitored strain remains constant before and after the drift, the corresponding relative change in capacitance should remain the same:

$$\frac{C_{pkpk}}{C_m} = \frac{C_{pkpk} + \Delta C_{pkpk}}{C_m + \Delta C_m} = 2\varepsilon \qquad \textbf{Equation 3.4}$$

Rearranging Equation 3.4 provides:

$$\frac{\Delta C_{pkpk}}{C_{pkpk}} = \frac{\Delta C_m}{C_m}$$

Equation 3.5

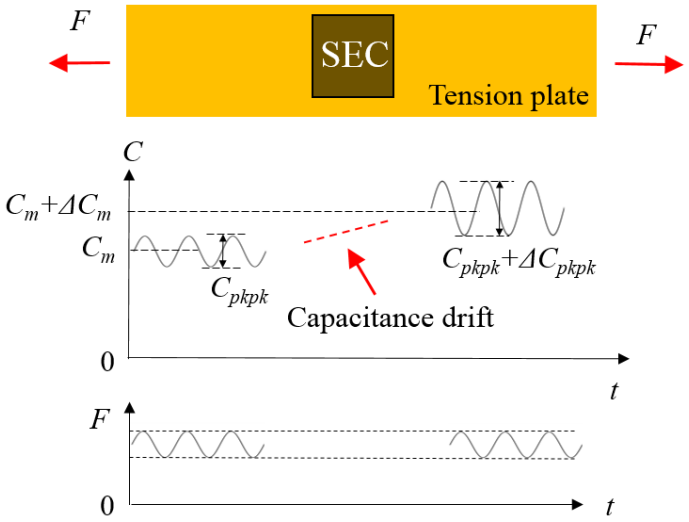

Figure 3.3: Illustration of Drift Impact on Both Mean and pk-pk Amplitude of Capacitance Measurement

Equation 3.5 indicates that the percentage change of the pk-pk amplitude caused by the capacitance drift $\Delta C_{pkpk}/C_{pkpk}$ is the same as the percentage change of the mean capacitance $\Delta C_m/C_m$. In the fatigue tests of this chapter, a maximum capacitance drift was found as 10 pF during a period of several weeks, leading to $\Delta C_{pkpk}/C_{pkpk} = \Delta C_m/C_m$ = 10 pF / 900 pF = 1.1%, in which the 900 pF is a typical mean capacitance C_m of the SECs. On the other hand, test results in this chapter also showed that $\Delta C_{pkpk}/C_{pkpk}$ caused by crack growth reached 100% when the crack grows from 0 mm (0 in.) to 46.0 mm ($^{29}/_{16}$ in.). Such an increment provoked by the crack growth (100%) is much larger than the change of capacitance drift (1.1%) so that the drift can be neglected for tests in this study.

The pk-pk amplitude is sensitive to signal-to-noise ratio due to its small magnitude. For high-cycle fatigue cracks, the pk-pk amplitude can even be smaller, given that fatigue in steel bridges is usually driven by relatively low stress ranges. To robustly and accurately identify

pk-pk amplitude, a crack monitoring algorithm is proposed based on frequency analysis, as explained in the next section.

3.3 Crack Monitoring Algorithm for High-Cycle Fatigue Cracks

An illustration of SEC application for crack monitoring in steel bridges is shown in Figure 3.4. Fatigue cracks can take years to decades to initiate and propagate before reaching a critical size (Zhao & Haldar, 1996). For this reason, continuously collecting data throughout bridge service life is impractical. An effective crack monitoring strategy would follow a multi-timescale (Gupta & Ray, 2007): a fast timescale for data collection and a slow timescale for tracking crack growth. As shown in Figure 3.4, in the fast timescale monitoring, a short-time measurement is taken by the SEC network. Within the period of measurement, the fatigue crack can be assumed unchanged. An indicator of crack length can be extracted for this particular point-in-time using a crack monitoring algorithm. By taking multiple fast timescale measurements and extracting features of crack length over the slow-timescale over the entire fatigue life, the global behavior of crack growth can be identified.

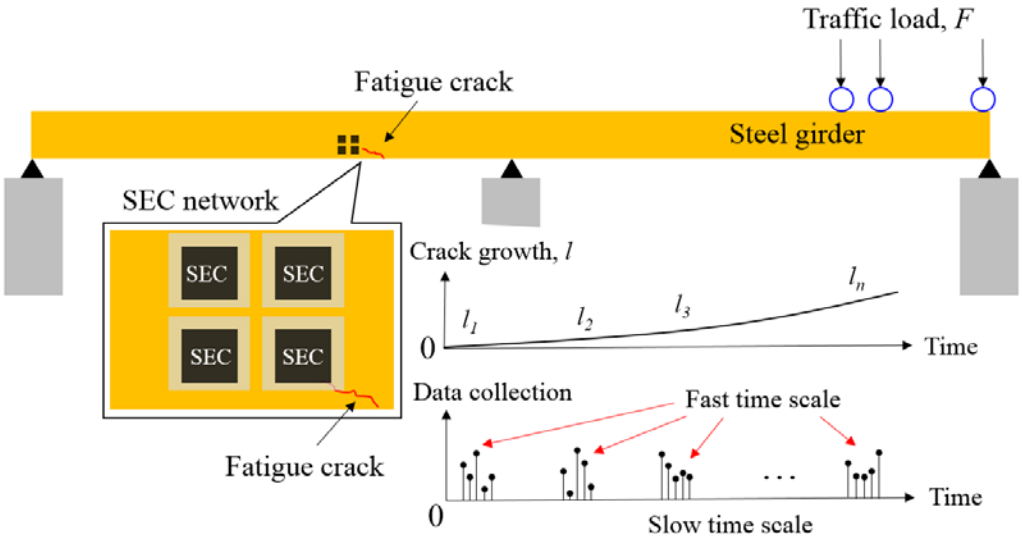

Figure 3.4: Demonstration of Fatigue Crack Monitoring in Steel Bridges Using SEC Network

For this approach to be viable, a computed value is required to serve as an indicator of crack length; the Crack Growth Index (CGI) was developed to serve as such an indicator. The

CGI acts as a normalized strain indicator from which crack growth under the SEC can be inferred. Figure 3.5 depicts the steps used in the developed crack monitoring algorithm for extracting the CGI. The algorithm is a four-step procedure including data acquisition, frequency analysis, establishing CGIs, and crack growth monitoring.

The first step in the monitoring algorithm is data acquisition (Figure 3.5(a)). A series of short time measurements are taken as the crack grows to different lengths (l_i). Both capacitance measurements $C_i(t)$ of the SEC and force measurements $F_i(t)$ of the fatigue load are collected. The pk-pk amplitude of the SEC is directly related to the opening of the crack, but is also affected by the magnitude of load. To successfully identify crack growth through the SEC's response, the capacitance measurements $C_i(t)$ should be normalized with respect to the level of fatigue load. The fatigue load can either be directly measured or indirectly determined via strain measurements.

The next step in the monitoring algorithm is to convert the capacitance, $C_i(t)$, and force measurements, $F_i(t)$, from the time domain to Power Spectral Densities (PSDs) in the frequency domain. Physically, a PSD represents the energy distribution of a signal in the frequency domain. The peak amplitude is then identified to represent the pk-pk amplitude of the time series. Compared with identifying the pk-pk amplitude in the time domain, the peak of the PSD in the frequency domain is less sensitive to noise content in the measurements. As shown in Figure 3.5(b), $peak_i^F$ is denoted as the PSD peak of the i^{th} force measurement $F_i(t)$, and $peak_i^C$ as the PSD peak of the i^{th} sensor measurement $C_i(t)$. Both $peak_i^F$ and $peak_i^C$ should locate at the same frequency (i.e., the loading frequency), but may have different amplitudes.

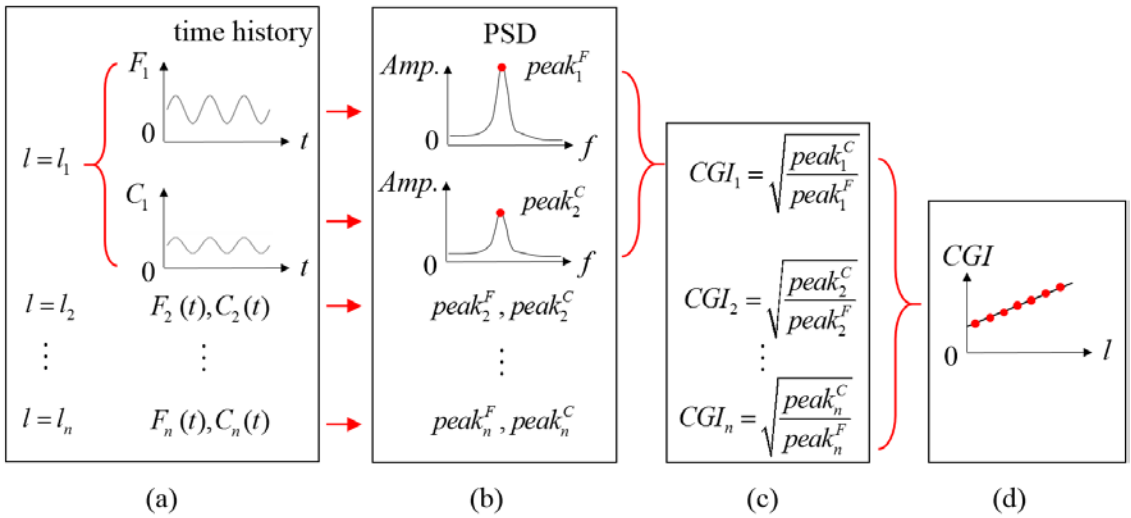

Figure 3.5: The Four-Steps Involved in the Proposed Crack Monitoring Algorithm
(a) Data Acquisition; (b) Frequency Analysis; (c) Establishing CGIs; (d) Crack Growth Monitoring

Once the PSD peaks are obtained, CGI*s* can be computed using equations shown in Figure 3.5(c). CGI is a feature extracted from sensor's measurement $C_i(t)$ and applied load $F_i(t)$. It represents the level of the pk-pk amplitude under a unit excitation load.

In the final step of the algorithm, crack growth is monitored using the CGI values. Specifically, CGI_i at the i^{th} measurement is correlated with its crack length l_i, so that a curve between CGI and crack length can be established (Figure 3.5(d)).

Fatigue testing was performed as part of this study to evaluate to what extent crack growth can be indicated by monitoring increasing CGI, and to evaluate the overall effectiveness of the monitoring algorithm.

3.4 Fatigue Loading Protocols

In previous investigations focused on the SEC performance in the presence of low-cycle fatigue cracks (Kong, Li, Laflamme, & Bennett, 2015; Kong, Li, Laflamme, Bennett, & Matamoros, 2015; Kong et al., 2016), a fatigue load with a 26.0 kN (5.85 kip) constant range was applied to specimens. However, a constant load range only guarantees relatively small crack openings in the early stages of crack propagation. As the crack grows longer, excessive opening and plastic deformation at the crack tip can occur due to significant stiffness reduction. This

leads to crack characteristics which are not representative of fatigue cracks that commonly occur in steel bridges.

To generate realistic high-cycle fatigue cracking, the loading protocol used in this study was based on maintaining a constant range of applied stress intensity, ΔK. A relatively low value for ΔK was used to limit formation of a large plastic zone at the crack tip so that crack openings remained small even as the crack length increased. This approach generated fatigue cracks that are more representative in steel bridges. ΔK is the range of stress intensity within one load cycle and can be expressed as:

$$\Delta K = K_{max} - K_{min} \qquad \textbf{Equation 3.5}$$

Where: K_{max} and K_{min} are the maximum and minimum stress intensity factors.

In fracture mechanics, ΔK is a parameter representing the stress state change around the crack tip caused by the fatigue load ΔF. According to ASTM E1820-15 (2015), for the compact tension specimen adopted in this study (Figure 3.6), ΔK can be determined as:

$$\Delta K = \frac{\Delta F}{B\sqrt{W}} f(\frac{a}{W}) \qquad \textbf{Equation 3.6}$$

Where:

$\Delta F = F_{max} - F_{min}$ is the difference between the maximum load F_{max} and the minimum load F_{min} in one load cycle;

B is the thickness of the specimen;

a is the length of the crack measured from the load line; and

W is the distance between load line and the back face of the specimen.

The term $f(a/W)$ in Equation 3.6 is a polynomial with the variable a/W. Detailed expressions for $f(a/W)$ can be found in ASTM E1820-15 (2015). Dimensions a and W are also labeled in the schematic presented in Figure 3.6.

From Equation 3.6, ΔF can be determined once a desired ΔK is established, but this requires knowledge of F_{max} and F_{min}. A common approach is to introduce the stress ratio, $R = K_{min} / K_{max} = F_{min} / F_{max}$, representing the ratio of maximum stress and minimum stress in one load cycle. In the case of steel bridges, R is the ratio between the magnitude of live load-induced

stress (i.e., vehicle load) and the magnitude of dead load-induced stress (i.e., bridge self-weight), at a particular location on the structure.

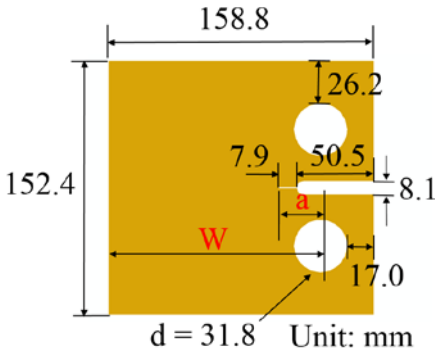

Figure 3.6: Dimensions of the C(T) Specimen

The procedure used to apply the loading protocol is summarized in Figure 3.7. A constant ΔK was first assigned. Then, based on ASTM E1820-15 (2015), the corresponding ΔF for the targeted ΔK was computed. Finally, a chosen magnitude for the stress ratio R guarantees a unique solution of F_{max} and F_{min}, so that the loading protocol can be applied using load control. Three R values were used in the test program (0.1, 0.4, and 0.6) simulating stress ratios caused by passing vehicles with different weights in steel bridges.

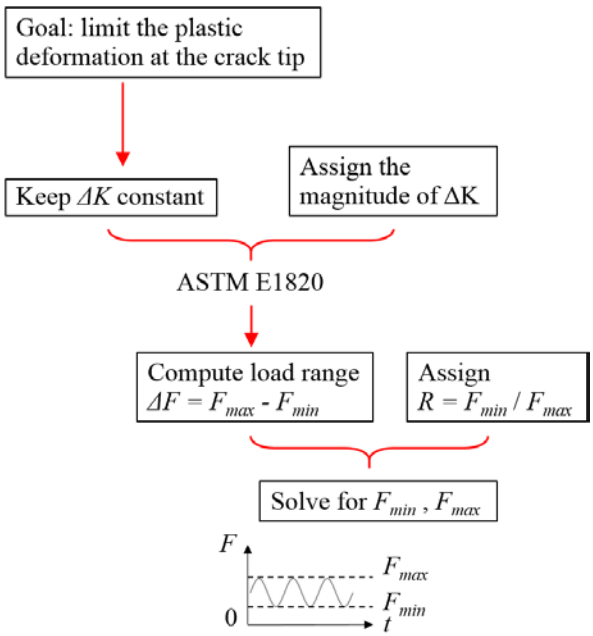

Figure 3.7: Procedure for Determination of the Fatigue Loading Protocol

3.5 Experimental Validations

The SEC's ability to monitor high-cycle fatigue cracks was investigated through fatigue testing performed on steel C(T) specimens. The suitability of the monitoring algorithm was evaluated based on the experimental findings.

3.5.1 Test Configuration

A series of small-scale steel specimens equipped with SECs were tested under fatigue loading using a constant ΔK. C(T) specimens were fabricated from A36 steel plates of 6.4 mm ($^1/_4$ in.) thickness. Figure 3.6 shows the dimensions of the C(T) specimen. The specimens were loaded using a closed-loop servo-hydraulic uniaxial load frame utilizing two clevises. Two adhesive measuring tapes were adhered to the front face of each specimen to allow for visual measurement of crack length during testing. The SEC was attached to the back face of the specimen using bi-component epoxy JB-Weld (Figure 3.8(b)), while the top and bottom conductive layers of the SEC were connected to a DAQ system (ACAM PCAP02) for measuring the capacitance response.

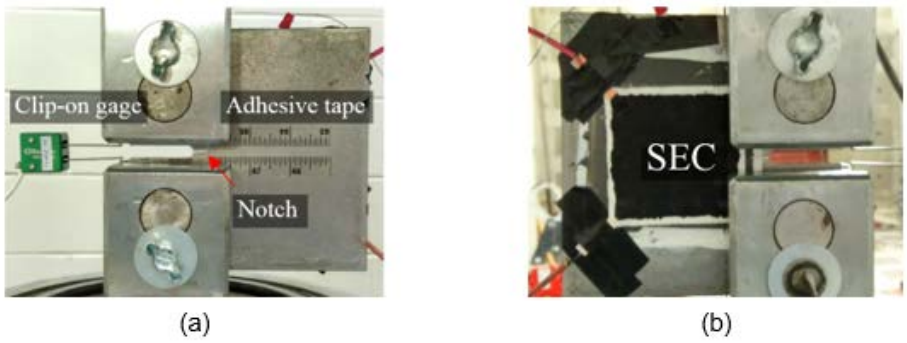

Figure 3.8: (a) Front Face of the Specimen; (b) Back Face of the Specimen

Table 3.1 summarizes the experimental testing procedures used on the three tests included as part of this study, as well as the previous low-cycle fatigue test (Kong et al., 2016). Test 1 was performed using R=0.1. Tests 2 and 3 were performed with identical test parameters, using R=0.6 during crack propagation, but R=0.4 and R=0.6 during each data collection interval. This was done to enhance an understanding of the influence of the stress ratio on SEC performance.

Table 3.1: An Overview of the Procedure on Experimental Testing

Test Number	Range of Stress Intensity Factor ΔK	Crack Propagation Stage	Data Collection Stage
Test 1	22.0 to 27.5 $MPa\sqrt{m}$ (20 to 25 $ksi\sqrt{in.}$)	R = 0.1	Figure 3.9, R = 0.1
Test 2 and Test 3	22 $MPa\sqrt{m}$ (20 $ksi\sqrt{in.}$)	R = 0.6	Figure 3.9, R = 0.4
			Figure 3.9, R = 0.6
Previous Low-Cycle Fatigue Test (Kong et al., 2016)	48.3 to 146.7 $MPa\sqrt{m}$ (44.5 to 133.5 $ksi\sqrt{in.}$)	R = 0.1	Figure 3.9, R = 0.1

A loading frequency of 10 Hz was used for initiating and propagating fatigue cracks. Data collection was performed at every 1.6 mm ($^1/_{16}$ in.) increment of crack growth, and the loading rate was reduced to 0.5 Hz while data was being collected. For each data collection interval, data were sampled at 50 Hz over 100 cycles, and measurements were recorded for actuator force and capacitance of the SEC. After each data collection interval, the fatigue loading rate was returned to 10 Hz so that the crack propagation could be continued.

Figure 3.9 presents the loading protocols applied in the tests with different R ratios: 0.1 (Test 1), 0.4 (Tests 2 and 3), and 0.6 (Tests 2 and 3). The loading protocol used by Kong et al. (2016) for low-cycle fatigue testing is also shown for comparison. It can be seen that the ΔK values used in Tests 1, 2, and 3 were much smaller than used in Kong et al. (2016), representing a higher demanding on the SEC's resolution. Note that crack lengths in these plots were measured from the notch of the specimen (Figure 3.8(a)).

The relationship between stress intensity factor, applied stress, and crack length defined in Equation 3.6 indicates that a longer crack length, a, should correspond to a smaller ΔF if the target ΔK is fixed. This relationship mandates that the difference between the minimum and maximum bounds of the fatigue loading should decrease as the crack grows. As shown in Figure 3.9(a), a multi-stage loading protocol was adopted in Test 1, in which ΔF was re-computed and adjusted for every 9.5 mm ($^3/_8$ in.) of crack propagation, maintaining an approximately constant ΔK within a range between 22.0 $MPa\sqrt{m}$ and 27.5 $MPa\sqrt{m}$ (20 $ksi\sqrt{in.}$ and 25 $ksi\sqrt{in.}$). In Tests

2 and 3, shown in Figure 3.9(b) and 3.9(c), more frequent adjustments were made by decreasing ΔF every 1.6 mm ($^1/_{16}$ in.) of crack growth. This ensured that ΔK was maintained at 22.0 $MPa\sqrt{m}$ ($20\ ksi\sqrt{in.}$) throughout Tests 2 and 3.

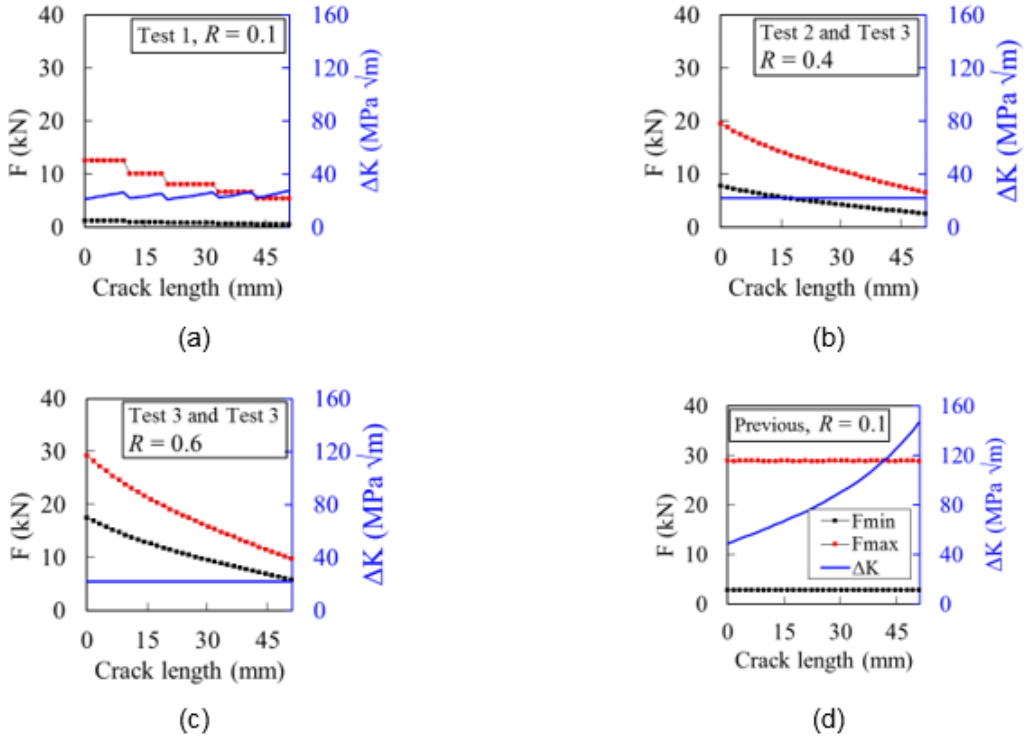

Figure 3.9: (a) Test 1 Loading Protocol, R = 0.1; (b) Test 2 and 3 Loading Protocol, R = 0.4; (c) Test 2 and 3 Loading Protocol, R = 0.6; (d) Loading Protocol Used in Prior Low-Cycle Fatigue Test (Kong et al., 2016), R = 0.1.

Note: Red Dotted Line Represents Fmax, Black Dotted Line Represents Fmin, and Blue Line Represents ΔK.

3.5.2 Crack Growth Under the New Loading Protocols

Figure 3.10 presents a comparison between cracking generated by maintaining an approximately constant value for ΔK, and that generated in previous testing by maintaining a constant value for ΔF. Although the crack sizes obtained in Test 1 are significantly longer than that observed during the previous low-cycle fatigue testing, crack opening was observed to be much smaller. Due to the large crack opening in the previous test, excessive plastic deformation produced a dimple which could be observed at the crack tip, while such plastic deformation was not observed in the tests performed as part of the current study.

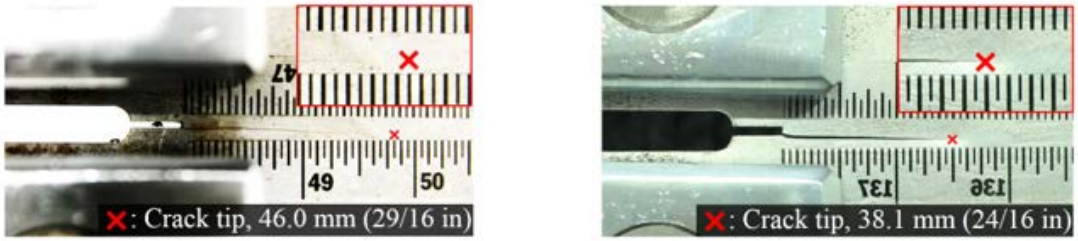

(a) (b)

Figure 3.10: Pictures of Cracks Showing Different Features Between the New and Previous Tests

(a) Crack in Test 1 at 46.0 mm ($^{29}/_{16}$ in.); (b) Crack from Previous Testing (Kong et al., 2016) at 38.1 mm ($^{24}/_{16}$ in.)

Table 3.2 summarizes the fatigue test results, and includes the number of cycles applied, final crack length, and fracture status. Because the load range was continuously decreased in Tests 1, 2, and 3, these specimens did not experience fracture. In the previous test, the specimen failed in ductile tearing when the crack reached a length of 37.1 mm ($^{24}/_{16}$ in.). Tests 1, 2, and 3 produced significantly longer fatigue lives than noted in the specimen previously tested because of the lower ΔK. In particular, nearly 2 million cycles were applied in Test 1, which was performed at the lowest stress ratio (R = 0.1).

Table 3.2: Fatigue Testing Results

Test Number	Number of Cycles	Final Crack Length	Specimen Fracture
Test 1	1,810,000	46.0 mm ($^{29}/_{16}$ in.)	No
Test 2	660,000	50.8 mm ($^{32}/_{16}$ in.)	No
Test 3	605,000	50.8 mm ($^{32}/_{16}$ in.)	No
Previous Low-Cycle Fatigue Test (Kong et al., 2016)	14,500	37.1 mm ($^{24}/_{16}$ in.)	Yes

3.5.3 Evaluation of Proposed Crack Monitoring Algorithm

Figure 3.11 presents sample raw capacitance measurements from the SECs in Tests 1, 2, and 3 as cracking propagated in the C(T) specimens. A full set of SEC's measurement in Tests 1, 2, and 3 can be found in Appendix A. For better pk-pk amplitude comparisons, all the

measurements have been detrended to have a zero mean. Results in these figures show an increasing trend of pk-pk amplitudes as cracking propagated. For example, the pk-pk amplitude increased from approximately 0.5 pF to 2 pF when the crack grew from 0 mm (0 in.) to 46.0 mm ($^{29}/_{16}$ in.). The SEC's measurements showed similar levels of response among the tests for similar crack lengths. One example is that pk-pk amplitudes were approximately 2 pF for all three tests (and all three R values tested) when the crack reached 46.0 mm ($^{29}/_{16}$ in.), as shown in the last column of the figures. This finding indicates that for a certain crack length, sensor response is governed by load range ΔF and is invariant to stress intensity ratio R.

Figure 3.11 also exhibits noise content in the capacitance measurements, especially when crack lengths were short. Identifying the pk-pk amplitudes directly from the raw measurements in the time domain will suffer from uncertainty due to this noise content. For this reason, the proposed crack monitoring algorithm based on frequency analysis was utilized.

Figure 3.12 shows the outcome of the crack monitoring algorithm for all testing cases. The plot for Test 1 is missing data for some crack lengths. This is due to faster than anticipated crack growth. In subsequent tests, more frequent observations were scheduled in order to avoid this loss of data.

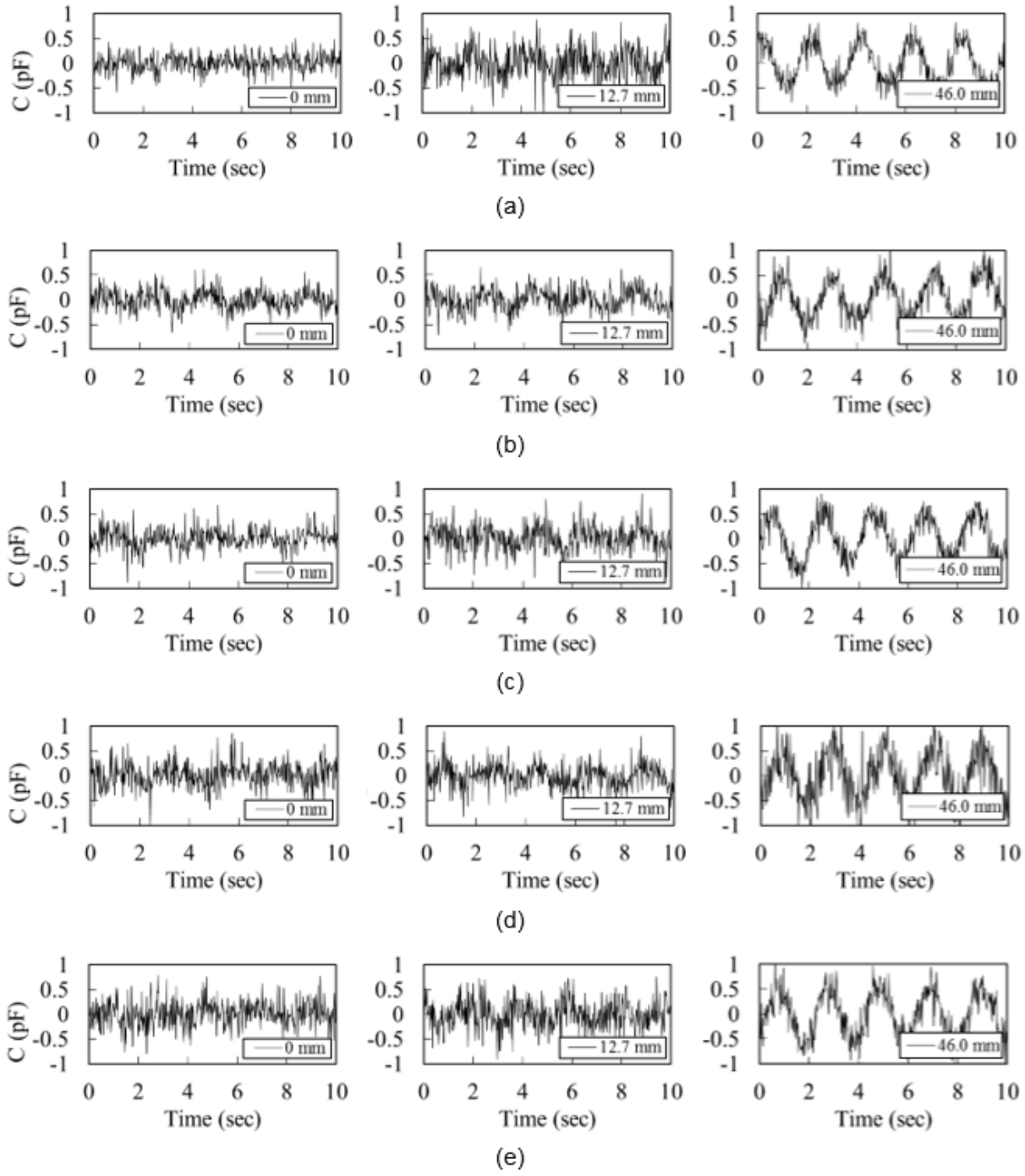

Figure 3.11: Sample Raw Measurements of SECs When the Crack Propagates to Different Lengths

(a) Test 1, R = 0.1; (b) Test 2, R = 0.4; (c) Test 2, R = 0.6; (d) Test 3, R = 0.4; (e) Test 3, R = 0.6. Crack lengths are indicated in each plot.

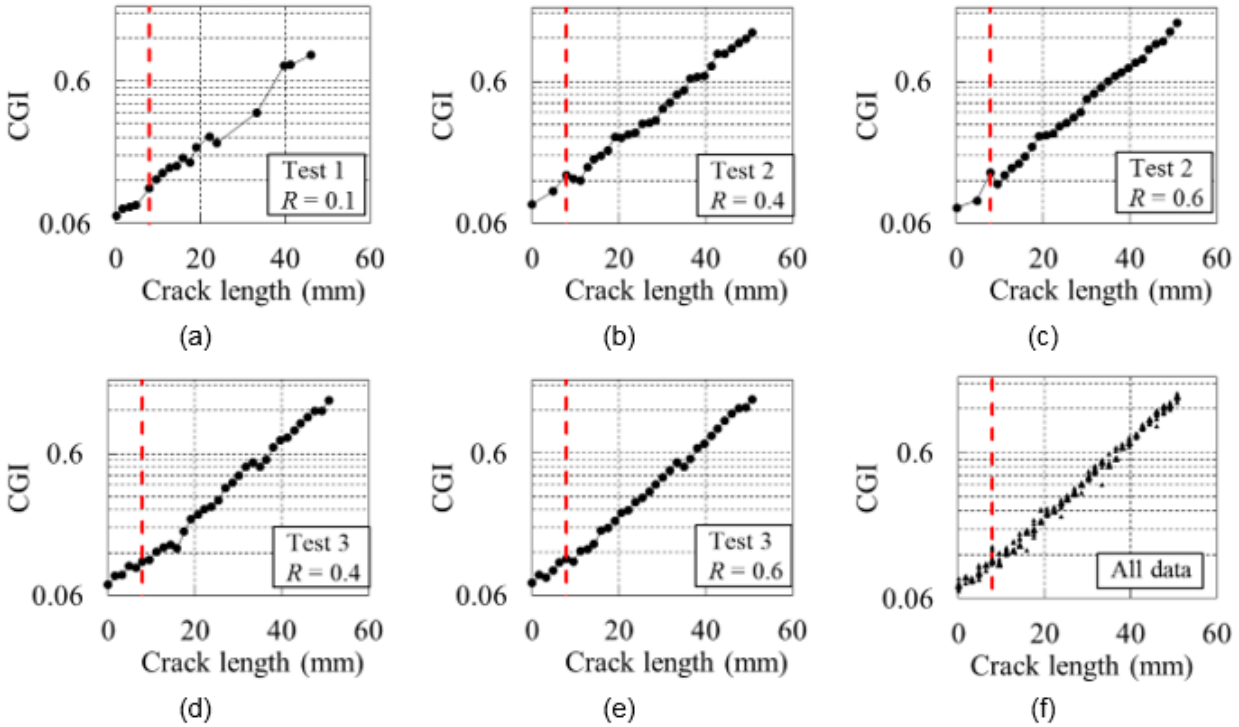

Figure 3.12: Representative Measurements of SECs as the Crack Propagated to Different Lengths

(a) Test 1, R = 0.1; (b) Test 2, R = 0.4; (c) Test 2, R = 0.6; (d) Test 3, R = 0.4; (e) Test 3, R = 0.6; (f) Comparison of All Data.

Red Dashed Line Indicates the Start of Effective Sensing Area on the SEC.

The crack length in Figure 3.12 is measured from the notch of the specimen. However, due to the fact that the effective sensing area of the SEC is less than its outermost dimensions, the crack does not reach the effective sensing area when it initiates from the notch. As shown in Figure 3.13, the notch is at a distance of 7.9 mm ($^{5}/_{16}$ in.) from the edge of the sensing area. The dashed red line in Figure 3.12 indicates the start of the SEC's effective sensing area.

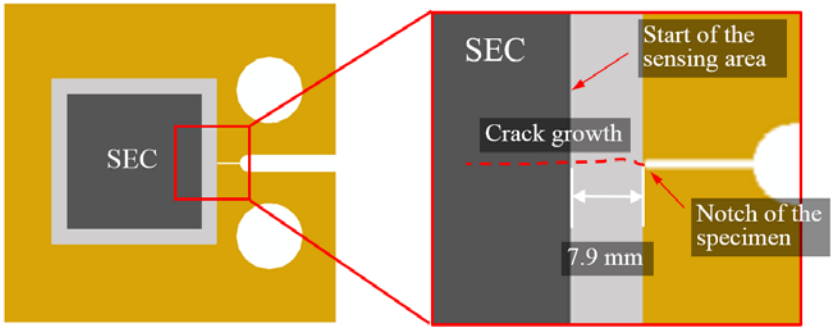

Figure 3.13: Demonstration of the Boundary of the Sensing Area

A positive correlation between CGI and crack length can be clearly observed in Figure 3.12(a) through Figure 3.12(e). An approximate linear relationship was identified between crack length and log(CGI). The data shows that fatigue crack growth can be successfully identified by monitoring the CGI values produced based on the developed algorithm. Furthermore, such a trend also exists when the crack is approaching, but has not quite reached the sensing area, as shown by the data points prior to the red dashed line. This is because the SEC essentially acts as a large-area strain gauge for monitoring the increasing strain field cause by crack growth. As a crack monitoring method based on direct strain measurement, its effectiveness is validated when the crack is either close to or directly underneath the SEC.

Figure 3.12(f) shows a compilation of CGIs for Tests 1, 2, and 3. Excellent agreement was observed between all tests in which fatigue loading with different stress intensity ratios was applied. Considering the fact that a bridge under traffic loading is subject to changing stress intensity ratios over time, the result in this plot indicate the SEC could robustly monitor high-cycle fatigue cracks under different stress ratios, R.

Based on the finding, the proposed crack monitoring algorithm provided a good solution for monitoring fatigue crack growth using an SEC. The algorithm showed robustness even when the crack was small and the measurements were contaminated by noise content. Moreover, the proposed algorithm proved to be applicable for various loading conditions.

3.6 Evaluation of the SEC Under Varying Crack Growth Rate and Random Traffic Load

3.6.1 Motivation

Research work reported in this chapter thus far were based on a constant crack growth rate under harmonic traffic load. Before the SEC-based crack sensing technology can be translated from laboratory to field applications, two research questions need to be addressed. The first research question was whether the SEC can be expected to produce false-positive results during long-term monitoring. Crack propagation in the field is likely to be driven by more complex loadings than the constant crack growth rate. The stress intensity factor range at the crack tip, ΔK, which is the driving force behind crack growth, can be expected to fluctuate due to

changing loading and structural conditions in the field. As a result, the crack propagation rate may fluctuate, and in some cases, the crack may stop growing when ΔK approaches its threshold for crack growth. To ensure that the SEC is capable of consistently monitoring crack growth over the long-term without false-positive results, it is critical to evaluate the SEC-based crack sensing technology under varying crack propagation rates.

The second research question is whether the SEC is still functional as a fatigue crack sensing device under more realistic loading cycles occurring in steel highway bridges. In field applications, traffic loads are composed of a series of load cycles due to passing vehicles. These load cycles can be expected to have different peak-to-peak amplitudes and periods. The load cycles used in Section 3.5 were based on a harmonic time series with a single period and a constant peak-to-peak amplitude, which does not fully capture realistic traffic load cycles in steel highway bridges.

In Section 3.6, we examined these two research questions through fatigue test of a steel C(T) specimen. First, a new loading protocol was created to generate and propagate a fatigue crack under a decreasing ΔK, eventually diminishing all the way to the material threshold for crack growth. As a result, the crack propagation rate continued to decrease until crack growth arrested. Measurements of the SEC under harmonic load cycles were collected, from which crack growth features were extracted. The SEC's crack monitoring performance under the decreasing crack propagation rate was then assessed. The result was also investigated when the crack stopped growing (i.e., when ΔK approached the threshold for crack growth). Second, new stochastic traffic load was established using random peak-to-peak amplitudes and periods, designed to simulate realistic features of traffic loads of steel bridges. An updated crack sensing algorithm was established for extracting crack growth features to investigate the SEC performance under the simulated random traffic load cycles.

3.6.2 Load Range Design

Load range is a critical parameter that governs fatigue crack propagation. Given that one of the research questions being investigated was whether the SEC would produce "false-positive" readings at low load ranges, our objective in selecting a loading protocol was to determine the

upper and lower bounds of a load cycle (i.e., F_{max} and F_{min}), and to adjust those bounds during crack propagation to achieve a decreasing crack propagation rate throughout the test. To accomplish this, the stress intensity factor range, ΔK, was chosen as the design criteria. ΔK represents the change of stress state in one load cycle around the crack tip, and hence governs the crack propagation rate.

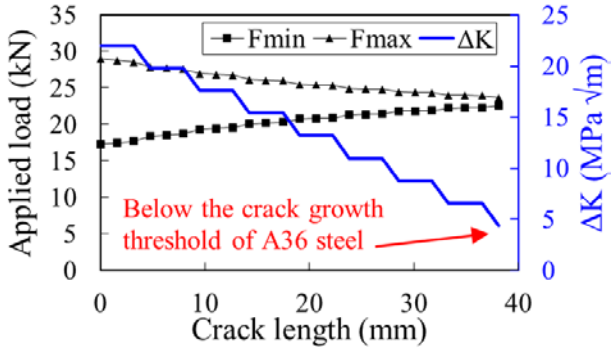

Figure 3.14: Loading Protocol

As shown in Figure 3.14, an initial ΔK = 22.0 MPa√m (20 ksi√in.) was assigned at the beginning of the test. Each time the crack propagated an additional 4.8 mm ($^3/_{16}$ in.), as visually identified by the measuring tape, ΔK was decreased by 2.2 MPa√m (2 ksi√in.). As a result, ΔK was incrementally decreased while the crack propagated, generating a decreasing crack propagation rate. Ultimately, the crack was expected to stop growing when ΔK dropped to 4.4 MPa√m (4 ksi√in.), which is below the crack growth threshold of the A36 steel.

Once the relation of ΔK versus crack length was determined, the corresponding F_{max} and F_{min} of the load cycles was calculated using the recommended method in ASTM E1820 (2015). The stress intensity ratio $R = F_{min} / F_{max}$ was also induced in this calculation, and its initial value was set as 0.6. The resulting F_{max} and F_{min} were equal to 29 kN (6.52 kip) and 17.3 kN (3.88 kip), respectively, at the beginning of the test. The mean load, $F_{mean} = 0.5 \times (F_{max} + F_{min})$, was maintained as 23.1 kN (5.2 kip) throughout the fatigue test.

3.6.3 Traffic Load Cycles Design

When designing the traffic loading protocol for the laboratory test, the goal was to mimic features of realistic traffic loads in steel highway bridges. The stochastic nature of the peak-to-

peak amplitude and period are two important characteristics of traffic load cycles. In steel highway bridges, the peak-to-peak amplitude is governed by vehicle weight. Lu et al. (2002) found that among all type of vehicles, only fully-loaded heavy trucks were critical for fatigue crack propagation, while excitation forces from lighter-weight vehicles were below the threshold of fatigue crack growth. Vrouwenvelder and Waarts (1993) measured 16,000 vehicles in the Netherlands in the 1970s and found the weights of fully-loaded heavy trucks followed normal distributions with coefficients of variation (COVs) from 0.12 to 0.22, depending on specific truck types. To simplify the laboratory loading, only one type of fully-loaded truck was considered in this study, and the peak-to-peak amplitude of load cycles was taken to have a normal distribution with a COV = 0.13.

The period of traffic load cycles, on the other hand, is governed by bridge geometric configuration such as span length and vehicle speed. For a specific steel highway bridge with known geometric configurations, vehicle speed becomes the only factor that affects the loading period. Different statistical distributions have been reported for highway vehicle speed, including bimodal distribution (Dey, Chandra, & Gangopadhaya, 2006), normal distribution (McLean, 1979), and gamma distribution (Haight & Mosher, 1962). In this study, the period of traffic load cycles was assigned a normal distribution. The mean period was taken as 2.49 seconds, while the COV of the period was taken as 0.20.

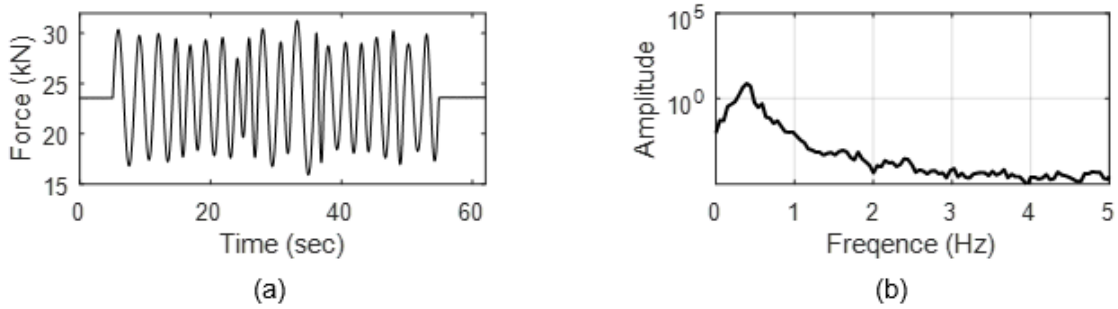

Figure 3.15: (a) Generated Traffic Load Cycles with Stochastic Amplitude and Period; (b) PSD of Traffic Load Cycles

Figure 3.15(a) shows the generated traffic load cycles for the beginning of the test. In total, 20 cycles were generated following the previously-determined statistical distributions of peak-to-peak amplitude and period. The generated waveform was combined with the load range,

F_{max} and F_{min} shown in Figure 3.14, to produce the final traffic load for the whole test. The corresponding power spectral density (PSD) of the generated load cycles is illustrated in Figure 3.15(b). Instead of a single dominant peak at the loading frequency, which was the case for the previous harmonic load cycles, a wide plateau can be observed around 0.5 Hz due to the variation of frequency content in the time series of loading signal.

3.6.4 Crack Sensing Algorithm

The crack sensing algorithm for harmonic load cycles was modified for the case of traffic load cycles. A moving-average filter (i.e., low-pass filter) was applied to smooth the PSD curves as shown in Figure 3.16. The PSD curves of the applied load $F_T(t)$ and capacitance measurement $C_T(t)$ both exhibited a broad-band feature due to multiple frequency contents in the traffic load cycles. To obtain robust results, the moving-average filter is necessary to smooth the PSD curves. With adequate order of the filter, flat plateaus can be achieved and the magnitudes of the flat plateaus ($Peak_C$ and $Peak_F$) are adopted for computing the CGI.

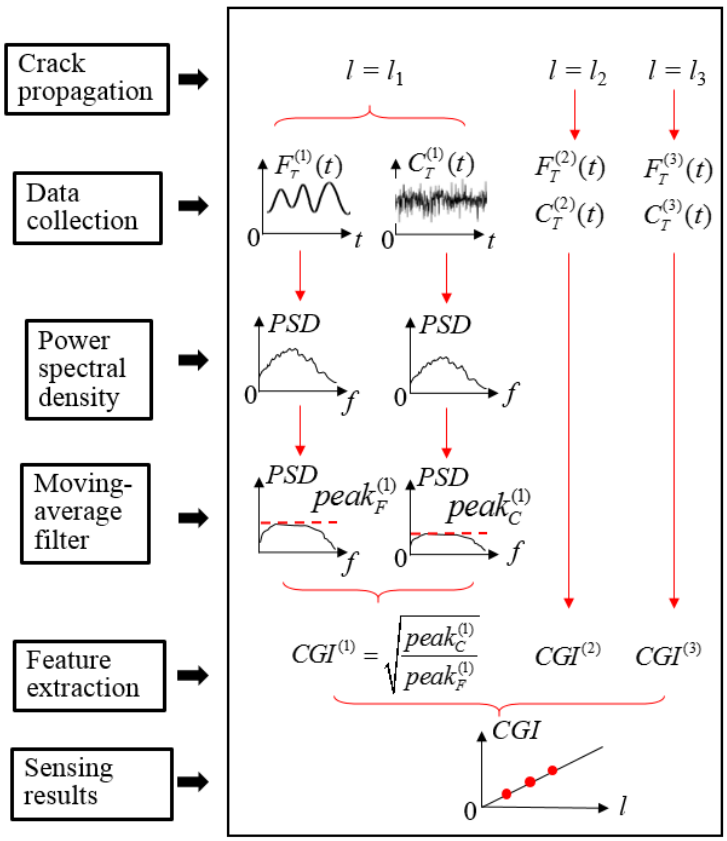

Figure 3.16: Crack Sensing Algorithm

3.6.5 Crack Growth Characteristics

Under the aforementioned test setup with the newly-designed loading protocol, the experimental test was conducted in the Fracture and Fatigue Laboratory at the University of Kansas. During the test, the number of cycles for propagating the crack each additional 1.6 mm ($^1/_{16}$ in.) was recorded. This information was converted to the crack propagation rate in terms of d*a*/d*N* (increment of crack length per load cycle). Table 3.3 summarizes typical crack propagation rates and number of cycles under each ΔK throughout the test.

The crack propagation rate, d*a*/d*N*, was found to be 8.0×10^{-5} mm/cycle ($3.13\text{x}10^{-6}$ in./cycle) at the beginning of the test when ΔK = 22.0 MPa√m (20 ksi√in.), after which it decreased as the crack propagated. Then the crack length reached 38.1 mm ($1^1/_2$ in.) when ΔK = 6.6 MPa√m (6 ksi√in.), d*a*/d*N* became 2.0×10^{-6} mm/cycle ($7.81\text{x}10^{-8}$ in./cycle), which was significantly lower than the initial crack propagation rate. A total of 4.73 million cycles had been applied to the specimen at this point. ΔK was then further reduced to 4.4 MPa√m (4 ksi√in.), and the crack propagation rate was found to be extremely low, after which the crack stopped growing. These observations indicate that the newly designed loading protocol successfully generated a varying crack propagation rate in the fatigue test.

Table 3.3: Crack Growth Characteristics

ΔK	**Number of cycles (million)**	**Crack length**	**da/dN**	**Remark**
22.0 MPa√m (20 ksi√in.)	0.08	3.2 mm ($^1/_8$ in.)	8.0×10^{-5} mm/cycle (3.13×10^{-6} in./cycle)	Decreasing crack propagation rate
15.4 MPa√m (14 ksi√in.)	0.27	15.9mm ($^5/_8$ in.)	3.2×10^{-5} mm/cycle (1.25×10^{-6} in./cycle)	
11.0 MPa√m (10 ksi√in.)	0.79	27.0 mm ($1^1/_{16}$ in.)	1.6×10^{-5} mm/cycle (6.25×10^{-7} in./cycle)	
6.6 MPa√m (6 ksi√in.)	4.73	38.1 mm ($1^1/_2$ in.)	2.0×10^{-6} mm/cycle (7.81×10^{-8} in./cycle)	
4.4 MPa√m (4 ksi√in.)	6.37	38.1 mm ($1^1/_2$ in.)	0	Crack propagation stopped

To evaluate whether the SEC would produce a false-positive result, five additional measurements, taken at increments of 0.2 million load cycles, were recorded under harmonic

load cycles. Figure 3.17 shows a photograph when the crack reached 38.1 mm. Despite the visible crack opening shown in the photograph, the crack propagation rate was extremely slow at this point because ΔK had decreased below the crack growth threshold for A36 steel.

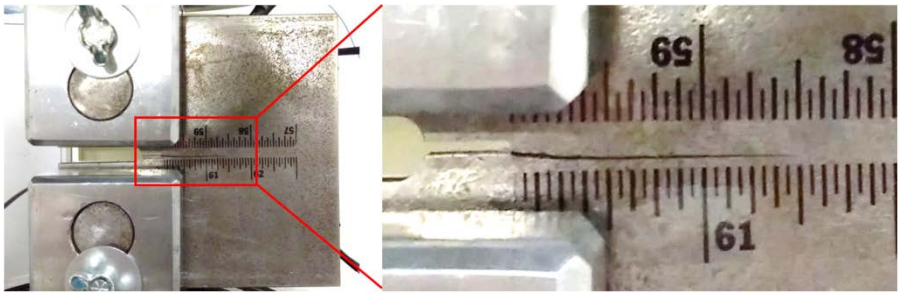

Figure 3.17: Fatigue Crack Developed in the Specimen

3.6.6 CGI Extraction and Crack Sensing Results

By following the proposed crack sensing algorithm shown in Figure 3.16, the CGIs can be extracted from the measurements taken at different crack lengths. Figure 3.18 shows the CGIs under both harmonic and traffic load cycles.

Figure 3.18(a) illustrates CGI versus crack length. The crack length was measured from the notch of the C(T) specimen. In general, the CGIs under both harmonic and traffic load cycles have a similar increasing trend. The lowest CGI occurred at the beginning of the test when the crack length was 0 mm, after which CGI gradually increased as the crack grew longer. This result validates the SEC's ability to detect fatigue crack initiation and monitor crack propagation, regardless of the loading scenarios. In particular, the SEC and its data processing algorithm remained effective under 20 traffic load cycles with random peak-to-peak amplitudes and periods.

Figure 3.18(b) shows CGI versus the number of load cycles, in which the number of cycles is shown in log scale. As described previously, the crack propagation rate continuously decreased during crack propagation. The same behavior was also observed in the CGI, which increased rapidly at the beginning of the test but slowed after approximately 1 million cycles. Importantly, the CGI continued exhibiting an increasing trend toward the end of the test during the period of extremely low crack propagation rate. This result demonstrates the crack monitoring capability of the SEC under a varying crack propagation rate.

Finally, CGIs of the five measurements taken under harmonic load cycles after the crack growth had stopped at 38.1 mm ($1^1/_2$ in.) are marked in Figure 3.18(b), with the details shown in Figure 3.18(c). The CGI remained stable during the additional 1.8 million load cycles applied to the specimen, indicating that the SEC does not produce false-positive results when the crack is not growing.

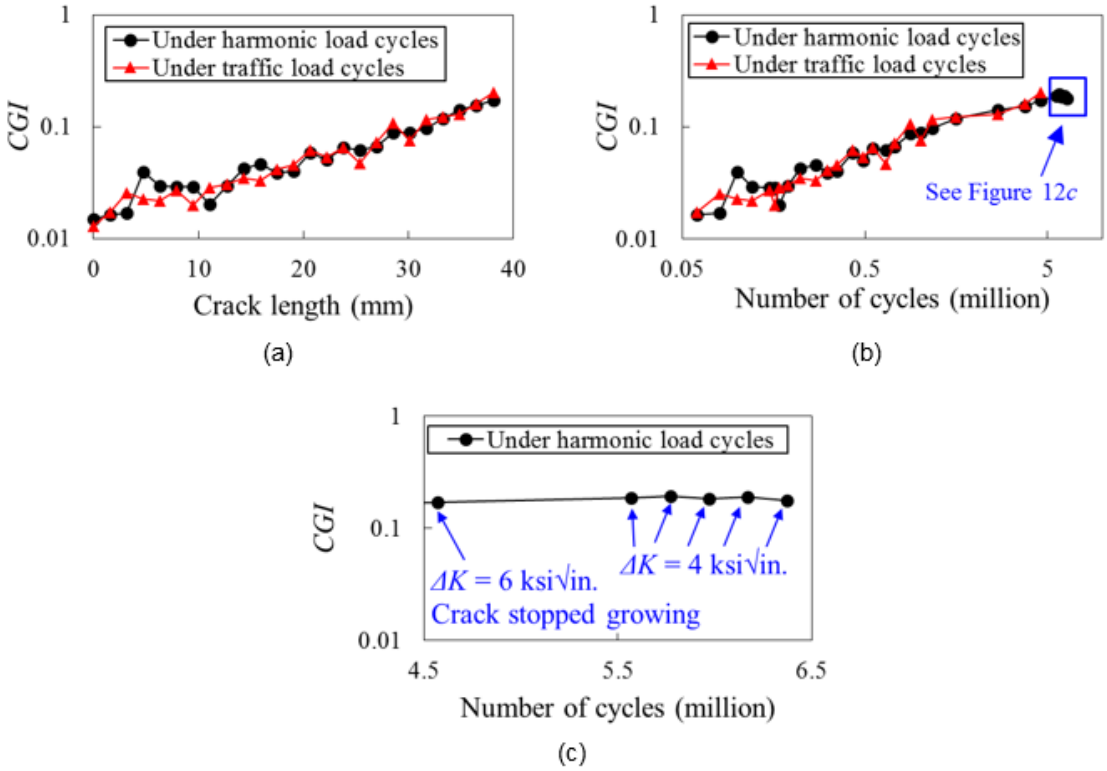

Figure 3.18: (a) CGI vs. Crack Length; (b) CGI vs. Number of Cycles; (c) CGI When the Crack Stops Growing

3.7 Conclusions

This chapter presented a study that was focused on examining the suitability of a novel large-area strain-based sensing technology for monitoring fatigue cracking in steel bridges. The SEC is a large-size, flexible, low-cost, and mechanically-robust capacitive strain gage which has a wide strain measuring range, making it a promising tool for monitoring cracking in bridges. Previous studies have verified the SEC's capabilities for monitoring low-cycle fatigue cracking, but high-cycle fatigue cracking is characterized by small crack openings, which presents a new

challenge for a capacitance-based sensor such as the SEC. To achieve a monitoring solution for fatigue cracking in steel bridges, the pk-pk amplitude of the sensor's measurement was used to construct an indicator of crack growth. Then, a crack monitoring algorithm was established to compute CGIs as a normalized pk-pk amplitude in frequency domain. The sensor's capabilities and the proposed algorithm were evaluated through experimental testing under various stress ratios, *R*. The following conclusions were drawn:

1. The developed algorithm was able to overcome noise infiltration, and resulted in excellent correlation between increasing fatigue crack length and increasing CGI. Therefore, the proposed crack monitoring algorithm was validated by the test data.
2. The proposed crack monitoring algorithm was able to robustly monitor the growth of high-cycle fatigue cracks under various loading conditions, and provided consistent results for the three stress ratios that were studied.
3. With the introduction of the monitoring algorithm, the SEC was found to be capable of serving as a monitoring device for propagating fatigue cracks in steel bridges.

In addition, the emphasis was placed on performance evaluation of the SEC applied over a fatigue crack with varying propagation rates and random traffic load cycles. To facilitate the investigation, we developed an experimental methodology including three components: (1) An efficient data collection strategy was developed by taking multiple short-time measurements during crack propagation, and then extracting crack growth features, the CGIs, to monitor fatigue crack growth in a long-term fashion; (2) A new loading protocol was developed for generating a fatigue crack with decreasing crack propagation rates, and random load cycles that can reflect realistic stochastic features of traffic load of steel highway bridges; and (3) Crack sensing algorithms based on frequency analysis were developed to extract CGIs under harmonic and traffic load cycles.

Experimental results showed an increasing trend of CGI during the process of crack initiation and propagation, despite continuously decreasing crack propagation rate or random traffic load cycles. Furthermore, the SEC produced constant CGIs after the crack stopped

growing, indicating no false-positive results. Results of this study verified the capability of the SEC to detect and monitor fatigue cracks under more complex and realistic loading conditions, which is a critical step towards field applications of the technology.

The research reported in this chapter forms the basis for use of SECs as a robust fatigue monitoring solution in steel bridges. Development of such a monitoring solution is highly impactful, as the sensors themselves are large and can cover large areas in fatigue-susceptible regions of steel bridges, leading to more reliable and comprehensive long-term fatigue monitoring solutions.

Chapter 4: Large-Scale Experimental Investigation of Soft Elastomeric Capacitors for Fatigue Crack Monitoring

4.1 Overview

In this chapter, we investigate the SEC's crack monitoring performance on bridge girder to cross-frame connections subjected to distortion-induced fatigue. Multiple SECs were deployed over a large structural region to form an SEC array. A new fatigue damage sensing approach was then established in terms of Crack Growth Index (CGI) map, which is a 2D image constructed by signals from the SEC array. The CGI map offers more comprehensive fatigue-related information about the monitored structural region than relying on discrete values from individual SECs. The effectiveness of the SEC array and the CGI map were validated through laboratory tests on scaled bridge girder to cross-frame connection models.

4.2 Background

This section introduces the background of this study including: a brief review of the mechanism of distortion-induced fatigue cracking, sensing principle of the SEC, and previous work on extracting fatigue sensitive features from SEC measurements.

4.2.1 Distortion-Induced Fatigue Cracks

Figure 4.1 shows the mechanism of distortion-induced fatigue at web-gap regions in steel girder bridges built prior to the mid-1980s in the United States. Cross frames and diaphragms are used to provide lateral stability to girders, as shown in a skewed bridge configuration in Figure 4.1(a). As illustrated in Figure 4.1(b), the traffic load F applied on top of Girder A leads to a differential vertical movement Δ between the two adjacent girders, which would in turn provoke an out-of-plane bending moment at the top web-gap region in the adjacent girder (i.e., Girder B). This repetitive out-of-plane loading leads to the initiation and propagation of fatigue cracks. A more detailed discussion about the mechanism of distortion-induced fatigue cracks can be found in Jajich and Schultz (2003).

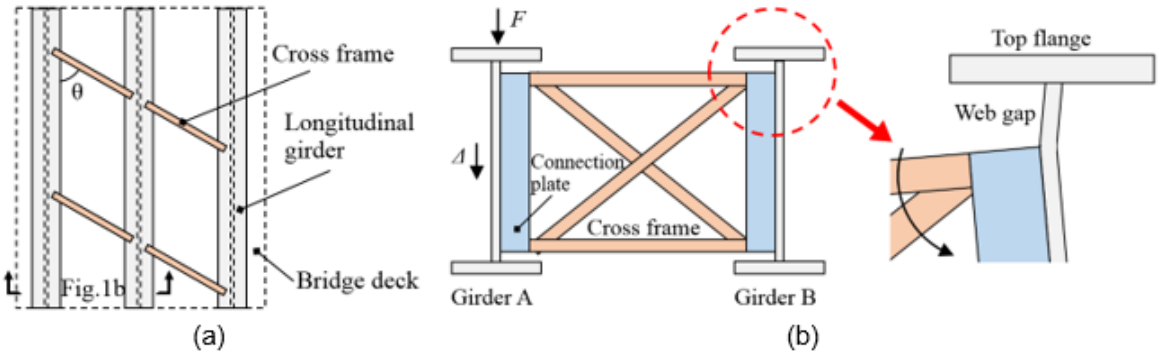

Figure 4.1: Schematic of a Girder Bridge Under Traffic Load
(a) Plan View; (b) Elevation View and Detail of the Web-Gap Region

Figure 4.2(a) is a photo that illustrates a common structural layout of a steel highway girder bridge. Many fatigue cracks have been identified at the web-gap region in this bridge during routine bridge inspections. Figure 4.2(b) shows a typical example where Crack A was found between the top flange and web, while Crack B initiated at the top end of the fillet weld between the connection plate and the web. Depending on the skew angle of the cross frame (denoted as θ in Figure 4.1(a)), Crack B could propagate into the web region, or grow along the fillet weld between the connection plate and the web.

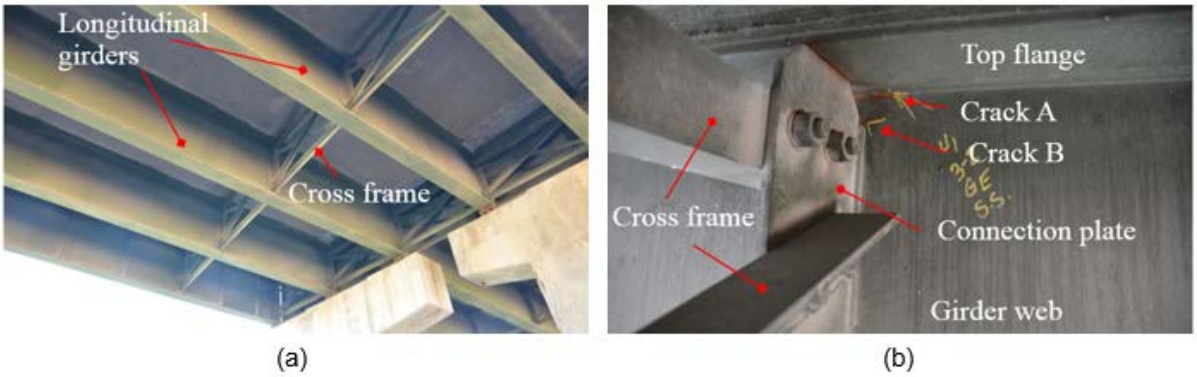

Figure 4.2: (a) A Typical Structural Layout of a Steel Girder Bridge in the Field; (b) Representative Distortion-Induced Fatigue Cracks at the Web-Gap Region

4.2.2 Soft Elastomeric Capacitor

The SEC technology is described in detail in Laflamme et al. (2012). Briefly, as shown in Figure 4.3(a), the SEC is a large-area capacitor consisting of a dielectric layer sandwiched between two conductive layers. The two sizes of SECs adopted in this study (Figure 4.3(b) and

Figure 4.3(c)) are 76.2 mm × 76.2 mm (3 in. × 3 in.) and 38.1 mm × 38.1 mm (1.5 in. × 1.5 in.), with respective nominal capacitance values of approximately 900 pF and 150 pF. Two copper tapes were adhered onto both conductive layers for measuring capacitance of the sensor.

Equation 6.1 shows the sensing principle of the sensor, where C is the capacitance of the SEC, ε_0 and ε_r are the vacuum and polymer relative permittivity, respectively, and l, w, and h are the length, width, and thickness of the SEC (Figure 4.3(a)), respectively. A change in surface strain on the monitored surface will provoke a change in the geometry of the SEC (i.e., l, w, and h), hence changing the capacitance C.

$$C = \frac{\varepsilon_0 \varepsilon_r l w}{h} \qquad \textbf{Equation 6.1}$$

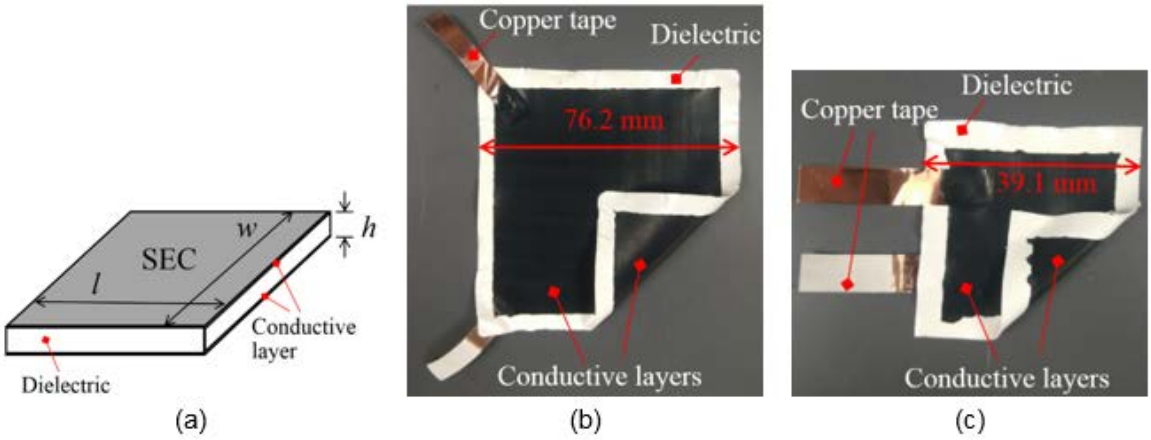

Figure 4.3: (a) Schematic of the SEC; (b) Photo of an SEC of Dimension 76.2 mm × 76.2 mm; (c) Photo of an SEC of Dimension 39.1 mm × 39.1 mm.

4.2.3 Crack Growth Index

Previous work (Kong et al., 2017; Kong et al., 2018; Kong et al., 2019) proposed and demonstrated a crack detection and monitoring algorithm by extracting a crack-sensitive feature, termed the Crack Growth Index (CGI), from the SEC's capacitance measurements. This feature extraction method is briefly reviewed here as it serves as the basis for constructing the CGI map to be introduced in Section 4.3.

Figure 4.4(a) shows the procedure for computing CGI. In the figure, a fatigue crack in a steel plate is generated by the fatigue load F. An SEC is deployed onto the steel plate to monitor

the crack activity. A previous investigation (Kong et al., 2017) verified that the peak-to-peak amplitude of capacitance (denoted in Figure 4.4(a)) of the SEC is a robust indicator for fatigue crack growth. In general, peak-to-peak capacitance increases when the crack propagates due to the reduction of local stiffness around the crack. However, the SEC's signal usually contains noise. Directly identifying the peak-to-peak capacitance from a time-series measurement is challenging. Hence, the power spectral density (PSD) is computed to convert time-series measurement into the frequency domain. The PSD curve represents the energy distribution of the time-series signal, and the peak around the dominant loading frequency (denoted as $peak_C$ in Figure 4.4(a)) can robustly indicate the peak-to-peak capacitance.

The magnitude of the applied load F is also required for CGI extraction. This is because the load range (denoted as Amp_F in Figure 4.4(a)) also directly affects the peak-to-peak capacitance of the SEC. A larger load range would induce higher capacitance response even if the crack does not grow. Hence, the capacitance response needs to be normalized with respect to the load range, which leads to the equation $CGI = \sqrt{peak_C} \,/\, Amp_F$. The applied fatigue load can either be directly measured from the actuator in a laboratory setting or indirectly inferred via strain measurements in practical applications.

Once the CGI is extracted from one set of short measurements, crack growth can be monitored through a long-term monitoring strategy as illustrated in Figure 4.4(b). Briefly, a series of short-time measurements of the applied load F and capacitance response C are collected during the fatigue life of the steel plate. If the crack grows between the data collection intervals, the extracted CGI would increase. By collecting the CGIs through repeated measurements over time, the fatigue crack growth can be monitored. It should be noted that the absolute value of CGI is also governed by the type of normalizer. The normalization procedure for computing CGIs could be based on the applied load from the actuator in the laboratory or the strain measurement from the strain gauge installed in the steel bridge. Therefore, directly comparing CGIs from different test set-ups or normalizers is not meaningful. However, for a predetermined test set-up with a fixed normalizer, the relative change of CGIs (i.e., the increasing trend in Figure 4.4(b)) is a robust indicator of fatigue crack growth.

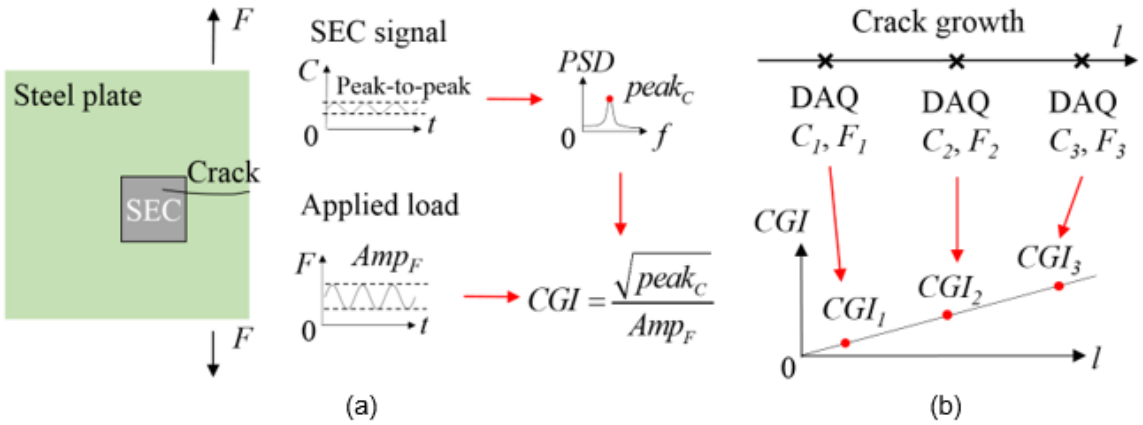

Figure 4.4: (a) Methodology for Extracting CGI from a Single Dataset; (b) Correlating CGI with Crack Lengths Based on Multiple Datasets

Note: DAQ in Figure 4.4(b) represents data acquisition.

4.3 Methodology

Previous research has focused on the examination of a single SEC on a small-scale specimen with an in-plane fatigue crack. The method of CGI extraction reviewed in Section 4.2.3 was developed for single SEC utilization. However, for sensing distortion-induced fatigue cracks in steel bridges, an array of SECs is adopted in this study to cover a larger fatigue-susceptible region. As the number of SECs increases in this application, measurements from the SEC array result in multiple CGIs. Investigating the CGI change for each individual SEC against different crack lengths would be time-consuming and less informative. A better approach is to spatially visualize all CGIs of the SEC array over the fatigue-susceptible region. We do so by extending the CGI index to a CGI map to visually represent the spatial distribution of CGIs.

4.3.1 CGI Map

Figure 4.5 illustrates the methodology for constructing a CGI map. An array of SECs was deployed on a steel plate to monitor the crack growth, and CGI①, CGI②, CGI③, and CGI④ are the CGI values for each individual SEC (Figure 4.5(a)). Where a crack propagates under an SEC (e.g., SEC①, SEC②, and SEC④ in Figure 4.5(a)), the CGI is a direct indicator of crack growth. On the other hand, where the crack does not grow under an SEC (e.g., SEC③ in Figure 4.5(a)), the SEC serves as a large-area strain gauge for monitoring migration of the strain field caused by the crack growth.

Next, the CGIs of the four SECs in Figure 4.5(a) were mapped to a 3D coordinate system where the vertical axis is the magnitude of CGI and the two horizontal axes represent the plane of the structural surface. The CGIs are placed at the centroid of each SEC as shown in Figure 4.5(b). Subsequently, a 3D CGI surface was created using linear interpolation. The 3D CGI surface is a matrix that contains the interpolated CGIs over the zone defined by the four centroids of the SEC array. Finally, by projecting the CGI surface to the structural surface, the 2D image, termed the CGI map, can be constructed as illustrated in Figure 4.5(c).

By constructing a series of CGI maps based on multiple measurements from the SEC array at different crack lengths, fatigue damage in a large region can be monitored. If the fatigue crack does not grow during the data collection intervals, the corresponding CGI maps would exhibit a similar intensity distribution. Conversely, fatigue crack propagation would provoke intensity changes in the CGI maps, which serve as good features for fatigue damage monitoring.

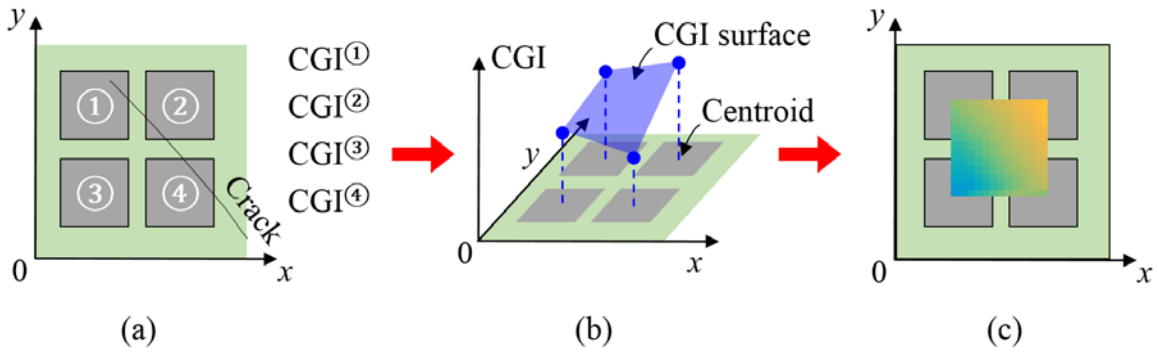

Figure 4.5: Methodology for Constructing CGI Map
(a) Individual CGIs from an SEC Array; (b) a CGI Surface Through Linear Interpolation; (c) CGI Map. Note: The SECs in Figure 4.5(a) and (b) are illustrated as transparent for illustration purpose.

4.3.2 Special Considerations for Distortion-Induced Fatigue Cracks

Section 4.3.1 presented the methodology for constructing CGI maps through a steel plate under an in-plane fatigue crack. However, distortion-induced fatigue cracks in steel bridges usually initiate and propagate along complex paths, as they are subjected to multi-directional states of stress that can vary significantly within the web gap region. As illustrated in Figure 4.2(b), distortion-induced fatigue cracks may initiate between the girder web and top flange (e.g., Crack A), or between the connection plate and girder web (e.g., Crack B). In both cases, cracking

initiates at the weld toe between two adjacent structural components. Furthermore, depending on the structural geometric layout, the crack may continue to grow along the weld. Hence, special considerations are needed for detecting distortion-induced fatigue cracks.

Previous studies (Kong et al., 2017; Kong et al., 2019) validated that the SEC can effectively sense in-plane fatigue damage if the crack directly propagates under the sensing skin. However, to detect a distortion-induced fatigue crack that grows along the weld, the SEC may need to be deployed in a folded configuration. For instance, an SEC should be folded to cover both the connection plate and the girder web to detect Crack B shown in Figure 4.2(b).

4.4. Experimental Configuration

4.4.1 Description of the Test Set-Up

A bridge girder to cross-frame connection was adopted for the experimental tests in this study, as shown in Figure 4.6. To simulate the restraint provided to the top flange of a bridge girder by the deck in the field, the bridge girder was mounted upside-down to the strong floor in the laboratory to constrain the bottom flange of the girder. A cross frame was then installed to the girder through a connection plate. The skew angle θ between the cross frame and the girder was 40 degrees as shown in Figure 4.6(b). To represent the structural layout of typical girder bridges built prior to the 1980s, the connection plate (Figure 4.6(c)) was only fillet welded to the girder web while the top and bottom of the connection plate were not attached to the flanges. A detailed description of the test specimen can be found in Yu, Bennett, and Matamoros (2017).

To apply fatigue load cycles, an actuator was vertically attached to the far end of the cross frame. The actuator was restrained from moving laterally (Figure 4.6(a)) so that it could only move in the vertical direction and apply vertical load to the cross frame. A 0.5-Hz harmonic load was adopted and a load range of -4.9 kN (1.1 kip) to 4.9 kN (1.1 kip) was applied.

As mentioned in Section 4.2.3, the amplitude of the applied load is required for extracting the CGI from the SEC's capacitance measurement. For this purpose, a strain gauge was installed on the top horizontal cross frame member (Figure 4.6(b)) to indirectly infer the amplitude of applied load during the test. A similar strategy could be applied in field applications where the true fatigue load caused by passing vehicles cannot be easily measured.

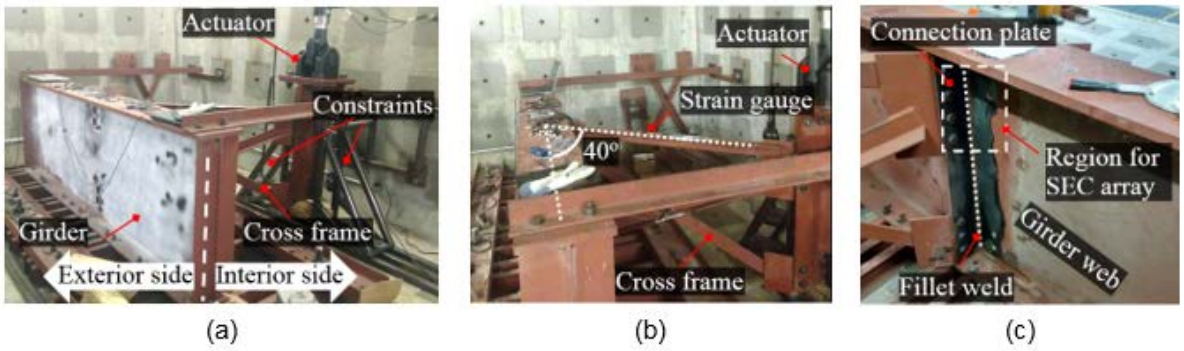

Figure 4.6: (a) Exterior View of the Test Model; (b) Interior View of the Test Model; (c) Detailed View of the Connection Plate

Note: Figure 4.6(c) shows the specimen prior to installation of the SEC array.

4.4.2 Existing Fatigue Damage

Prior to this study, the test model had been fatigue loaded for 2.7 million cycles under a load range of 0 to 11.2 kN (2.5 kip). As a result, a fatigue crack existed at the interior side of the top web-gap region between the connection plate and the girder web. Due to the small opening of the fatigue crack, a fluorescent dye penetrant was used to accurately identify the locations of the crack tip. As shown in Figure 4.7, the length of the fatigue crack was measured as 19.1 mm (0.75 in.).

Figure 4.7(c) shows the detailed layout at the top web gap region of the connection model. The connection plate was not welded to the girder flange, leaving a gap between the flange and connection plate, which was the primary reason for causing distortion-induced fatigue cracks as discussed in Section 4.2.1.

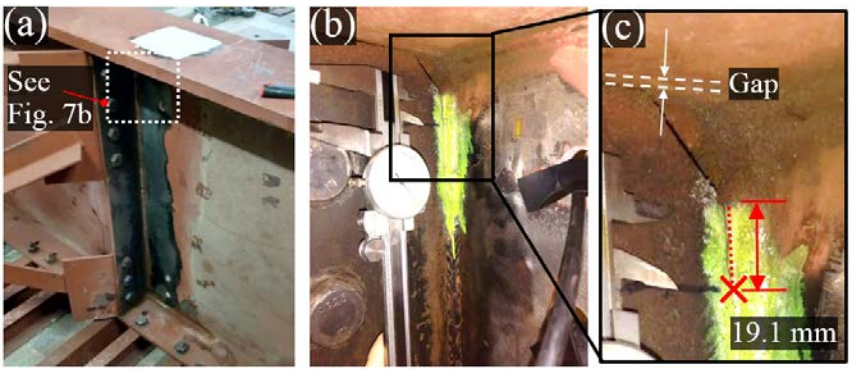

Figure 4.7: Existing Fatigue Damage in the Connection Model

(a) Overview; (b) Fatigue Crack at the Top Region of the Connection; (c) Detailed Look at Figure 4.7(b)

4.4.3 Deployment of an SEC Array

To detect and monitor distortion-induced fatigue damage in the test girder, an SEC array was deployed at the top web-gap region, as shown in Figure 4.8(a). SECs with dimensions of 76.2 mm × 76.2 mm (3 in. × 3 in.) are termed large SECs, while those with dimensions of 38.1 mm × 38.1 mm (1.5 in. × 1.5 in.) are termed small SECs. A total of 11 SECs were deployed on the structural surface using a bi-component epoxy (JB Weld). Figure 4.8(b) schematizes the sensor layout. Folded SECs (i.e., SEC a1, a5, and a10) were deployed along the weld to detect crack growth at the weld toes. Flat SECs, on the other hand, were intended to serve as large-area strain gauges to sense the strain field migration caused by cracking activity. An off-the-shelf data acquisition (DAQ) system (ACAM PCAP02) was used to collect the capacitance measurements of the SEC array.

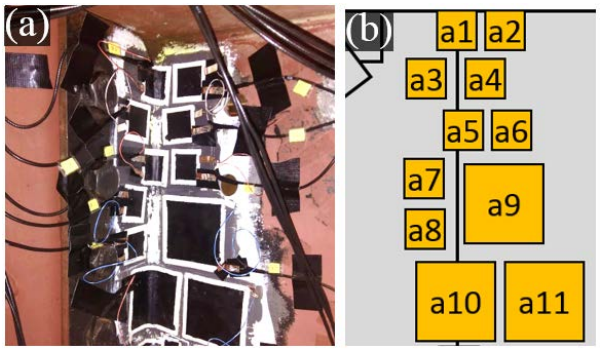

Figure 4.8: (a) SEC Array Arrangement; (b) a Schematic of the Sensor Layout

4.4.4 Experimental Procedure

During the test, 130,000 new load cycles were applied to the test girder under the load range of −4.9 kN (−1.1 kip) to +4.9 kN (+1.1 kip). A total of 13 datasets were collected at cycle counts of 0, 15,000, 21,500, 30,000, 43,100, 53,800, 64,900, 79,200, 93,000, 101,300, 110,000, 121,000, and 130,000. Each dataset contained both capacitance measurements from the SEC array and the strain gauge collected over 2-minute periods, sampled at 50 Hz and 2,000 Hz, respectively. During the test, four inspections were performed to identify crack lengths at cycle counts of 0, 71,000, 101,300, and 130,000 cycles, respectively.

Figure 4.9(a) presents a photograph of the specimen at the end of the test, in which some of the SECs were removed to clearly identify the crack tip. The locations of the crack tips identified from the four inspections are marked in Figure 4.9(a) and (b). The length of the crack was measured from the top end of the weld, as annotated in Figure 4.9(a). Crack lengths were approximately 19 mm (0.8 in.), 42 mm (1.7 in.), 62 mm (2.5 in.), and 84 mm (3.3 in.), respectively, at the time of the four inspections. This result indicates how the fatigue crack propagated over the 13 data collection intervals.

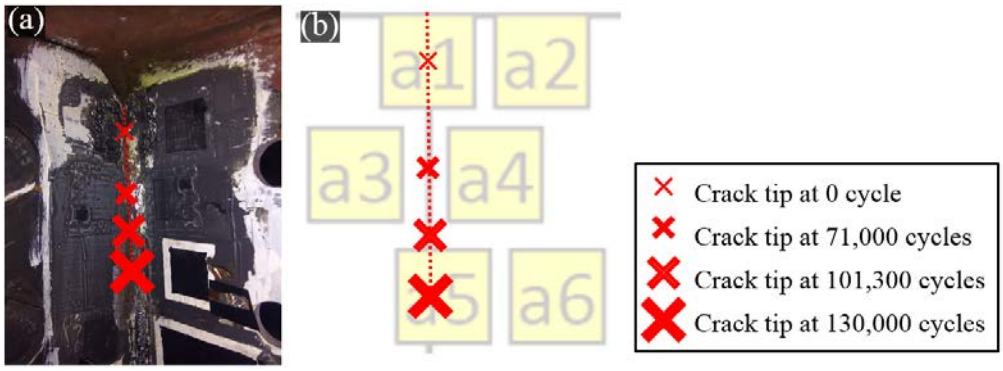

Figure 4.9: (a) Locations of the Crack Tips at Different Cycle Counts; (b) Illustration of Crack Tips with Respect to the Sensor Layout

SEC a1 was removed after 79,200 load cycles, as shown in Figure 4.10. The bonded side (i.e., the side in direct contact with the steel surface) of SEC a1 experienced damage during loading. In particular, a crack was identified in the conductive layer of SEC a1, exposing a white line that revealed the dielectric layer. This crack in the SEC was attributed to the large out-of-plane crack opening displacement under the sensor that repeatedly stretched the sensing skin during the test. Despite the occurrence of the crack in the conductive layer, SEC a1 continued providing capacitance data which will be illustrated in Figure 4.13.

Figure 4.10: Damaged SEC a1 after Removal

SEC a1 was Removed after 79,200 Load Cycles for a Detailed Inspection. On the bonded side (the side in direct contact with the steel surface) of the SEC, a crack was identified in the conductive layer, indicating damage to the SEC. The white color along the crack is the exposed dielectric layer.

4.5 Experimental Results

4.5.1 Representative Time-Series Measurements

Figure 4.11 presents a series of plots of representative time-series measurements of the SEC array taken from SECs a2 and a6. The plots present 10 seconds of measurements collected at 0 cycles (the beginning of the test) and 64,900 cycles. SEC a2 initially exhibited a larger peak-to-peak capacitance $\Delta C/C$ (Figure 4.11(a)), which became significantly smaller after 64,900 cycles (Figure 4.11(c)). This reduction may be attributed to the crack tip propagating away from SEC a2, causing strain relief around SEC a2 (Figure 4.9(b)). SEC a6, which was located in front of the crack propagation path, experienced an increased peak-to-peak capacitance, $\Delta C/C$, at 64,900 cycles due to higher strain caused by the crack tip moving closer to the sensor. A detailed full set of all SEC measurements can be found in Appendix B.

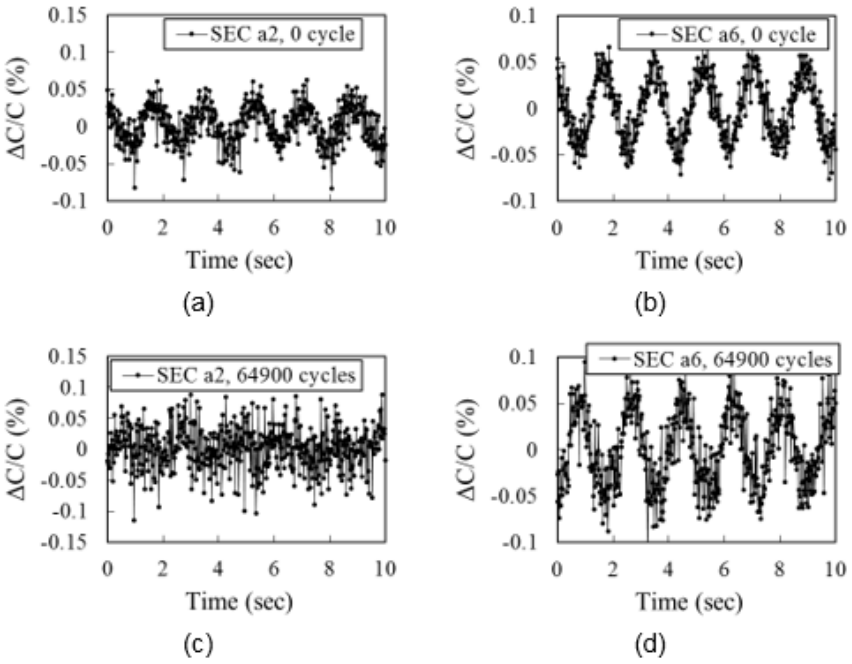

Figure 4.11: Representative Time-Series Measurements from the SEC Array
(a) SEC a2 at 0 Cycles; (b) SEC a6 at 0 Cycles; (c) SEC a2 at 64,900 Cycles; (d) SEC a6 at 64,900 Cycles

As discussed in Section 4.2.3, although peak-to-peak capacitance is a good indicator of fatigue crack growth, it is often times difficult to reliably identify in time-series signals due to the noise content. This can be observed in the signals plotted in Figure 4.11. Therefore, CGIs were extracted from the time-series signals through frequency analysis described in the next subsection.

4.5.2 CGIs from the SEC Array

4.5.2.1 CGIs from the Flat SECs

CGIs were extracted from the SEC array using the method introduced in Section 4.2.3. The strain measurement at the top chord of the cross frame was used to normalize the SEC measurements. Figure 4.12 shows the CGIs from the flat SECs at different numbers of load cycles. For clarity, results have been grouped based on the similarity of amplitude of CGI response.

As shown in Figure 4.12(a), CGIs from SEC a3 and a4 quickly increased at the beginning of the test and then gradually decreased. This phenomenon was a result of crack propagation

which initially brought the crack tip closer to a3 and a4 during the first three datasets collected (0, 15,000, and 21,500 cycles). The stress concentration around the crack tip increased the responses of nearby sensors. As the crack propagated further and the crack tip moved beyond a3 and a4, the stress relief along the fatigue crack path led to a decrease in the responses of these two sensors after 21,500 cycles.

Figure 4.12(b) shows the CGIs from SECs a6, a7, a8, a9, and a11, in which increasing CGIs were observed for all SECs. This increasing trend was due to increases in the strain field at these SECs caused by crack growth. Figure 4.12(c) illustrates the CGI change for SEC a2. As the crack propagated downward, stress relief along the crack path led to a decreasing trend of CGI as shown in the figure. This behavior is corroborated by comparing time-series measurements shown in Figure 4.11(a) and (c), in which the peak-to-peak capacitance decreased significantly at 64,900 cycles.

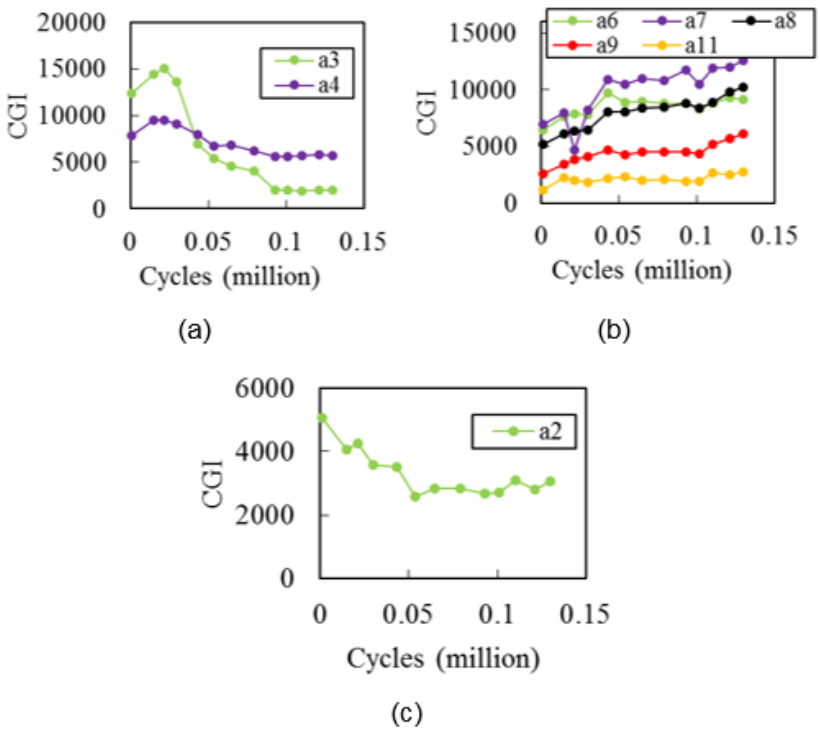

Figure 4.12: CGIs for (a) SEC a3 and a4; (b) SEC a6, a7, a8, a9, and a11; (c) SEC a2

4.5.2.2 CGIs from the Folded SECs

SECs a1, a5, and a10 were folded at the corner between the connection plate and the girder web. CGIs from these three SECs have been plotted in Figure 4.13. Only eight datasets were collected for SEC a1, after which the sensor was removed for a detailed inspection (see discussion in Section 4.4.4). SEC a1 exhibited significantly higher CGI responses than the other SECs. In addition, the CGIs from SEC a1 exhibited fluctuations during the test. This behavior is caused by the damage occurring in the sensing material of SEC a1 (Figure 4.10) provoked by the distortion-induced fatigue cracking.

SEC a5 also exhibited much larger CGI responses than adjacent flat SECs. The initial CGI from SEC a5 was approximately 14,400 while the CGIs from SEC a6 and a7 were approximately 6,500 and 7,000, as shown in Figure 4.12(b). This is due to the relative rotation between the connection plate and the girder web, which periodically stretches the sensing skin around the corner, provoking additional capacitance change to the SEC. In addition, the CGIs from SEC a5 (Figure 4.12(b)) steadily increased at the beginning of the test, and then decreased after 43,100 cycles. However, based on the observation illustrated in Figure 4.9(b), the fatigue crack reached SEC a5 at approximately 100,000 cycles and propagated to the center of SEC a5 at 130,000 cycles (end of the test). The CGI from SEC a5 continuously decreased during this stage despite the fact that the fatigue crack was growing under the sensing skin. A detailed discussion about the possible cause of this phenomenon can be found in Section 4.6.

Figure 4.13(c) shows the CGI from SEC a10, which is a folded sensor located far away from the fatigue crack. Large fluctuations were observed in the CGIs collected throughout the test from this SEC. The fluctuations may be attributed to the fact that SEC a10 was far away from the fatigue crack, and hence was less sensitive to the fatigue crack growth.

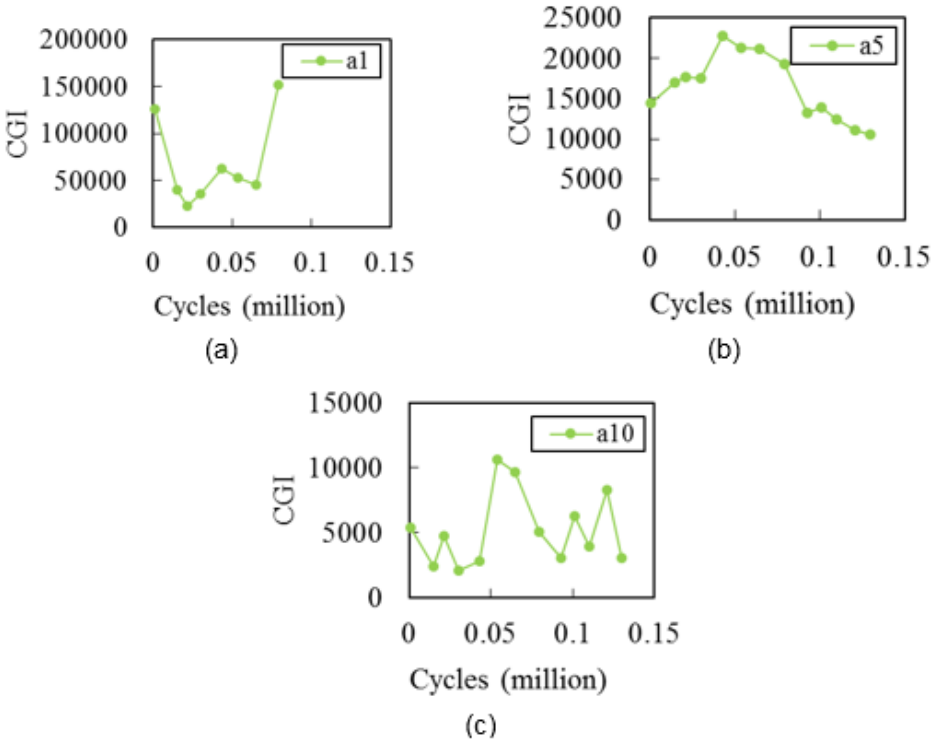

Figure 4.13: CGIs for (a) SEC a1; (b) SEC a5; (c) SEC a10

In summary, CGIs from folded SECs, initially deployed for directly detecting the crack growth, were unable to fulfill such a purpose (i.e., fluctuations of CGIs in SEC a1 and a10; decreasing CGIs when the crack grew into SEC a5). In this regard, only the flat SECs were adopted for constructing CGI maps, presented in the next subsection.

4.5.3 CGI Maps

CGI maps were constructed using CGIs from the SEC array. Figure 4.14(a) illustrates the flat SECs used in constructing the CGI maps. The dashed lines represent the boundaries of the CGI maps. A 2D coordinate system was created where the origin was at the top of the weld. Figure 4.14(b) schematizes the 15 cm × 25 cm (6 in. × 10 in.) region used as the boundary for the plots shown in Figure 4.15.

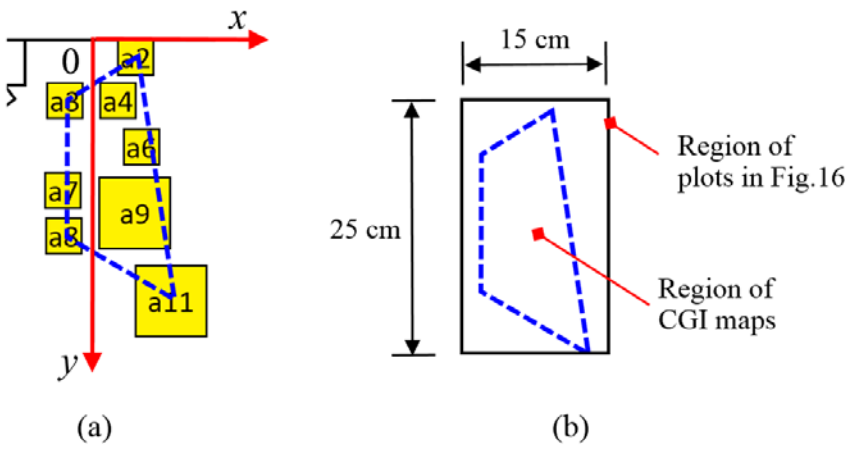

Figure 4.14: SECs for Constructing the CGI Maps

Figure 4.15 shows the resulting CGI maps. Due to significant differences in magnitudes of CGIs (e.g., the CGI was as large as 15,000 for SEC a3, and approximately 2,000 for SEC a11), the intensity in the CGI maps is represented in logarithmic scale. The CGI map covers a large area of fatigue susceptible region (10 cm × 20 cm). The crack tip locations were identified multiple times during the test, which are also marked with white X's in Figure 4.15(a), (h), (j), and (m).

Each plot in Figure 4.15 illustrates the distribution of CGI for the SEC array corresponding to each data collection interval, enabling a clear depiction of the fatigue damage over this large area. As the number of load cycles increases, the intensity in the CGI map changes. For instance, as the crack tip moved downward (shown in the progressions of Figure 4.15(a) to Figure 4.15(d)), higher intensities/brightness can be observed in the top-left region of the CGI map. However, as the crack continued to propagate, the top-left region became darker due to the stress relief along the crack path, as demonstrated in the progression shown in Figure 4.15(e) to 4.15(h). The bottom-left corner of the CGI map became brighter during crack propagation, evident in a comparison of Figure 4.15(h) and (m). This is due to the increasing strain field provoked by the propagation of the crack. By comparing the CGI map between the beginning and the end of the test (i.e., Figure 4.15(a) and 4.15(m)), significant changes in the location of high CGI intensity can be observed, indicating the fatigue crack propagation behavior during these 13 data collection intervals.

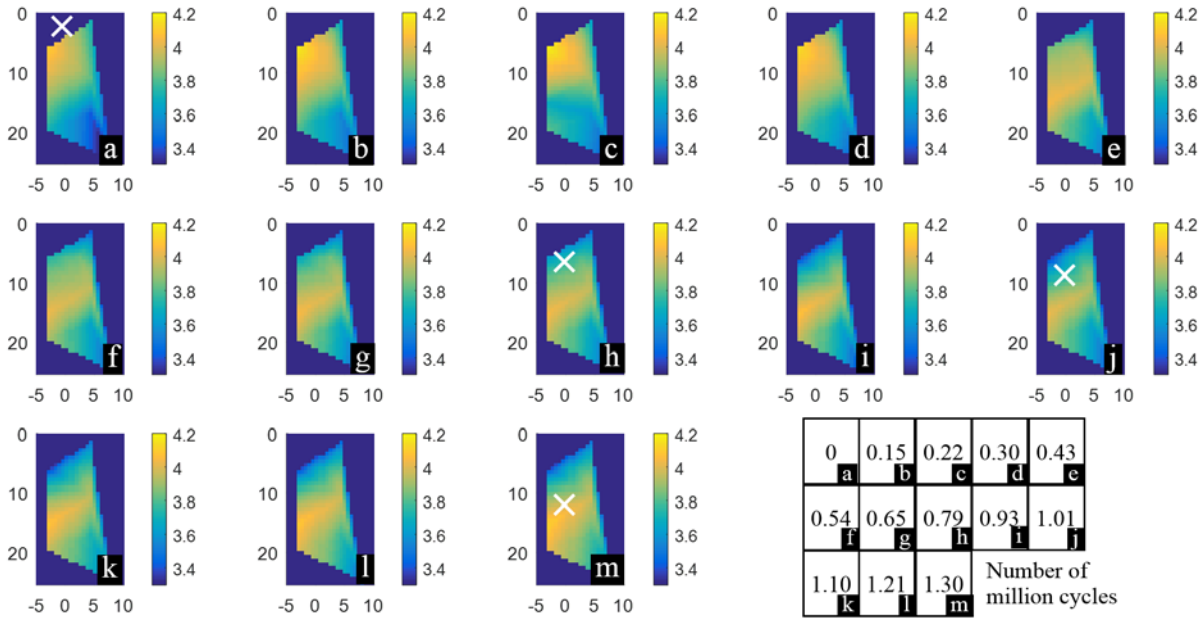

Figure 4.15: CGI Maps at the Top Region of the Connection Under Different Load Cycles
Note: The 'x' at (a), (h), (j), and (m) indicate the locations of the crack tips observed during the test. The number of load cycles associated with each plot is shown at the bottom-right corner of this figure.

4.6 Further Discussion on Folded SEC Sensors

This section investigates the potential source of the electromechanical behavior of the folded SEC a5 described in Section 4.5.2.2. SEC a5 was initially deployed for directly detecting the crack growth, but did not yield increasing CGIs when the crack propagated through the sensor. Figure 4.16 schematizes the layout of the test model, in which there is a skew angle of 40 degrees between the cross frame and the girder web. Due to the skewed configuration, the fatigue load *F* creates both a vertical movement of the cross frame and a horizontal rotation around the girder web, as illustrated in Figure 4.16(b). Such a rotational movement could lead to a supplemental change in capacitance of the SEC folded between the connection plate and girder web. As a result, the folded SEC a5 is subject to a combined effect of crack propagation and cross frame rotation, which may have contributed to the behavior of SEC a5.

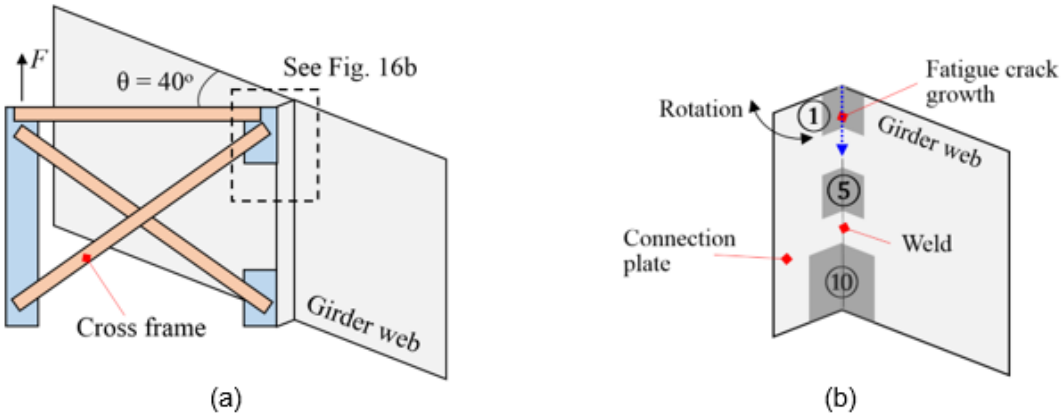

Figure 4.16: (a) Illustration of the Rotation between the Connection Plate and the Girder Web in the Tested Model; (b) Inset Detail at the Top Web Gap

Note: Other SECs not shown for clarity.

To further validate this hyporeport, an additional experimental investigation was performed on a non-skewed bridge girder to cross frame connection model, as shown in Figure 4.17(a). This new model is similar to the skewed one described in Section 4.4.1, except that the cross frame is perpendicular to the girder web, as denoted in Figure 4.17(a). The test model was symmetric about the cross frame. This non-skewed structural layout allowed the cross frame to maintain the vertical movement under the fatigue loading without being subject to the horizontal rotation around the girder web.

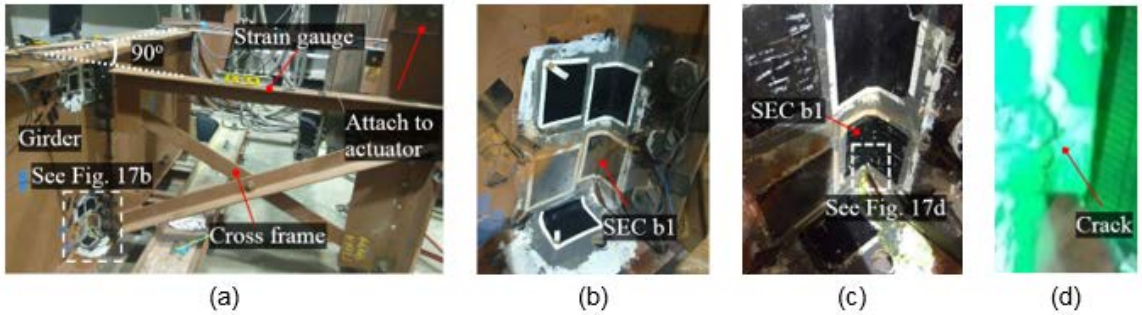

Figure 4.17: (a) Test Set-Up of the Non-Skewed Bridge Girder to Cross Frame Connection; (b) SEC b1 at the Bottom Region of the Connection; (c) SEC b1 was Removed for Crack Inspection after the Fatigue Test; (d) Crack Inspection Result

Note: Other SECs pictured in Figure 4.17(b) are not related to this study.

An SEC, denoted SEC b1 in Figure 4.17(b), was deployed in folded configuration along the weld between the connection plate and the girder web. A foil strain gauge was installed on

the top chord of the cross frame for normalizing the SEC's measurement. Prior to the test, the test model was inspected and no fatigue crack was detected. The test model was then fatigue loaded with 18,900 cycles with a load range of 2.2 kN to 25.5 kN (0.5 kip to 5.75 kip), leading to a newly-initiated fatigue crack beneath SEC b1. After the test, SEC b1 was removed to confirm the crack activity (Figure 4.17(c)). The fatigue crack is shown in Figure 4.17(d) under fluorescent dye penetrant.

During the test, 13 short time measurements of both the SEC and the strain gauge were collected for computing the CGIs. Utilizing the same CGI extraction method, CGIs of SEC b1 were computed and plotted in Figure 4.18. A clearly increasing trend of CGIs is observed in the figure, indicating SEC b1 was able to successfully monitor the crack growth, despite its folded configuration.

A comparison between the two tests with folded SECs under the skewed and non-skewed bridge configurations reveals that the rotational movement occurring between the girder web and connection plate led to the inability of the folded SEC a5 to provide consistently increasing CGIs under crack propagation. When no such rotational movement is occurring, as is the case for the non-skewed configuration, the folded SEC b1 was able to provide robust CGIs to monitor crack growth. Therefore, folded configuration of the SECs is only recommended to use in non-skewed bridge configurations or in ones with small skewness that have limited rotations.

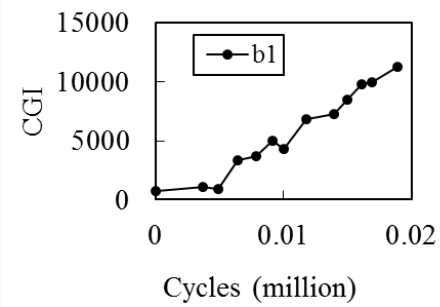

Figure 4.18: CGIs from SEC b1 in the Non-Skewed Bridge Girder to Cross Frame Connection

4.7 Conclusions

This chapter presented a novel strain-based approach for sensing out-of-plane distortion-induced fatigue cracks in steel bridges using soft elastomeric capacitor (SEC) arrays. The SEC is a large-area and flexible sensing skin, able to measure a wide range of strains over large structural surfaces. Previous investigations have verified the ability of a single SEC for sensing an in-plane fatigue crack in a small-scale specimen. In this study, we further demonstrated the ability of the SEC technology in the context of sensing distortion-induced fatigue cracks, which represent the majority of fatigue cracks in aging steel highway girder bridges in the United States.

With the proposed strategy, multiple SECs in the form of a sensor array were deployed to cover a large fatigue-susceptible region. Subsequently, a fatigue-sensing algorithm was proposed by constructing a Crack Growth Index (CGI) map from the measurements of the SEC array. The effectiveness of the SEC array coupled with the CGI map was then experimentally validated through a fatigue test of a bridge girder to cross-frame connection model subjected to distortion-induced fatigue. Test results verified that by deploying the SEC array, multiple CGIs can be obtained over the fatigue-susceptible region, offering a comprehensive picture of the fatigue damage. Furthermore, through monitoring the evolution of CGI maps constructed under different fatigue load cycles, the fatigue crack growth can be clearly visualized by identifying the intensity changes in the CGI maps.

Comparison between the skewed and non-skewed bridge configurations also indicated that the horizontal rotation between the connection plate and the girder web can affect the effectiveness of the folded SEC for directly monitoring crack growth along the corner of the connection. This observation provides an important guideline for applying the SECs in folded configuration in future field applications.

Chapter 5: Development of a Wireless Capacitive Sensing Board

5.1 Overview

In this chapter, we developed a wireless sensor board to integrate the SEC sensor with wireless sensing for crack monitoring. This sensor board converts low-level dynamic capacitance variations into analog voltage signals. The board is designed to interface with the Xnode wireless platform utilizing its power supply (3.3 V), analog-to-digital conversion, onboard signal processing, and wireless data communication capabilities. The hardware design consists of an AC-excitation, a precisely balanceable AC-based De-Sauty Wheatstone bridge circuit, a two-step signal amplifier, an AM demodulation circuit, and a series of filtering circuits. A dual-step shunt calibrator has also been proposed to remove the parasitic capacitance effect of the lead wires during the on-board calibration process. The prototype of the sensor board has been developed. The performance of the wireless sensor board in combination with the SEC sensor in dynamic capacitance sensing has been validated through a series of shake table tests and compared with an off-the-shelf wired capacitance measurement kit.

5.2 AC Wheatstone Bridge-Based Capacitive Strain Sensor Board Design

Resistance-based strain can be measured using a DC Wheatstone bridge. However, if the bridge circuit is composed of capacitors or a combination of resistors and capacitors, only the AC can be used to excite the bridge. Therefore, an AC Wheatstone Bridge was employed to convert capacitance variation into analog voltage change. To measure the low-level capacitance variation of the SEC sensors under micro-level structural strain change, a two-step analog signal amplification has been employed. In addition, an AM demodulation circuit was utilized to account for the dynamic variations of the capacitance value manifested in the form of modulated signals. This section elaborates on the AC-based dynamic capacitance sensing principle, hardware design, and theoretical analysis of AC Wheatstone bridge configuration in detail.

5.2.1 Sensing Principle of Soft Elastomeric Capacitor

The soft elastomeric capacitor (SEC) is a skin-type flexible strain sensor that transduces surface strain to a change in capacitance. It is fabricated using a stretchable polymer-based dielectric sandwiched by stretchable electrodes. The capacitance changes corresponding to change in geometry (area and thickness) of the sensor can be expressed by Equation 5.1, depending on surface area A, thickness d, vacuum permittivity ε_0, and dielectric permittivity ε_M.

$$C = \frac{\varepsilon_0 \varepsilon_M A}{d}$$

Equation 5.1

The SEC enables mesosystem monitoring for civil structures with several advantages, such as large coverage area, low cost, durability, and flexibility. Several studies (Kong et al., 2017; Laflamme et al., 2012; Laflamme et al., 2013; Laflamme et al., 2014; Saleem et al., 2015) have shown promising performance for mesoscale and fatigue monitoring.

In this study, two sizes of SECs, 1.4 in. × 1.4 in. and 3 in. × 3 in., as shown in Figure 5.1, are used for validation tests. Each SEC is installed on the steel plate member of a lab-scale shear building along with a foil-type strain gauge to serve as a reference, which will be further discussed in Section 5.3.

Figure 5.1: Two Sizes of SEC: 1.4 in. × 1.4 in. (left); 3 in. × 3 in. (right)

5.2.2 Xnode Wireless Sensing Platform

The new capacitance sensor board is designed to work with the Xnode wireless sensor platform developed as a part of the Illinois Structural Health Monitoring Project (ISHMP; Spencer et al., 2017). The Xnode was selected from various wireless sensor platforms due to its

many attractive features, such as reliable wireless communication, high-fidelity Analog-to-Ditigal converter (ADC), expandable data storage, high-precision synchronized sensing, user-configurable middleware software library, automated long-term operation of wireless network, and so on. It is equipped with an LPC4357 (ARM Cortex M0/M4) microprocessor with frequencies up to 204 MHz, a 24-bit low-noise ADC (TI ADS131E8), a 2.4 Ghz low-power wireless radio transceiver (Atmel AT 86RF233), and it supports up to five analog input channels. In addition, it is powered by a high-capacity rechargeable battery with solar panel support. The sensor platform also provides a power supply port to feed 3.3 V to external sensor boards.

5.2.3 Considerations for High-Sensitivity Capacitance Sensing

The first step of capacitance-based strain sensing is the conversion of capacitance change into analog voltage change. Considering the fact that the capacitance variation of an SEC for micro-level strain responses of civil structures is below 1%, the sensor board needs to have sufficiently high signal amplification. Based on these requirements, an AC bridge circuit has been employed with high-precision bridge balancers and a two-step amplifier.

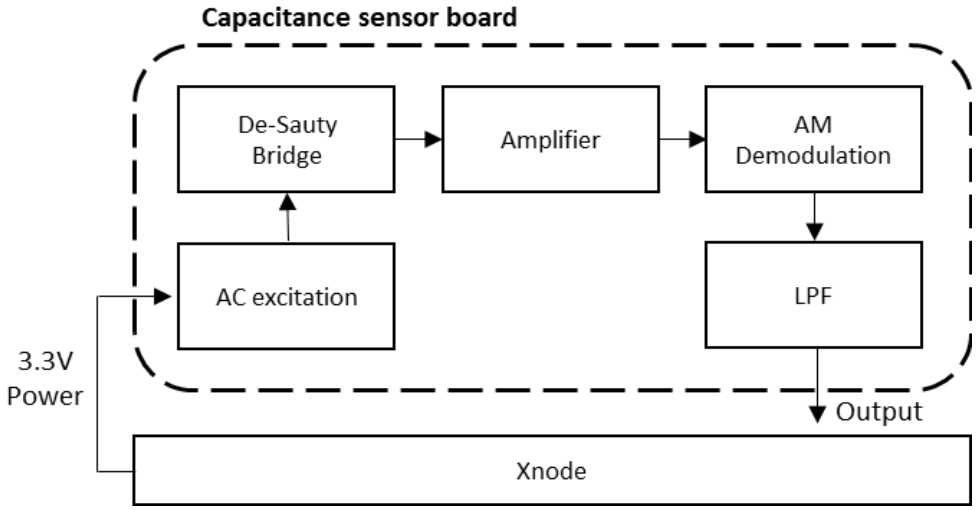

Figure 5.2: Block Diagram of the Wireless Capacitive Strain Sensing Module

The second consideration was the compatibility with the Xnode platform. The new sensor board has been designed to interface with the Xnode to use its high-fidelity sensing capability enabled by the 24-bit ADC and the regulated 3.3 V power supply. The analog voltage output

from the sensor board can directly be processed by the Xnode ADC. The two-step amplifier can be set (i.e., by controlling the sensitivity) to produce a 0~2.4 V range output (the measurement range of Xnode) after AM demodulation under micro-level strain changes. Because of the AC bridge mechanism, the differential voltage from the Wheatstone bridge arms is the amplitude modulated (AM) signal. Therefore, an AM demodulation circuit is employed to extract the actual dynamic signals so as to recover the dynamic capacitance variation from the modulated signals. Subsequently, an analog low-pass filter is applied to obtain a cleaner output in the desired sensing bandwidth. Figure 5.2 shows the block diagram of the sensor module demonstrating the capacitance sensing principle and interfacing with the Xnode platform.

5.2.4 AC Wheatstone Bridge

As mentioned previously, high sensitivity is essential for capacitive strain sensing using SECs. To achieve the required sensitivity, a precisely controllable AC Wheatstone Bridge circuit was designed as illustrated in Figure 5.3.

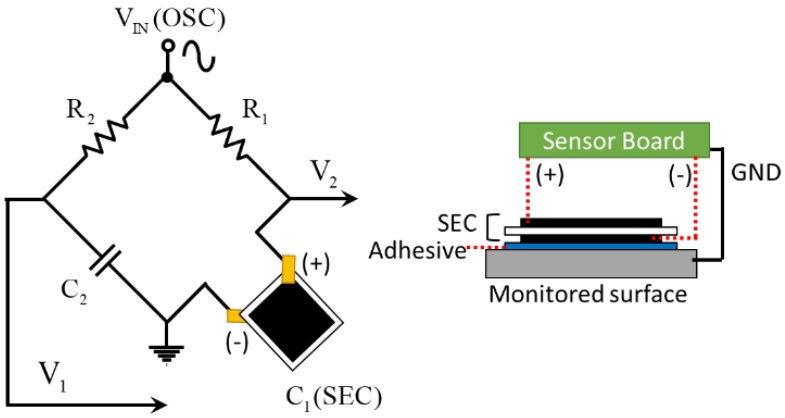

Figure 5.3: De-Sauty Bridge Configuration: Grounding Measurement Scheme

The AC Wheatstone Bridge with two capacitors and two resistors, the simplest AC bridge configuration for comparing two capacitor values, is known as the De-Sauty Bridge. In this design, a grounding scheme in which a sensor is located at the grounding side is employed to minimize the noise. The SEC has two stretchable electrode layers at the top and bottom surfaces with copper tapes used to make connections with the DAQ. The top layer is used for the (+)

input to the DAQ and the bottom layer is used for the (−) as the ground. The SEC is very sensitive to the electromagnetic and environmental noise, hence the sensor board is designed to share its ground with the whole circuit.

In this design, a sine wave AC signal is used to excite the bridge circuit. Considering the cost effectiveness and difficulties in finding a proper sine wave chip with the required bandwidth of the amplifier, a scheme that converts a square wave to a sine wave is employed. This strategy utilizes a 32.768 kHz square wave oscillator with a 4th-order Sallen-key low pass filter for square wave to sine wave conversion. The De-Sauty Bridge is composed of a reference capacitor (C_2), an SEC (C_1, i.e., variable capacitor), and two potentiometers as variable resistors (R_1 and R_2) for bridge balancing as shown in Figure 5.4. One of the capacitors is the sensor (DUT, Device Under Test), while the other is the reference (quarter bridge). The final output signal (i.e., ΔV_{out}) from the De-Sauty bridge with the two-step amplifier can be derived as follows. First, by using the configuration in Figure 5.4, the balanced condition is $R_2 / R_1 = C_1 / C_2$. The initial state voltage (no strain) of bridge $V_{initial}$ can be expressed as:

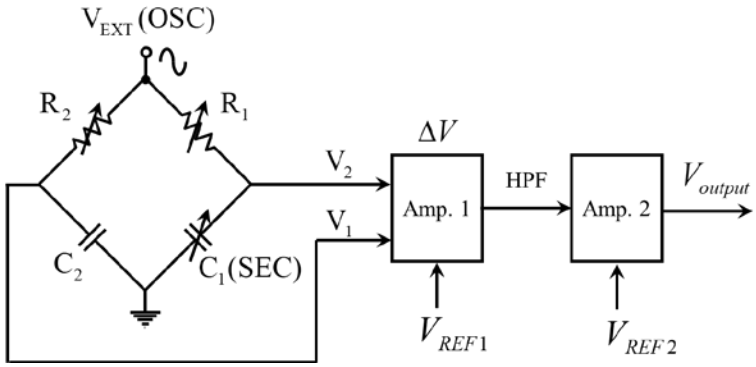

Figure 5.4: De-Sauty Bridge and Two-Step Amplification Design

$$V_{initial} = V_{EXT}\left(\frac{\frac{1}{j\omega C_2}}{R_2 + \frac{1}{j\omega C_2}} - \frac{\frac{1}{j\omega C_1}}{R_1 + \frac{1}{j\omega C_1}}\right)$$

Equation 5.2

And when the capacitance of SEC increases by ΔC the total capacitance of the SEC sensor is $C_1^{'} = C_1 + \Delta C$ and the voltage under test (strain) of the bridge is:

$$V_{test} = V_2 - V_1 = V_{EXT}\left(\frac{\frac{1}{j\omega C_2}}{R_2 + \frac{1}{j\omega C_2}} - \frac{\frac{1}{j\omega\left(C_1 + \Delta C\right)}}{R_1 + \frac{1}{j\omega\left(C_1 + \Delta C\right)}}\right)$$

Equation 5.3

Rearranging terms in Equation 5.3 yields:

$$V_{test} = V_{EXT}\left(\frac{j\omega\left(C_1R_1 - C_2R_2\right) + j\omega\Delta CR_1}{\left(1 + j\omega C_1R_1 + j\omega\Delta CR_1\right)\left(1 + j\omega C_2R_2\right)}\right)$$

Equation 5.4

For a balanced status, $C_1R_1 - C_2R_2$ is zero, and according to the SEC sensitivity, the capacitance change ΔC is very small compared with the nominal capacitance of the SEC; thus, ΔC can be neglected in the denominator of Equation 5.4, resulting in the following equation:

$$V_{test} = V_{EXT}\left(\frac{j\omega R_1}{\left(1 + j\omega C_1R_1\right)\left(1 + j\omega C_2R_2\right)}\Delta C\right)$$

Equation 5.5

Equation 5.5 gives a linear expression converting a change in capacitance into a change in voltage.

Because the capacitance change is very small, an amplification is necessary. However, due to the parasitic effect, the balance could not be perfectly achieved, which means there is always a DC component in the output signal from the bridge circuit. Therefore, a two-step amplification is proposed in this design. As illustrated in Figure 5.4, two AD8226 were employed for the two-step amplification due to their low cost, appropriate power supply range (2.2 V to 36 V), proper bandwidth (1.5 Mhz), and sufficient amplification capability up to 1,000 times. The two-step amplification can be expressed in Equation 5.6.

$$\Delta V_{output} = G_2 \cdot \left\{\left(G_1 \cdot \Delta V + V_{REF1}\right) - V_{HPF}\right\} + V_{REF2}$$

Equation 5.6

Differential voltage from the De-Sauty bridge is amplified by the two-step amplification with gain factors G_1 and G_2 drifted by V_{REF1} and V_{REF2}. Between the two stages, a high-pass filter is employed to eliminate the DC component of the signal output from the first stage amplifier by subtracting the DC components for pure AC amplification. In the second amplification stage, an unbiased AC signal was amplified and drifted again by V_{REF2} for the output level control.

5.2.5 AM Demodulation and Low Pass Filtering

According to Equation 5.6, the output signal from the amplification part would be an amplitude-modulated (AM) sine wave. Therefore, amplitude envelope detection is employed to make the final voltage proportional to the capacitance change. Figure 5.5 shows the circuit for the amplitude envelope detection.

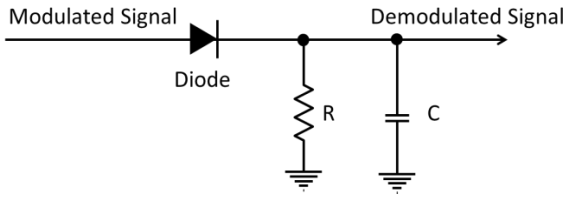

Figure 5.5: Demodulation Circuit for Amplitude Envelope Detection

In this circuit, the values for *R* and *C* should be carefully selected to ensure the demodulated signal reflects the actual one (i.e., dynamic capacitance variation of the SEC). In this board design, the target frequency bandwidth of the structural response signal is 0~40 Hz. On the other hand, the carrier frequency of the modulated signal that comes from the AC sine-wave excitation for the bridge is much higher than the message frequency. Therefore, to extract the message from the modulated signal, the relationship shown in Equation 5.7 must be satisfied.

$$\frac{1}{f} \ll \tau = RC \ll \frac{1}{\omega} \qquad \textbf{Equation 5.7}$$

Where:

f is the frequency of the carrier,

ω is the bandwidth of the message, and

τ is the charging time of the RC circuit.

In addition, a third-order active LPF using the Sallen-Key configuration has been incorporated after the AM demodulation for cleaner final outputs.

5.2.6 Prototype Sensor Board

Figure 5.6 shows the prototype sensor board based on the circuits described above. Each component has been described in Figure 5.2 through Figure 5.4 according to its function. The potentiometers were soldered on the back side of the sensor board. To achieve low-level noise

performance, a low-noise OP-Amp, TI OPA4344 was used. For amplifier gain control and DC drift, analog potentiometers were used, which consequently allowed for compatibility with various levels of nominal capacitance of the SECs depending on their geometry.

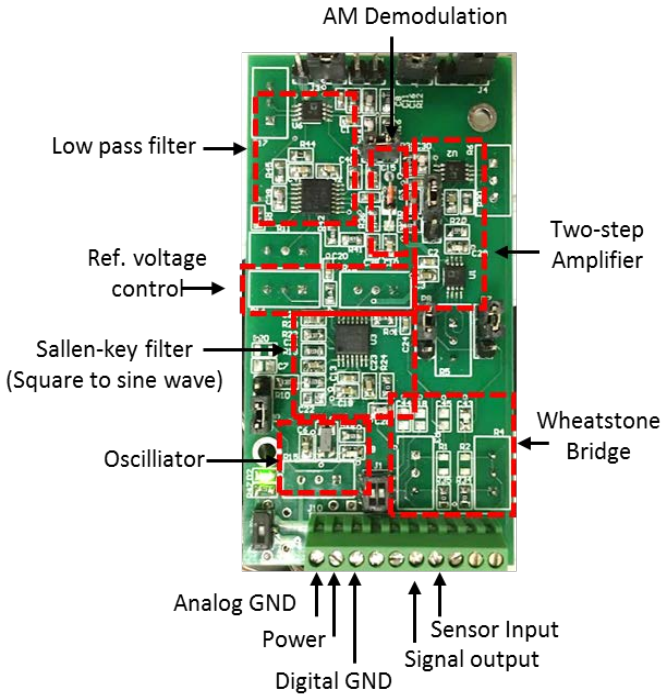

Figure 5.6: Top View of the Capacitance Sensor Board

5.3 Experimental Validation

Performance evaluation of the capacitance sensor board was conducted by employing a static noise test and a series of dynamic tests. While various sizes of SECs were available, SECs with dimensions of 1.4 in. × 1.4 in. (nominal capacitance: 210 pF) and 3 in. × 3 in. (nominal capacitance: 870 pF) were selected for the validation tests. For these tests, an eight-story shear building with steel plate columns was used. An APS400 Electrodynamic shaker with an APS145 amplifier was used to generate the dynamic excitation.

The SECs and a foil-type resistive strain gauge were installed on the exterior surface of a steel plate column on the 1st floor as shown in Figure 5.7. Wireless capacitive measurements were compared with a commercial wired capacitance measurement kit PCAP02, which is based

on an oscillator with digital inverter having a noise level of 116 aF RMS under the 250 Hz sampling rate.

For comparison, strain responses were measured by an OMEGA KFH-3-120-C1-11L3M3R, which is a foil-type strain gauge having a nominal resistance of 120±0.35Ω, in combination with a National Instruments CompactDAQ with the universal strain gauge input module (NI9235). A static noise test was conducted to estimate the noise floor of the sensor board with the Xnode. For dynamic performance evaluation, each SEC was tested under a cyclic sine-wave excitation with four-step amplitude increments shown in Table 5.1. For each test case, the sensor board was precisely balanced and amplified with calibration factors (pF/mV) shown in Table 5.1.

Table 5.1: Excitation History (μs) and Calibration Factor (pF/mV)

Test Case	Step 1	Step 2	Step 3	Step 4	Calibration Factor
Case1 1Hz	110	210	350	710	0.0100
Case1 5Hz	110	205	370	500	0.0056
Case2 1Hz	90	170	300	600	0.3003
Case2 5Hz	80	160	300	400	0.4000

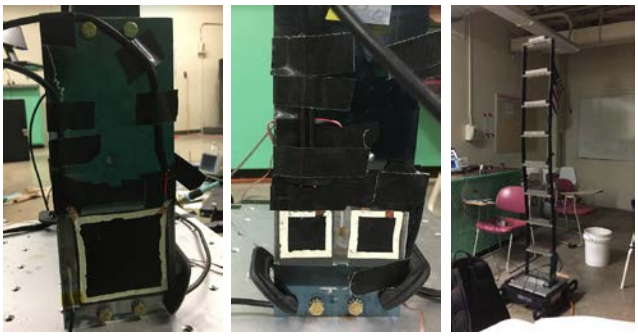

Figure 5.7: Test Specimens, Shear Building on a Shake Table

5.3.1 Static Noise Test

First, the noise floor of sensor board was evaluated. The capacitance change of the SEC under micro-strain level deformation was very small, hence low noise performance is critical. The ambient RMS noise was measured as 0.12 mV (corresponding to 1.2 fF) over the 20 Hz bandwidth as shown in Figure 5.8.

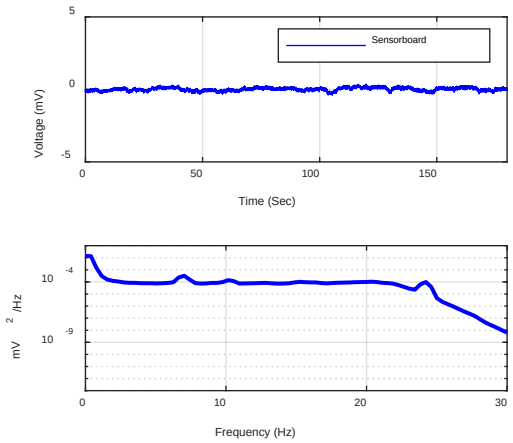

Figure 5.8: Static Noise Test Result: Sampling Rate = 100 Hz, Cut Off Frequency = 20 Hz

5.3.2 Dynamic Step-Load Test Case 1: Small SEC

Dynamic performance of the new sensor board was evaluated by applying cyclic step-load tests. A series of dynamic test results from the three DAQs (i.e., NI DAQ, PCAP02, and Xnode) for small SEC tests are compared in Figure 5.9 and Figure 5.10. For each test, the De-Sauty bridge was precisely balanced. As can be observed in Figure 5.9(a) and Figure 5.10(a), the measurements taken by the new sensor board showed strong agreement with conventional strain gauge measurements for all excitations with different amplitudes and frequencies. Compared with the PCAP02 measurements, the new sensor board showed cleaner (lower noise) results as shown in Figure 5.9(b) and Figure 5.10(b). The PCAP02 measurement showed relatively more noisy results under high frequencies; the noisy measurements are particularly obvious for low amplitude responses.

The maximum capacitance variation under dynamic excitation was observed to be 1.11 pF, which can be converted to a 0.5% variation at the 710 micro-strain level. Considering the clean measurement from the sensor board under the small strain level (110 micro strain, 0.11 pF), the sensor board is capable of measuring capacitance changes below 0.05%.

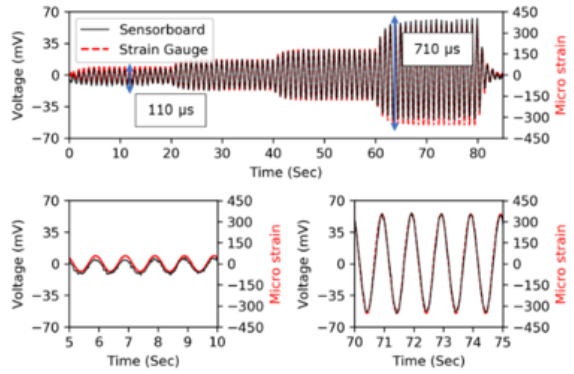

(a) Comparison between sensor board and strain gauge

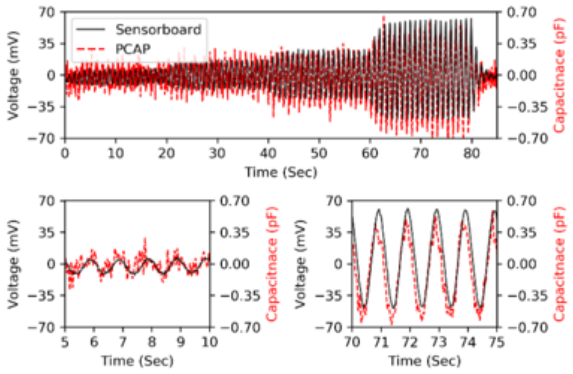

(b) Comparison between sensor board and PCAP02

Figure 5.9: Test Results with Small SEC for 1 Hz Excitation

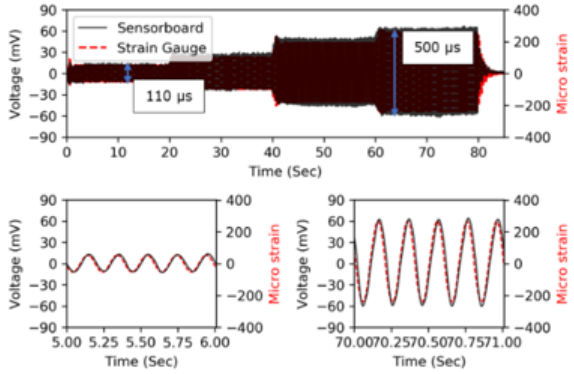

(a) Comparison between sensor board and strain gauge

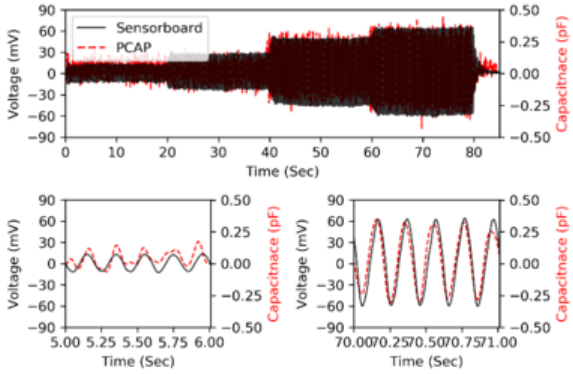

(b) Comparison between sensor board and PCAP02

Figure 5.10: Test Results with Small SEC for 5 Hz Excitation

5.3.3 Dynamic Step-Load Test Case 2: Large SEC

While small SECs exhibited good sensitivity, a large-size SEC was also tested under the same condition. A large SEC is advantageous in that it can cover a larger area for mesoscale sensing.

Figure 5.11 and Figure 5.12 show that maximum capacitance variation under an excitation of 600 micro-strain was about 2.6 pF, which can be converted to a 0.3% variation of the 870 pF nominal capacitance for the large SEC. Good agreements were still observed among

the three measurement systems, but the large SEC showed noisier data than the small SEC shown in Figure 5.9 and Figure 5.10. The difference may be attributed to the fact that the increased SEC area is subjected to more electromagnetic (EM) field noise from the lab environment. Also, the large SEC provides average strain measurements for the 3 × 3 in.^{2} area on the plate surface, while the strain gauge and small SEC measure more localized responses.

For the 90 micro-strain deformation (i.e., the amplitude in the first step), the sensor board measured capacitance variation with a 2.5 mV amplitude as shown in Figure 5.11 and Figure 5.12. Considering the RMS noise of the sensor board was 0.12 mV, it was sufficient to effectively resolve a 2.5 mV signal.

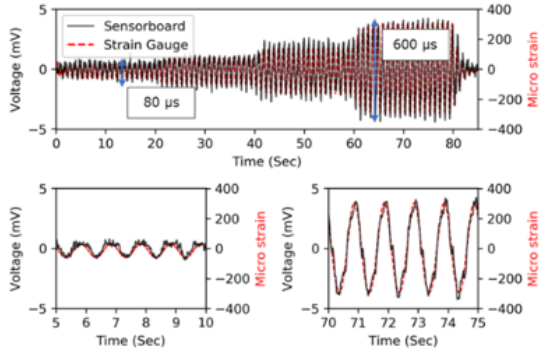

(a) Comparison between sensor board and strain gauge

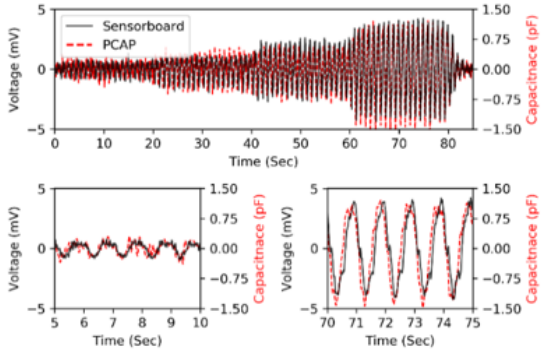

(b) Comparison between sensor board and PCAP02

Figure 5.11: Test Results with Large SEC for 1 Hz Excitation

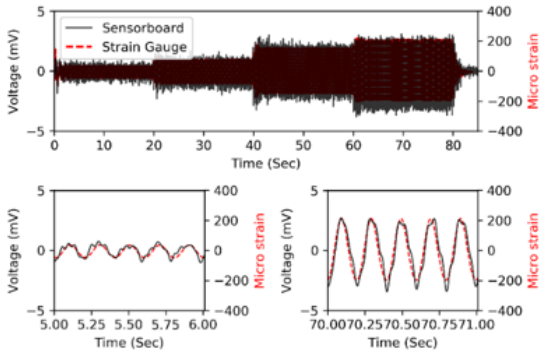

(a) Comparison between sensor board and strain gauge

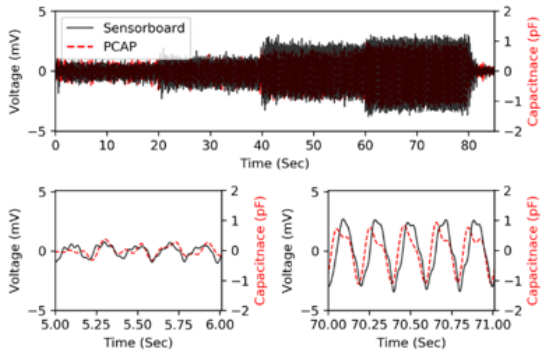

(b) Comparison between sensor board and PCAP02

Figure 5.12: Test Results with Large SEC for 5 Hz Excitation

5.3.4 Dynamic Random Load Test: Large SEC

Additionally, the new sensor board was tested under random excitations to evaluate its performance under ambient structural responses. A 20-Hz band-limited white noise was used for the excitation. For comparison, a 3 in. × 3 in. SEC was used for performance evaluation. The sensor board was balanced with a calibration factor of 0.2141 for this case. Test results showed strong agreement with conventional strain gauge measurement as shown in Figure 5.13(a), and the performance was even better than the PCAP02 from the noise perspective, as shown in Figure 5.13(b). The small amplitude difference observed in parts of the time histories may be attributed to the larger area of the SEC.

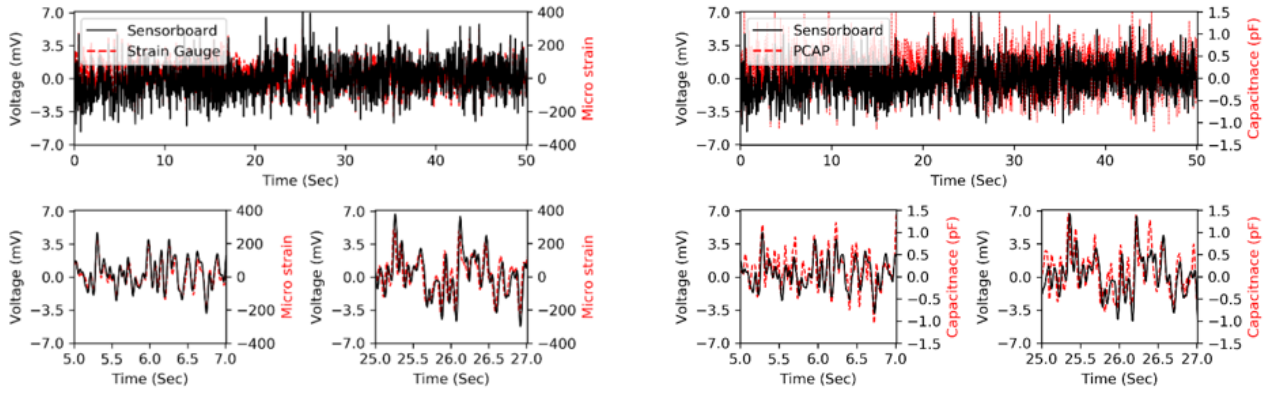

(a) Comparison between sensor board and strain gauge

(b) Comparison between sensor board and PCAP02

Figure 5.13: Test Result of the Random Excitation Case

Figure 5.14 shows a comparison of the measurements in the frequency domain. In particular, auto power spectral density (APSD) was used to evaluate the noise floor of each data set. All three measurements successfully identified the natural frequency peaks of the shear building, but showed differences in the noise floor. As shown in Figure 5.14, the strain gauge data showed the clearest peaks with the lowest noise level. The SEC measurements from both the PCAP02 and the sensor board captured the natural frequency peaks clearly but showed higher noise floor levels. Nonetheless, as expected, the sensor board showed a lower noise floor than the PCAP02 over the whole frequency range.

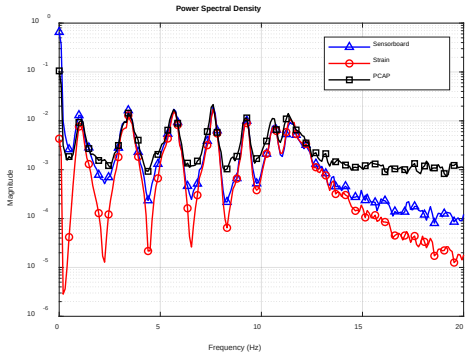

Figure 5.14: PSD Comparison of the Random Excitation Case

5.4 Modified Shunt Calibration Circuit

For field applications, a calibration circuit is necessary to convert the output voltage to absolute capacitance. For capacitance-based Wheatstone bridge circuit, traditional shunt calibration using single capacitor does not yield accurate results due to parasitic resistance and capacitance existing in the wires for sensor connection. In order to eliminate this effect, a modified shunt calibration circuit was proposed using two fixed-value capacitors.

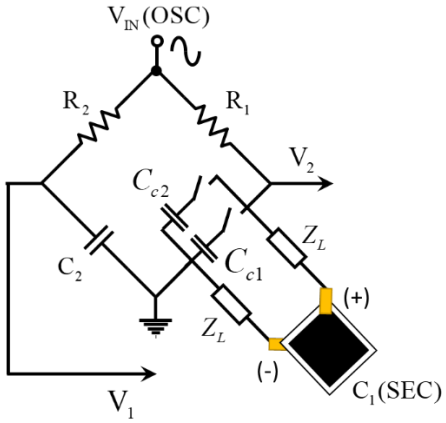

Figure 5.15: The Proposed Modified Shunt Calibration Circuit

Figure 5.15 shows the modified calibration circuit showing two capacitor arrangements for shunt calibration. Assuming $V_{initial}$ is the initial voltage output from the bridge circuit, $\Delta V_{C_{c1}}$ is the voltage output change from the bridge circuit due to the first paralleled capacitor for calibration (C_{c1} is short and C_{c2} is open) considering the parasitic impedance of wire, as shown in Equation 5.8:

$$\Delta V_{Cc1} = V_{Cc1} + V_{wire} - V_{initial}$$ **Equation 5.8**

$\Delta V_{C_{c2}}$ is the voltage output from the bridge after connecting the second capacitor for calibration (C_{c1} is open and C_{c2} is short):

$$\Delta V_{Cc2} = V_{Cc2} + V_{wire} - V_{initial}$$ **Equation 5.9**

The net output voltage changes from the two-step calibration can be expressed as:

$$\Delta V_{C_{c1}-C_{c2}} = (V_{C_{c1}} + V_{wire} - V_{initial}) - \left(V_{C_{c2}} + V_{wire} - V_{initial}\right) = V_{C_{c1}} - V_{C_{c2}}$$ **Equation 5.10**

By summarizing the above equations, a calibration factor for voltage to capacitance conversion can be obtained as:

$$\Delta C = \left(\frac{C_{c1} - C_{c2}}{V_{Cc1} - V_{Cc2}}\right)\Delta V$$ **Equation 5.11**

5.4.1 Validation of the Modified Shunt Calibration Circuit

To validate the proposed modified shunt calibration circuit, two cases of calibration tests were conducted and the results were compared with the direct capacitance measurements of a large SEC. 5 pF and 1 pF capacitors were selected as the shunt calibration capacitors which yield a 4 pF capacitance difference. For each case the bridge circuit has a different balance and amplification, and hence needs to be calibrated prior to performing actual measurements. From the shunt calibration tests (as illustrated in Figure 5.16), the voltage-to-capacitance conversion coefficients were achieved as 2.35 mV/pF for Case 1 and 3.25 mV/pF for Case 2.

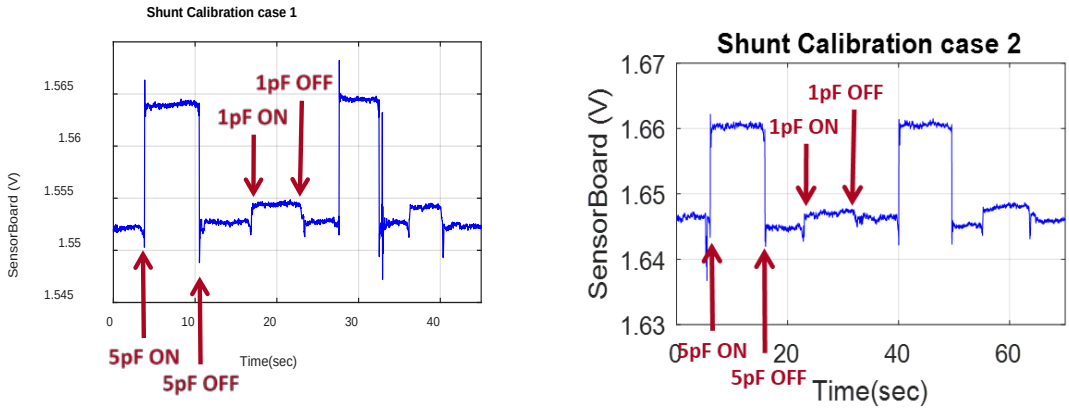

Figure 5.16: Shunt Calibration Voltage Outputs for the Two Test Cases

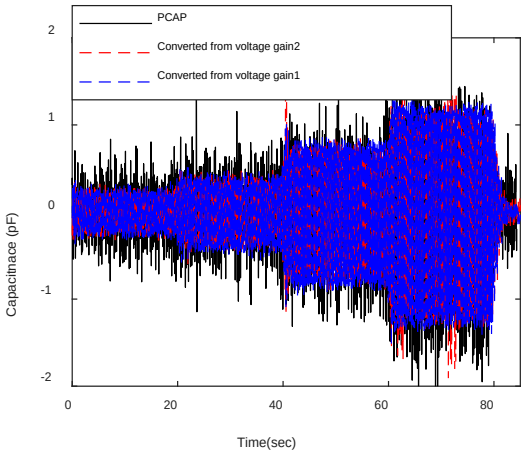

Figure 5.17: Comparison Among Sensor Board Measurements and PCAP Measurement

By using the achieved calibration coefficients, dynamic tests with cyclic sine-wave excitations were conducted using the same four-step amplitude increments as those applied in Section 5.3.3. The raw voltage measurements from the sensor board were converted to capacitance with the calibration coefficients. Figure 5.17 shows the capacitance measurements comparison between the PCAP measurement and the sensor board measurements converted using the two calibration coefficients. All three cases showed good agreement indicating the modified shunt calibration successfully converted voltage to capacitance with good accuracy.

5.5 Sensor Board Manufacturing and Quality Tests

Twenty capacitance sensor boards have been manufactured and tested for quality verification. The sensor board performance was evaluated by the incremental dynamic step-load

test and the shunt calibration test. The quality test results were quite consistent with minor variations. Each sensor board was numbered and labeled with performance result. Among the 20 sensor boards, seven sensor boards were configured for the large SECs, 10 sensor boards were configured for the small SECs, and three sensor boards were kept for future tests.

5.5.1 Manufactured Sensor Boards

Figure 5.18 shows the 20 sensor boards manufactured by Bittele Electronics (a circuit board manufacture company, www.7pcb.com) which were shipped to the University of Arizona. Hardware assemblies for all sensor boards were in good condition.

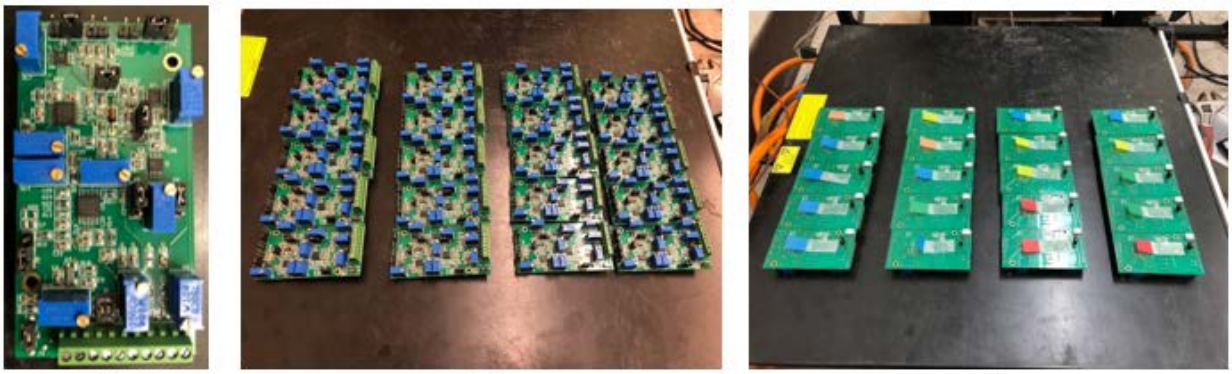

Figure 5.18: Manufactured Sensor Boards
(a) One of the Sensor Boards (detail); (b) 20 Board Array (top side), (c) 20 Board Array (bottom side)

5.5.2 Quality Test Setup

To evaluate the hardware quality, several performance tests were conducted, including the incremental dynamic step-load test and shunt calibration test as shown in Figure 5.19. Large SEC (3 in. × 3 in.) and small SEC (1.4 in. × 1.4 in.) were used for the sensor board performance tests.

A total of 17 sensor boards were validated for the Kansas team's field test. Each sensor board was assigned a number from to #1 to #7 for large SEC setup, and #8 to #17 for small SEC setup.

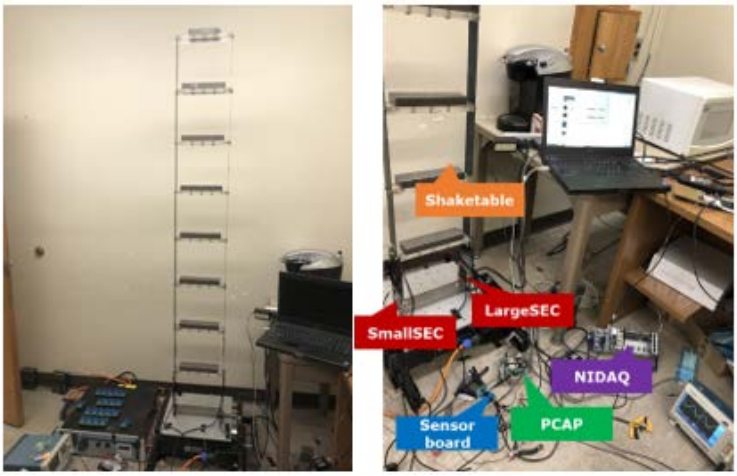

Figure 5.19: Test Setup

5.5.3 Incremental Dynamic Step-Load and Shunt Calibration Test for Large SEC Setup

1-Hz sine wave with incremental step load was provided to the shear building via shake table APS400. Each step load sinewave was applied for 20 seconds and the amplitude was increased by 85 / 135 / 280 / 450 μ-strain. After the step load test, the shunt calibration test was conducted to convert measured voltage from sensor board into absolute capacitance value. Double-step shunt calibration process with 5 pF and 1 pF capacitors was employed. A resistive-type strain gauge was installed to provide reference measurements (Figure 5.20), and the measurements by the sensor board and the PCAP were compared each other.

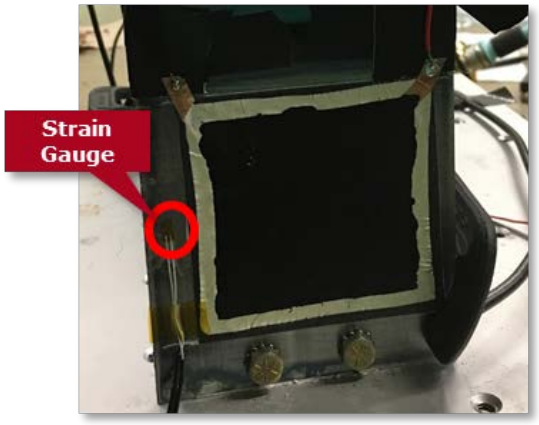

Figure 5.20: Strain Gauge Installation

Figure 5.21 shows the example test result of the sensor board #1. The plot on the first row shows raw measurements during the shunt calibration test. The second row shows strain measurement from the strain gauge as the reference. The trend of capacitance variation (3rd row) to the strain amplitude change (2nd row) matches well. The third row shows the comparison of PCAP (off-the-shelf wired) capacitance measurement with the sensor board measurement. There was a little more noise from the PCAP, but in general, both (PCAP and the sensor board) show similar performance for the step load tests. Appendix C includes test result for the other six boards.

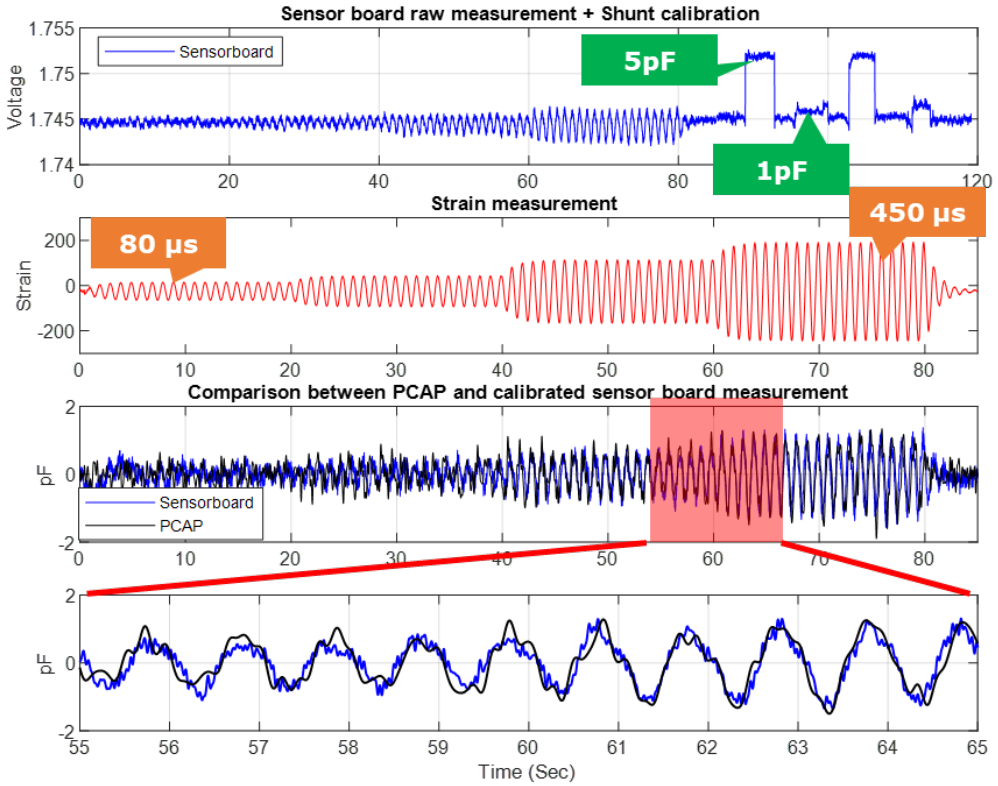

Figure 5.21: Example Test Results from the Sensor Board #1

5.5.4 Incremental Dynamic Step-Load and Shunt Calibration Test for Small SEC Setup

1-Hz sine wave with incremental step load was provided to the shear building via shake table APS400. Each step load sinewave was applied for 20 seconds and the amplitude was increased by 80 / 150 / 270 / 560 µ-strain. After the step load test, the shunt calibration test was

conducted to convert measured voltage from sensor board into absolute capacitance value. Double-step shunt calibration process with 5 pF and 1 pF capacitors was employed. A resistive-type strain gauge was installed to provide reference measurements (Figure 5.22), and the measurements by the sensor board and the PCAP were compared each other.

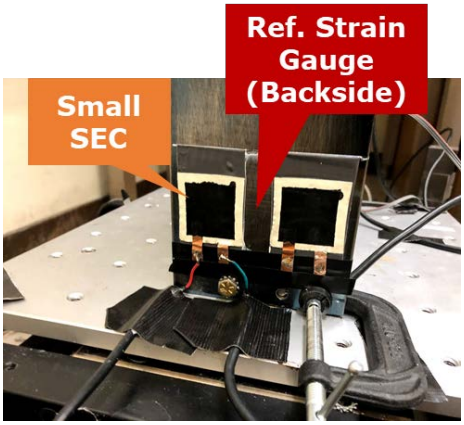

Figure 5.22: Specimen Setup

Figure 5.23 shows the example test result of the sensor board #8. The plot on the first row shows raw measurements during the shunt calibration test. The second row shows strain measurement from the strain gauge as the reference. The trend of capacitance variation (3rd row) to the strain amplitude change (2nd row) matches well. However, the reason for the signal shape difference was from the geometric size difference of sensors between strain gauge and SEC. The third row shows the comparison of PCAP (off-the-shelf wired) capacitance measurement with the sensor board measurement, which was converted from voltage measurement to capacitance by using the calibration factor achieved from the shunt calibration test. A little more noise is observed from the PCAP, but in general, both PCAP and the sensor board show similar performance for the step load tests. Appendix C includes the rest of the sensor board (#9 to # 17) test results.

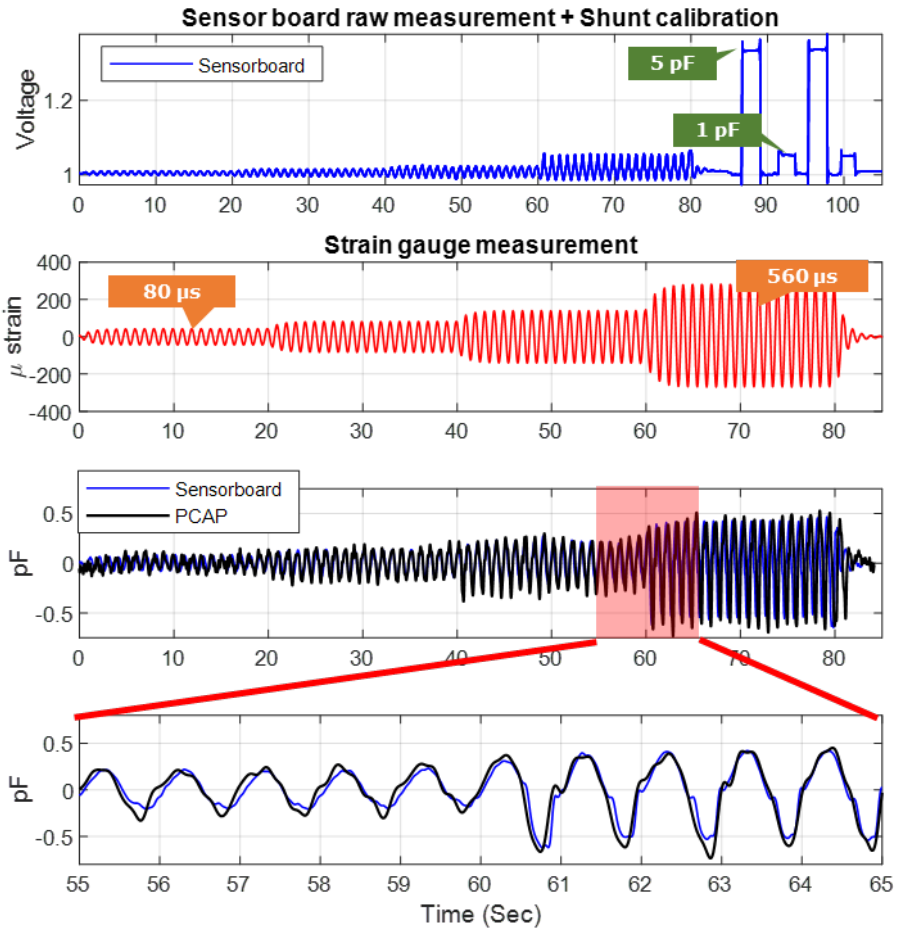

Figure 5.23: Example Test Results from The Sensor Board #8

5.6 Xnode Breakout Box Setup and Wheatstone Bridge for Strain Gauge

Field deployment requires multiple sensor readings from not only the SECs, but also the reference foil strain gauge using the Xnode. The breakout box is an additional component to interface up to five analog sensor channels with a single Xnode. However, the current breakout box was not able to supply consistent power voltage as 3.3 V which affects measurement consistency; thus, it was calibrated for accurate measurement and modified to be able to supply consistent voltage to the sensor board and Wheatstone bridge circuit.

5.6.1 Xnode Breakout Box Setup

The breakout box is designed as an interface for the Xnode to measure multiple (up to five) external sensor channels. Each channel provides both single-ended and differential

measurement modes. Figure 5.24(b) shows an Xnode with a breakout box connected with a 20-pin cable. The current breakout box design did not offer consistent 3.3 V voltage supply through the existing power channel. Simple re-wiring as shown in Figure 5.24(a) was done to provide consistent 3.3 V power supply as shown in Figure 5.24(c).

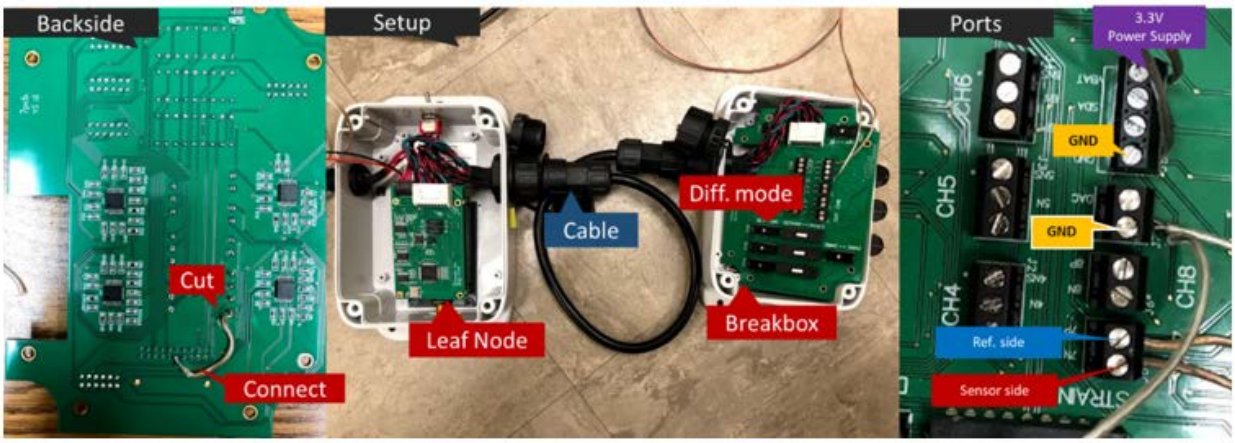

(a) Wiring modification (b) Xnode+breakout box setup (c) Breakout box wiring

Figure 5.24: Breakout Box Setup

Each breakout box needs to be calibrated prior to use in the field because the internal circuit in the breakout box affects signal magnitude. Therefore, calibration tests were conducted using the sine wave excitation test with the shear building to compare the Xnode measurement with the reference measurement from NIDAQ. A calibration factor 1.335 was obtained for converting the breakout box measurement to the actual voltage level of the Xnode.

5.6.2 Three-Wire Wheatstone Bridge Configuration

For strain gauge measurement using Wheatstone bridge circuit, a three-wire configuration Wheatstone bridge was chosen due to its advantages for robustness against temperature variation and the lead-wire induced errors. To be used with 120-ohm foil-type strain gauges, three 120 ohm resistors were assembled as shown in Figure 5.25. Figure 5.25 shows the Wheatstone bridge circuit, assembly, and schematic.

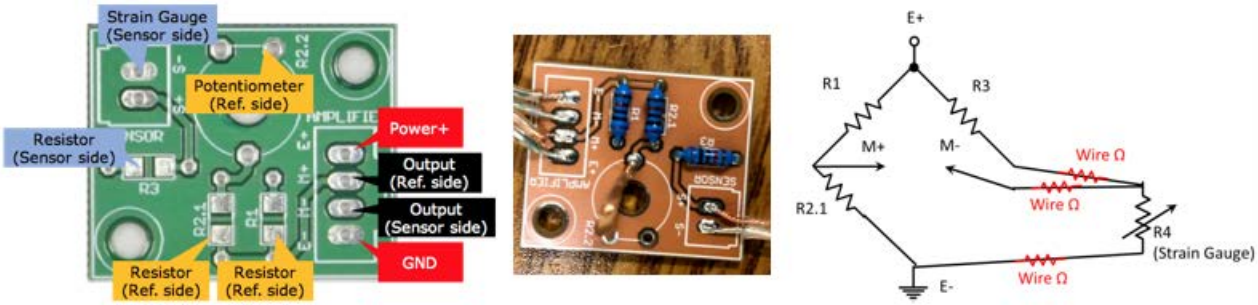

Figure 5.25: Wheatstone Bridge Setup for Strain Measurement

5.6.3 Test Result

Figure 5.26 shows the test result comparing the Xnode measurement with the Wheatstone bridge and the NIDAQ measurement as a reference. The upper plot shows NIDAQ measurement from the sensor side and the reference side of the Wheatstone bridge. These two signals were manually differentiated for the pure sensor signal variation, which was then compared with the Xnode measurement as shown in the lower plot. Excellent agreement was achieved as shown in the figure.

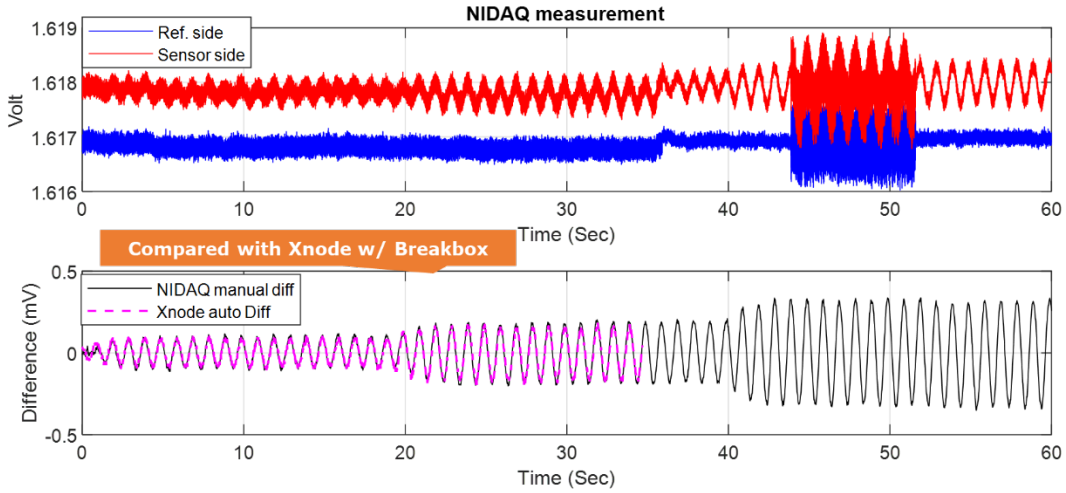

Figure 5.26: Comparison of Xnode + Wheatstone Bridge Measurement with NIDAQ Measurement

5.7 Conclusions

In this chapter, a capacitance-based wireless strain sensor board was developed for achieving wireless capacitance sensing with the SECs to facilitate long-term autonomous crack monitoring. The performance of the sensor board was evaluated through a series of lab tests. The sensor board was designed to interface with the Xnode wireless sensor platform to take advantage of many unique features of the Xnode aimed at realizing effective wireless structural health monitoring. By employing an AC Wheatstone bridge circuit, a high-precision bridge balancer, two-step signal amplification, and AM demodulation with low-pass filter, low-level dynamic capacitance variation of the SEC was successfully measured. This AC Wheatstone bridge-based configuration enabled analog voltage output that can be directly interfaced with the Xnode platform. Such a configuration is characterized by its simple PCB structure for low-cost and high-sensitivity capacitance-based strain measurement for civil infrastructure monitoring. A series of lab-scale tests revealed that the sensor board was able to perform low-noise and high-accuracy strain measurement. It outperformed the off-the-shelf wired capacitance measurement system (PCAP02) and achieved comparable performance as conventional strain sensing system using traditional foil strain gauges.

For field deployment, 20 sensor boards were assembled and tested for hardware quality validation. Seven sensor boards for measuring large SECs and 10 sensor boards for measuring small SECs were configured and tested with dynamic tests. All the sensor boards for small and large SECs showed satisfactory performance compared with the off-the-shelf capacitance measurement kit PCAP02 and conventional strain measurements.

The Xnode breakout box was modified for multi-channel measurement in the field. The Wheatstone bridge circuit was modified to the three-wire configuration for environmental resistance and the breakout box was modified for stable 3.3 V power feeding and was calibrated. A validation test was conducted for strain gauge measurement using the modified Wheatstone bridge, and showed good match with the NIDAQ measurement.

Chapter 6: Field Validation of Wireless Elastomeric Skin Sensors

6.1 Overview

In order to validate the integrated wireless fatigue crack monitoring system, in this chapter, a field deployment was conducted on a steel highway bridge that is subject to fatigue damage. Several wireless elastomeric skin sensors were deployed over fatigue-susceptible regions at the midspan of a steel girder. Particularly, two sizes of SECs including large SEC (3 in. × 3 in.) and small SEC (1.5 in. × 1.5 in.) were selected for the deployment. The newly developed wireless capacitive sensing boards were also deployed for measuring the capacitances of the SECs under traffic loads. Data was autonomously collected in the field through the wireless sensor network triggered by the passing traffic. Data processing results indicate the SEC measurements collected under passing vehicles are able to offer the basis for long-term monitoring of fatigue critical steel bridges.

6.2 Background of Xnode

The development of wireless smart sensor platforms has enabled many field applications of structural health monitoring for civil infrastructure. The attention to SHM has been increasing over the past decades due to major concerns about the safety of aging infrastructure. Continuously monitoring the integrity of structures in real-time can greatly improve the safety of structures and reduce the maintenance cost. A series of wireless smart sensor platforms have been developed in recent years with significant computational capabilities to facilitate structural condition assessment.

In wireless smart sensor networks, the sensor nodes communicate wirelessly, eliminating the need for cabling. In addition, each node has a microprocessor, making on-board digital signal processing, self-diagnosis, self-calibration, self-identification, and self-adaptation possible. Moreover, the sensor nodes can be deployed, moved, and replaced easily. In this study, the Xnode developed by the University of Illinois at Urbana Champaign (Fu, Mechitov, Hoskere, & Spencer, 2016; Fu, Hoang, et al., 2018; Spencer et al., 2017) is selected as the wireless sensing platform for this deployment. Xnode is a next-generation smart sensor platform for civil

engineering applications which enables high precision, inexpensive, and flexible instrumentation for SHM applications.

6.2.1 Hardware

The Xnode consists of three boards including a processor board, a radio/power board, and a sensor board. The processor board features an LPC4357 microcontroller from NXP Semiconductors, which can be used to perform on-board computation and data acquisition. The memory available on the mini 4357 is 32 MB for temporary data storage and processing. An SD card can be plugged into the radio/power board to increase the data storage size. The radio/power board has a power management circuit that controls charging from the battery and solar panels. It also includes a 2.4-GHz radio transceiver for low-power wireless communication which can reach up to 1 km line-of-sight with transfer rates up to 250 kbps.

The sensor board consists of a 24-bit high precision, analog-to-digital converter with eight differential channels of analog input, and antialiasing filters. It is capable of measuring (1) accelerations in three directions for global response monitoring, and (2) generic voltage signals from external sensors, required for advanced SHM applications. Among the eight sensing channels of the Xnode, the 3-axis accelerometer takes three channels, leaving five channels available for external sensors. The three boards are stacked together to complete the sensor node as shown in Figure 6.1. An IP67 environmentally hardened enclosure is used to package the sensor node as shown in Figure 6.2.

Figure 6.1: Xnode Processor, Radio/Power, and Sensor Boards
Source: Spencer et al. (2017)

Figure 6.2: Xnode Environmentally Hardened Enclosure
Source: Spencer et al. (2017)

6.2.2 Software

The Xnode is powered by FreeRTOS, an open source real-time operating system (RTOS). FreeRTOS is selected for the Xnode platform because of its open source nature, C-language implementation, availability of free support options, and a large user community. FreeRTOS provides a priority-based scheduler as well as inter-task communication and coordination tools. With this operating system, long-running and low-priority functions cannot block important tasks such as sensor sampling and radio communication. The Xnode platform is designed to be more standardized to make the development and interoperation with other software and hardware platforms easier.

Xnode provides several capabilities for application developers compared to previous platforms. For example, it extends the ability of SHM systems to capture extreme events, known as rare event detection. Due to the fact that uncertain delays in the start of sensing can be possibly avoided in RTOS-based systems, real-time triggering of the wireless sensor network is feasible to capture earthquakes and impact events, as durations of such events can be rather short. Secondly, the software toolsuite of Xnode provides a more engineer-friendly development environment to enable flexible implementation of SHM applications by civil engineers, most of whom do not necessarily have an extensive background of computer science knowledge or programming skills.

6.2.3 Event-Triggered Sensing

Wireless sensor networks help to reduce the cost of long-term SHM of civil infrastructure; however, performing wireless monitoring has its own challenges due to the inherent constraints.

Wireless smart sensors are typically powered with batteries with a finite power supply. To this end, duty cycling is therefore commonly adopted to save power. As a result, it is possible that important events could be missed if the sensors are in the sleep mode during the occurrence of the event. To address this issue, a demand-based sensing strategy has been developed with the Xnode (Fu, Zhu, Hoang, Mechitov, & Spencer, 2018). Specifically, a low-power trigger accelerometer (ADXL362) is integrated to the Xnode, which has very a low power consumption and hence is able to run continuously to monitor the ambient vibration level. ADXL362 is able to sample at frequencies up to 400 Hz with a resolution of 12 bit. Moreover, it can store up to 512 samples using an integrated buffer, which correspond to 1.7 seconds of data if sampled at 100 Hz. The ability to store data using the integrated buffer and at the same time trigger the main sensor board for data collection enables robust rare event detection and sensing.

The designed prototype for event-triggered sensing provides three basic functionalities including:

1. Communications of commands and data between Xnode and ADXL362;
2. Ability to wake up Xnode from its deep sleep mode; and
3. Initiation of high-fidelity sensing with Xnode.

Figure 6.3 shows the schematic of the prototype to configure ADXL362 with Xnode. The INT1 pin from ADXL362 is connected to the RESET pin from Xnode. This connection plays the main role in the triggering mechanism. INT1 from ADXL362 is triggered whenever the detected acceleration level exceeds a predefined threshold. Then, the RESET pin from Xnode receives the signal from INT1. Subsequently, Xnode wakes up from its deep sleep mode and starts taking measurements. This mechanism allows the Xnode to spend most of the time in deep sleep mode in order to save power. To address the challenge of response latency, the INT2 pin from ADXL362 is connected to the GPIO pin of Xnode. At the moment when an important event is detected by ADXL362, INT2 will interrupt any ongoing task to enable Xnode for data collection.

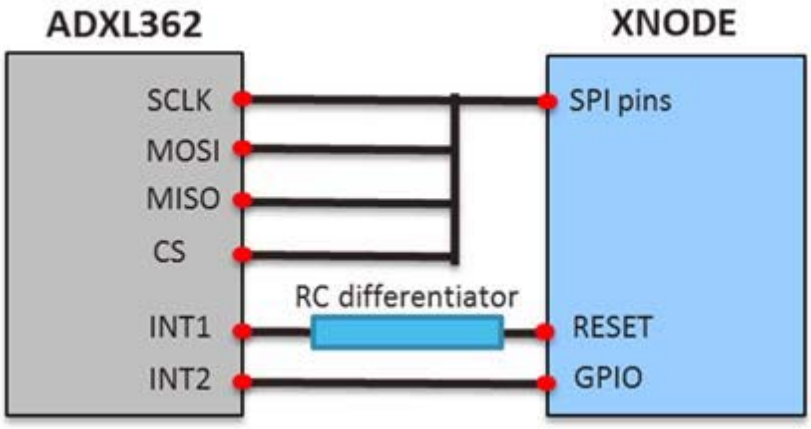

Figure 6.3: Configuration of ADXL362 with Xnode
Source: Fu et al. (2018)

An effective software is also required to manage ADXL362 and Xnode and enable event-triggered sensing. Figure 6.4 presents the flowchart of demand-based wireless smart sensor for event-triggered sensing. When Xnode is initiated, it will send commands to ADXL362 and go to the deep sleep mode. Then, ADXL362 will start taking measurements continuously in an ultra-low-power mode. If an important event happens, i.e., the acceleration measured by ADXL362 exceeds the predefined acceleration threshold, it will trigger and wake up the Xnode. Xnode then starts collecting data based on the predefined sampling parameters. At the same time, ADXL362 saves 512 acceleration samples into its buffer and waits for Xnode to retrieve the data. At the end, Xnode reads the collected data by ADXL362 and integrates that with the measured data by Xnode. Finally, Xnode will save the data on its SD card.

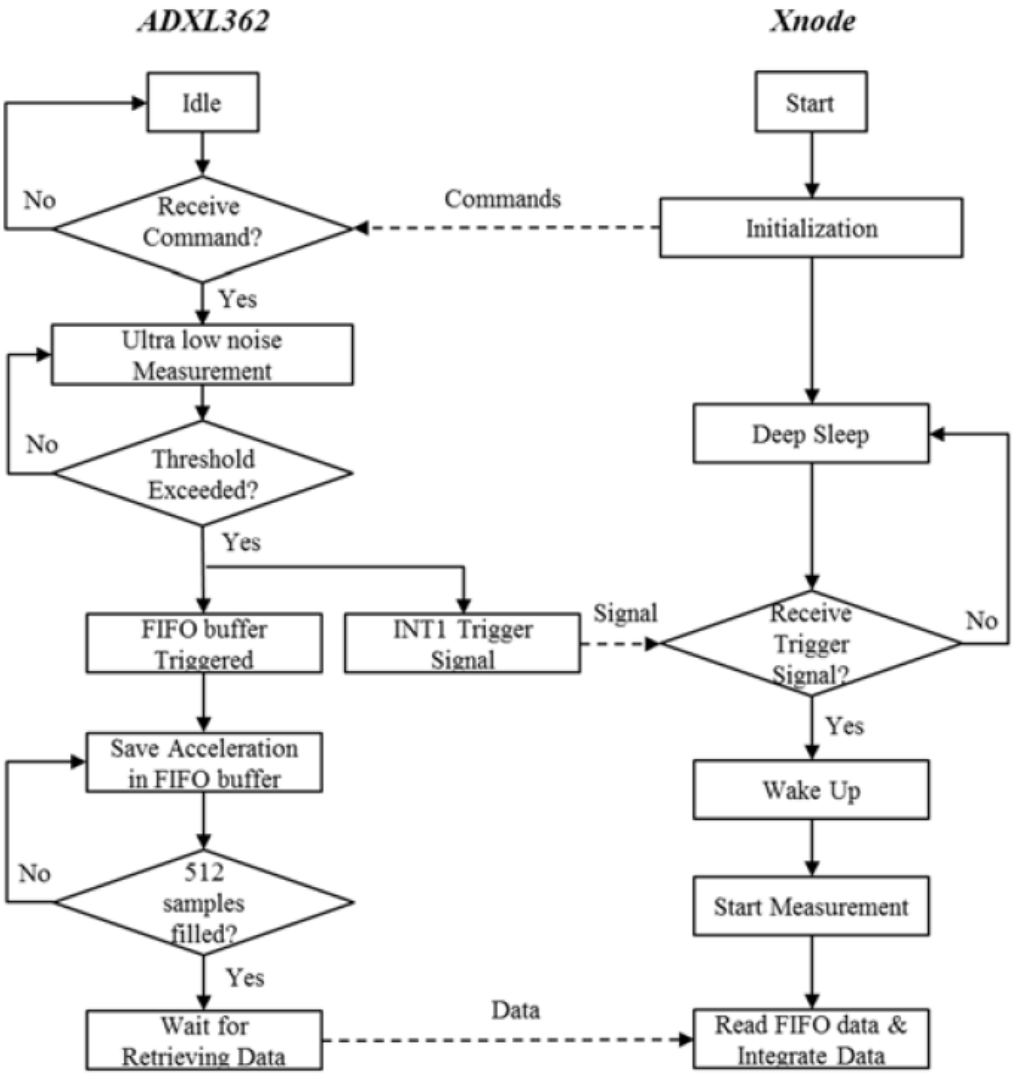

Figure 6.4: Event-Triggered Sensing Flowchart
Source: Fu et al. (2018)

6.2.4 Application at the University of Kansas

We installed the gateway node software on one of the Xnodes and installed the leaf node software on two other Xnodes. A terminal emulator, Tera Term, is installed on the PC serving as the base station of the sensor network that sends commands and reads data from the Xnodes. After connecting the Gateway node to the PC and launching Tera Term, there will be instructions displayed on Tera Term as shown in Figure 6.5.

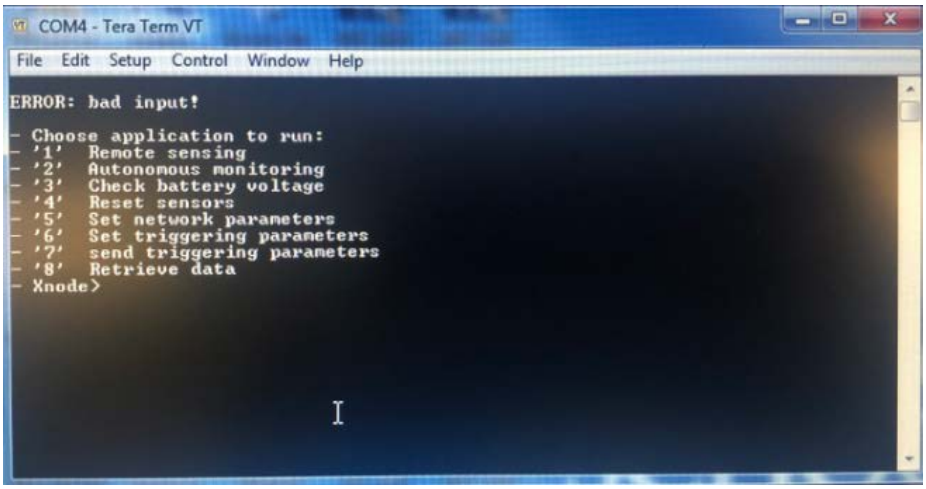

Figure 6.5: Available Functions of Xnode

As shown in Figure 6.5, there are several options for using the Xnode. REMOTE SENSING (the 1st option) is a fundamental data acquisition application which is implemented in FreeRTOS as a demonstration of the RTOS-based framework. This application is used to help the coordination between the gateway node and multiple leaf nodes. During the REMOTE SENSING application, sensor nodes start sensing (taking measurements) when they receive commands from a gateway node. Once the sensing is finished, leaf nodes send sensor data back to the gateway node. AUTONOMOUS MONITORING is the 2nd option in which the network wakes up based on a predefined time interval and performs REMOTE SENSING. For example, if the predefined time interval is set as 12 hours, the network collects data twice a day.

The TRIGGERING SENSING application takes care of collecting data from the bridge for long-term monitoring. Our goal is to wake up each leaf node when it is informed that a vehicle event is happening. These types of events are called triggering events. Sensing is triggered when the vibration level due to the vehicles exceeds the predefined vibration threshold of the leaf node. For this purpose, an additional low-power accelerometer (ADXL362) is connected to each Xnode to wake up the node. In the final version of Xnodes, ADXL362 is integrated in the radio board, and the required changes were made to the software. For TRIGGERING SENSING, the sensing parameters will be sent to the leaf nodes by the 7th option shown in Figure 6.5. After that, the leaf nodes will start collecting data independently.

Eventually, the 8th option can be used to retrieve the measured data from the leaf nodes to the gateway node.

The final version of the software makes it possible to modify all the sensing parameters remotely by using the 5th and 6th options. Option 5 is for modifying the sensing parameters for REMOTE SENSING, while option 6 allows one to modify the sensing parameters for TRIGGERING SENSING. The sensing parameters include SAMPLING TIME, SAMPLING FREQUENCY, NUMBER OF CHANNELS, and THRESHOLD ACT. The first three parameters are in common for REMOTE SENSING and TRIGGERING SENSING. However, the last one determines the vibration threshold to wake up the nodes and perform TRIGGERING SENSING.

We have tested the triggering functionality of the Xnodes together with the software. In our field visit on 07/02/2018, we investigated the vibration level coming from the vehicles passing the bridge by collecting acceleration measurements. Figure 6.6 presents one example of measured acceleration in vertical direction from the girder. It can be seen that the peak acceleration response of the bridge typically ranges from a small value to about 100 mg.

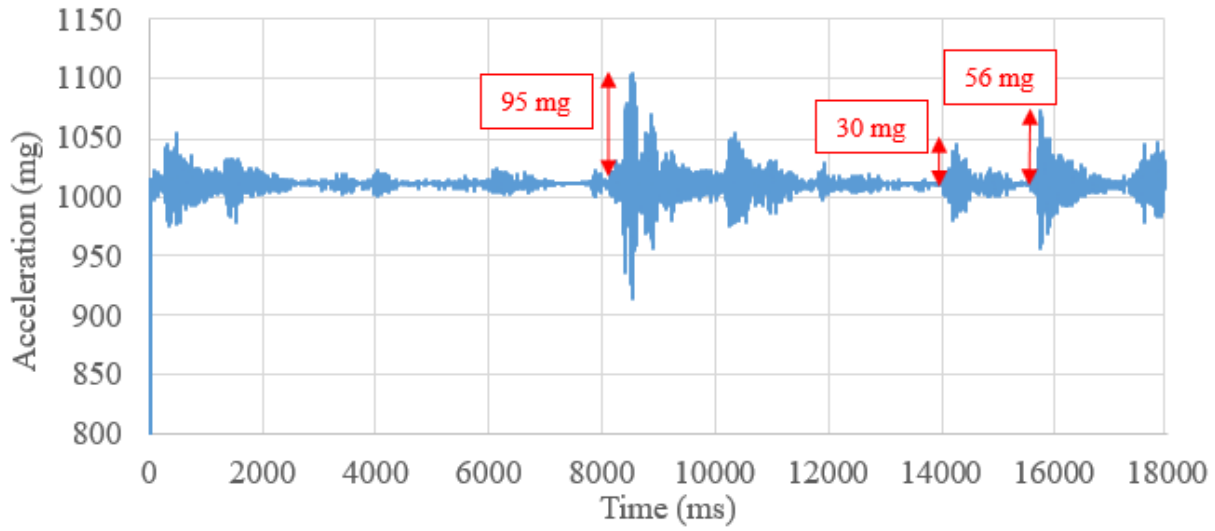

Figure 6.6: Bridge Girder Acceleration Measurement in the Vertical Direction

Based on the measured acceleration time histories, we tried several different vibration thresholds for the sensors for triggering sensing. Our goal was to achieve a certain number of

times the nodes will be woken up during the day and collect data. The first threshold was set equal to 50 mg, which turned out very low because with this threshold the nodes were almost constantly taking measurements. After several trials and errors, 100 mg was chosen as the vibration threshold for triggering sensing. The final triggering sensing parameters for the field deployment are:

SAMPLING TIME = 60 seconds

SAMPLING FREQUENCY = 100 Hz

NUMBER OF CHANNELS = 8

THRESHOLD ACT = 100 mg

6.3 Background of the Capacitance Sensor Board

6.3.1 Balancing and Shunt Calibration

As introduced in Chapter 5, the capacitance sensor board is designed by our Arizona team to measure the capacitance of SEC sensor by converting the capacitance change to voltage change. Balancing and shunt Calibration are the two main steps prior to data collection for the SECs. In particular, balancing is achieved by adjusting the potentiometers on the capacitance sensor board to match the signals of different jumpers monitored by an oscilloscope. To perform shunt calibration for the coefficient to convert the measured voltage to capacitance, two switches on the sensor board corresponding to two capacitors are turned on and off in sequence. As a result, two jumps can be observed in the measured voltage. The difference between those two jumps corresponds to a 4-pF change in capacitance. By having the change in voltage induced by the 4-pF change in capacitance, the calibration coefficient can be calculated. Figure 6.7 presents the setup for balancing and shunt calibration that includes the sensor board, SEC sensor, and Xnode. The SEC sensor is attached to a steel plate. Figure 6.8 shows the monitored signal at different stages of the balancing process. An example of calculation for shunt calibration is presented in Figure 6.9.

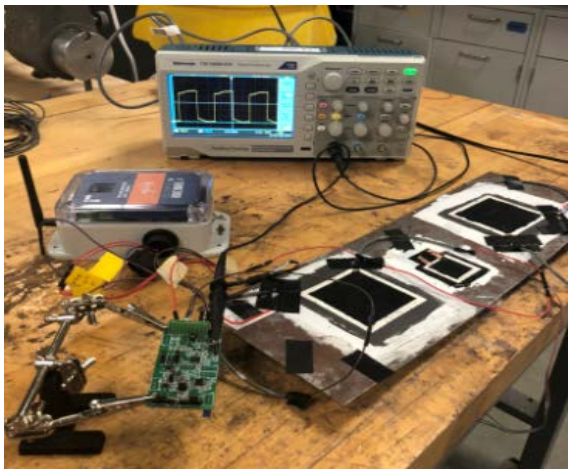

Figure 6.7: Capacitance Sensor Board Setup for Balancing and Shunt Calibration

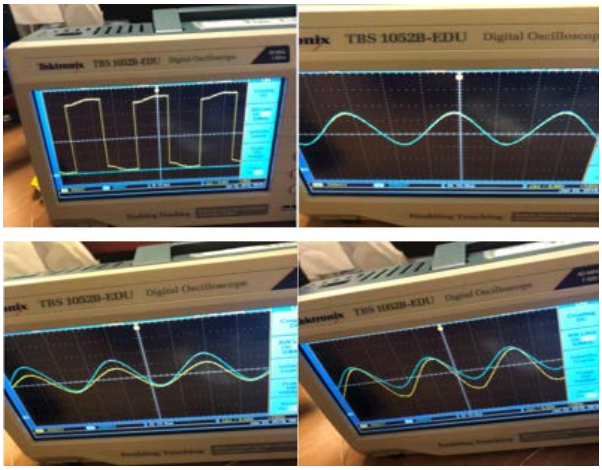

Figure 6.8: Different Stages of the Balancing Process

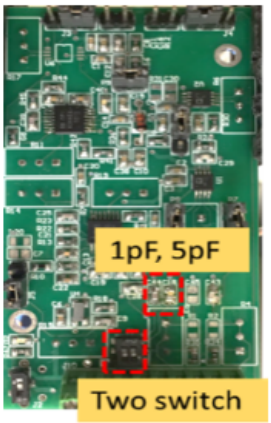

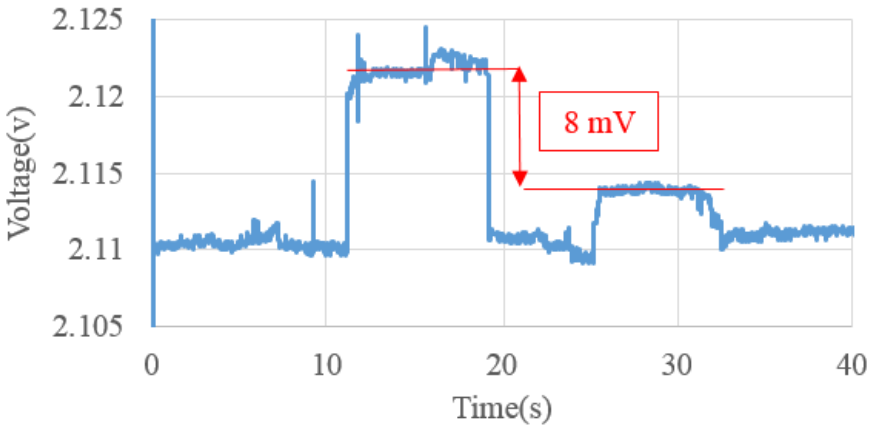

ΔVoltage (mV)	Δcapacitance (pF)	Shunt coefficient
8	4	2

Figure 6.9: Shunt Calibration

6.3.2 Pre-Balancing and Shunt Calibration Before Deployment

The balancing and shunt calibration process described above needs to be performed separately for each individual SEC sensor since each SEC sensor has a slightly different nominal capacitance. The process involves manual tuning of the potentiometers and switching the calibration capacitors on and off. In addition, an oscilloscope is needed to visualize the signals throughout the process. In our previous field visits where a bucket truck was used to reach the target location on the bridge girder, it was found that performing the above balancing and shunt calibration work was challenging due to space limitation and movement of the bucket. To ensure reliable balancing and accurate shunt calibration, a strategy is created to pre-balance and shunt calibrate the sensor boards in the lab prior to the field deployment.

The proposed strategy starts with measuring the nominal capacitance of each SEC sensor on the bridge, which also includes the capacitance of the attached cables. In the lab, another SEC sensor is then used to replicate the nominal capacitance of the one on the bridge. Since the SEC sensors have very close capacitance, accurate matching could be achieved by adjusting the length of the cable. This method also allows accommodation of all SECs on the bridge by repeating the adjustment of the cable length. Once a replicate setup with the SEC in the lab is ready, the capacitance sensor board can be balanced and shunt calibrated accordingly, which can then be used with the SEC sensor on the bridge without further adjustments.

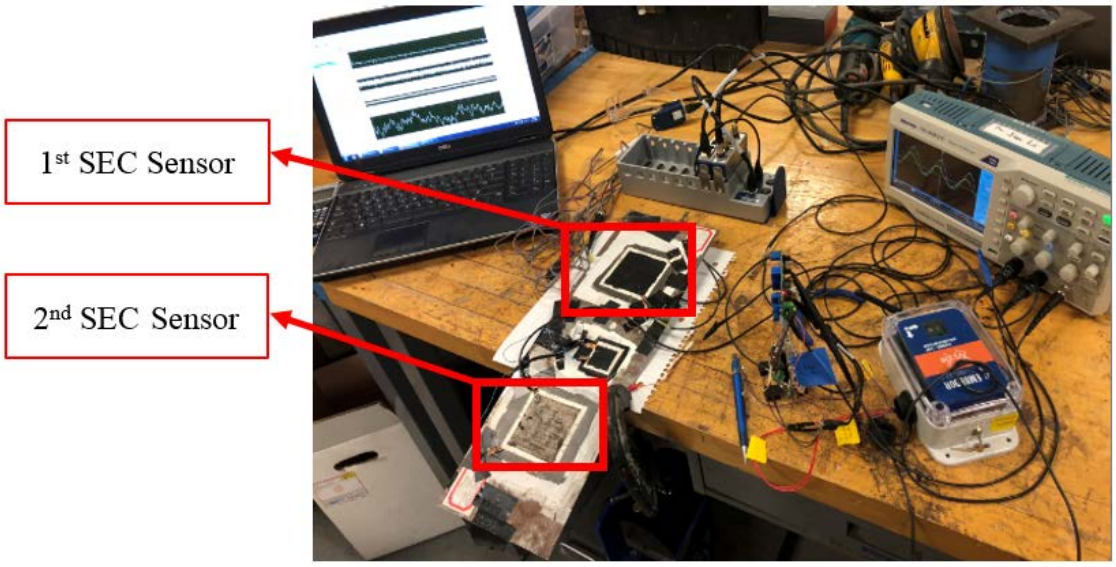

Figure 6.10: Setup for Pre-Balancing Tests Based on Same Nominal Capacitance

To validate this strategy, two SEC sensors with the same nominal capacitance were used as shown in Figure 6.10. A sensor board was balanced for the 1st SEC sensor and was then applied to the 2nd one. Figure 6.11 presents two important stages of balancing for those two SEC sensors. It can be seen from the figure that the exact same signals are observed in the oscilloscope for both SEC sensors, which indicates the sensor board balanced using the 1st SEC was also balanced for the 2nd SEC. We also calculated shunt calibration coefficients for these two SEC sensors as shown in Figure 6.12. The two coefficients are very close, proving that the calculated calibration coefficient for one SEC sensor can also be used for another one with the same nominal capacitance.

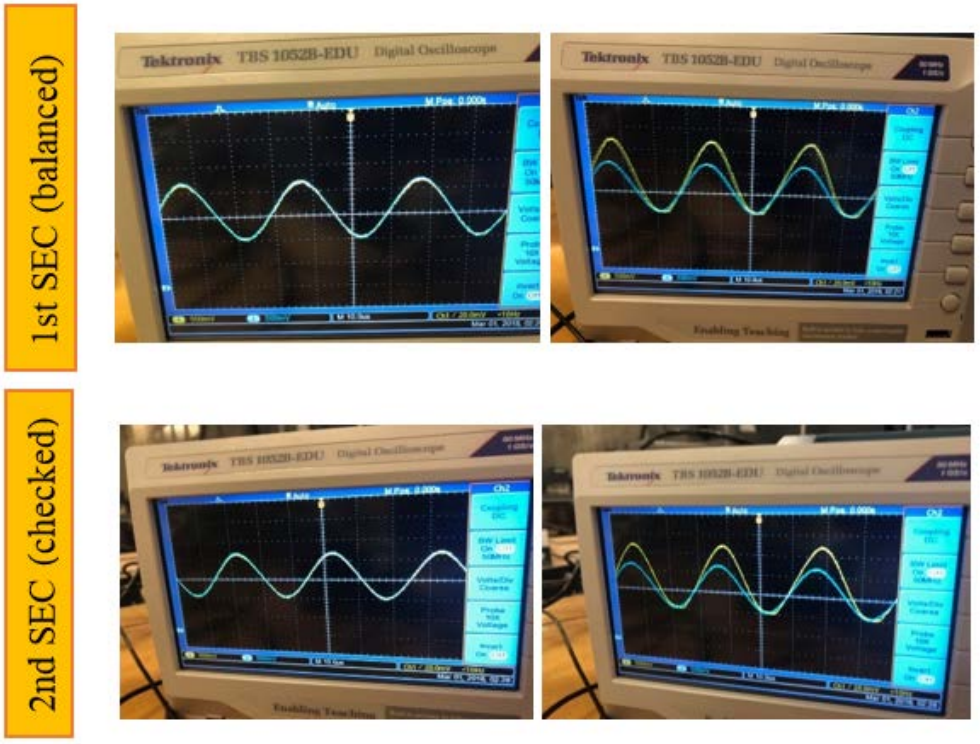

Figure 6.11: Important Stages of Balancing for Two SEC Sensors with the Same Nominal Capacitance

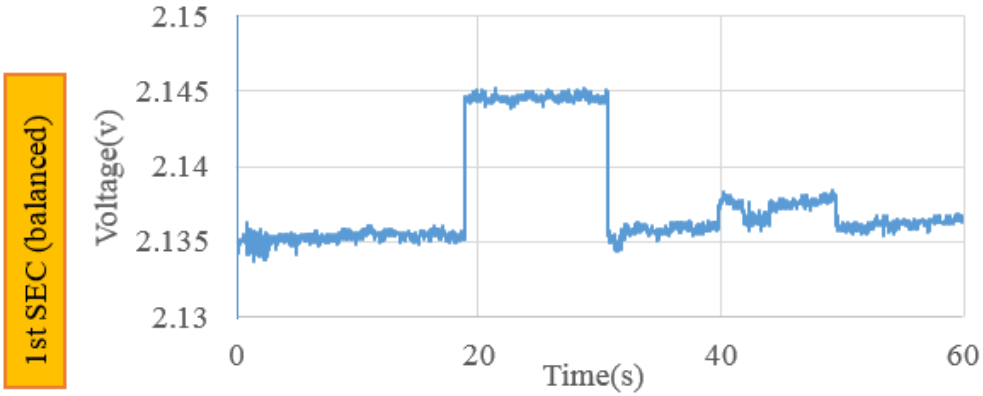

ΔVoltage (mV)	Δcapacitance (pF)	Shunt coefficient
7.32	4	1.83

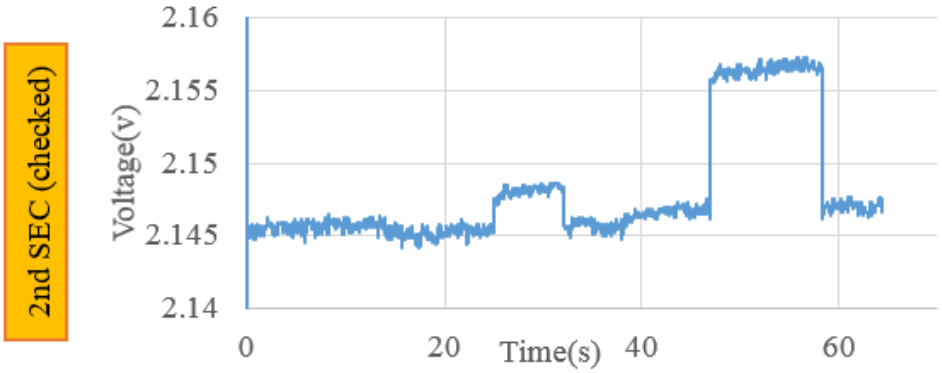

ΔVoltage (mV)	Δcapacitance (pF)	Shunt coefficient
7.25	4	1.81

Figure 6.12: Shunt Calibration Coefficient for the Two SEC Sensors with Pre-Balanced Board

6.4 Descriptions of the Field Deployment

6.4.1 Test Bridge

The test steel bridge was a part of the I-70 highway near Kansas City, Kansas, at the intersection of N. 57th Street, as illustrated in Figure 6.13(a). According to the inspection reports provided by the Kansas Department of Transportation (KDOT), the bridge was named 70-105-41731-127 (westbound) and 70-105-41732-128 (eastbound) and was originally designed in 1984 with some repairs in 2004. The bridge has eight spans with an overall length of 680 ft. Based on

the recent two inspections performed in 2013 and 2017, respectively, multiple locations on the bridge were subject to fatigue damage, typically at web-gap regions in the cross-frame-to-girder connections, as shown in Figure 6.13(b).

Figure 6.13(c) shows a typical web-gap region with existing fatigue cracks. Driven by the out-of-plane movement of the cross frame, a fatigue crack initiated at the top end of the weld between the connection plate and girder web. Depending on the structural layout, the fatigue crack could either grow along the weld toe or propagate into the girder web.

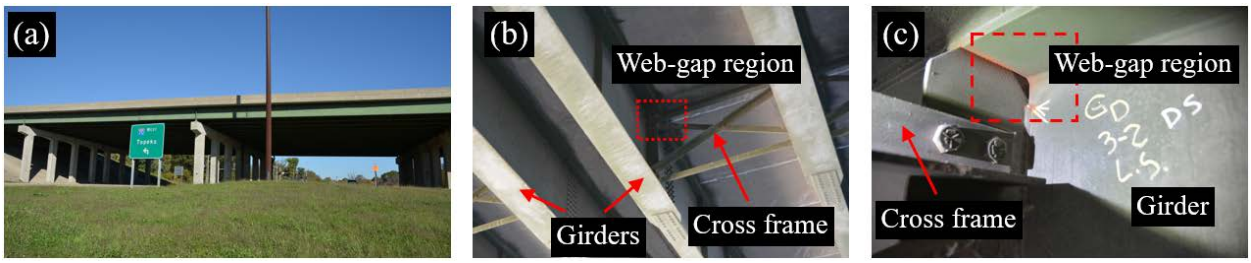

Figure 6.13: (a) Test Bed Bridge in the Field; (b) Typical Cross Frame and Longitudinal Girders; (c) Web-Gap Region Between the Cross Frame and the Girder

To facilitate the field deployment, a man-lift truck was used. The man-lift platform can easily access the fatigue-susceptible regions in the steel girders. A power generator was also used for offering electric power during the deployment. Figure 6.14 shows some photos taken during the field visits.

Figure 6.14: Field Deployment of the Monitoring System on a Steel Bridge

6.4.2 SEC Arrangement

An exterior girder was selected for the SEC installation, as shown in Figure 6.15(a). Two fatigue-susceptible regions were selected for the SECs. The first region is on the web gap region

on the exterior side of the girder (Figure 6.15(b)). This region was inspected in both 2013 and 2017. Based on the inspection reports and the marks on the structural surface, two fatigue cracks can be found in this region, including: (1) a horizontal crack initiated between the flange and the web (Crack 1); and (2) a horizontal crack in the web (Crack 2). As can be seen in Figure 6.15(c), both cracks propagated during the period between the past two inspections.

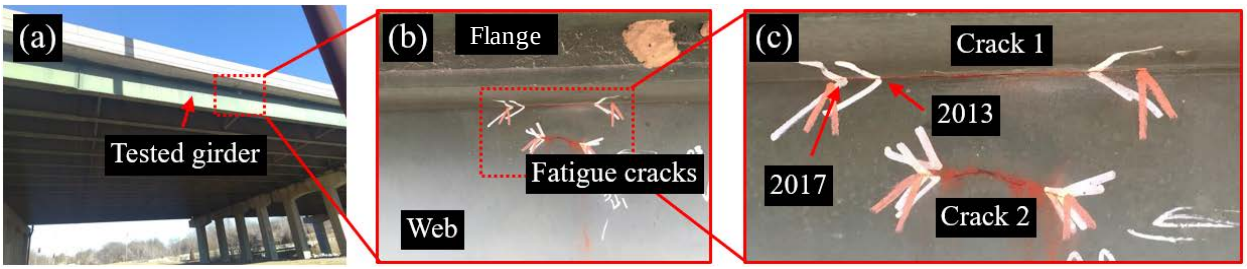

Figure 6.15: Detail Views about the Exterior Side of the Girder Prior to the Sensor Installation

(a) The Steel Girder for Sensor Deployment; (b) Two Fatigue Cracks at the Exterior Side of the Girder; (c) Arrows Indicate Crack Growths Between Inspection Periods

Figure 6.16(a) demonstrates the arrangement of the SECs where five small SECs with a size of 1.5 in. × 1.5 in. (38.1 mm × 38.1 mm) were deployed in this region. In particular, two SECs (a1 and a5) were installed to cover Crack 1 and three SECs (a2, a7, and a4) were attached to Crack 2. Additional short cables were attached to the SECs in order to connect them to the wireless capacitive board for data collection, as shown in Figure 6.16(b).

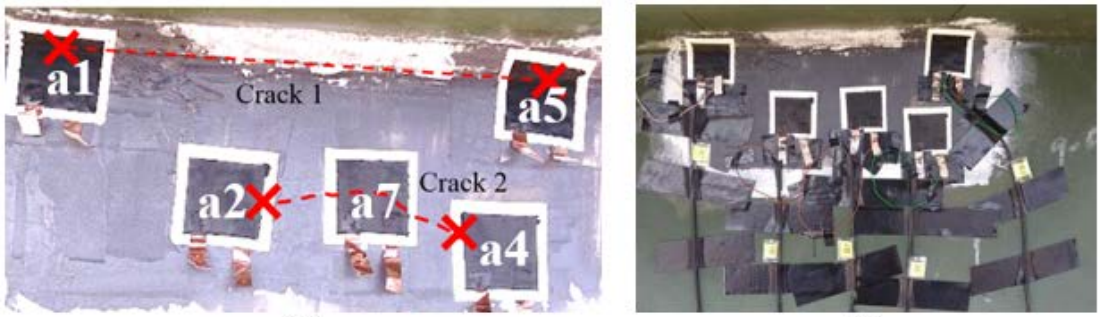

Figure 6.16: (a) Arrangement of the SEC Arrays; (b) SEC Arrays after Soldering the Cables

Figure 6.17(a) illustrates the SEC installation at the same web-gap region on the interior side of the girder. A fatigue crack (Crack 3) was observed on the connection plate between the

cross frame and the girder web. One large SEC was installed in this region, denoted as SEC b1 as shown in Figure 6.17(b).

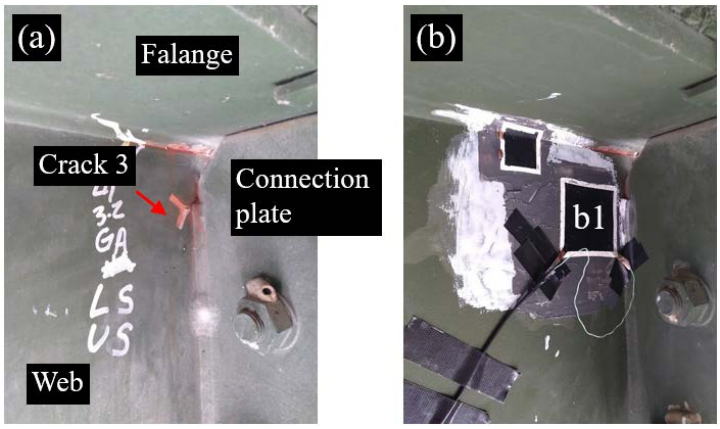

Figure 6.17: SEC Installation on the Interior Side of the Girder
(a) Selected Fatigue-Susceptible Region Prior to the Installation; (b) SEC Installation

6.4.3 Strain Gauge Installation

To normalize the capacitance measurement of the SEC, the level of loading due to the passing vehicles is needed. In this field deployment, we adopted strain measurements from the cross frame to indirectly infer the traffic load. Figure 6.18 shows the strain gauge installation for which the cross frame near the web-gap region was selected for the strain gauge deployment. The strain gauge was installed at the bottom chord of the cross frame, as shown in Figure 6.18(b).

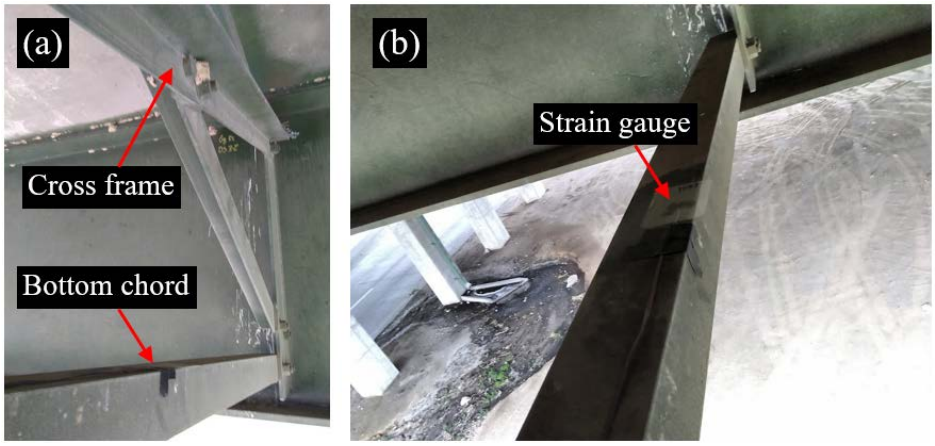

Figure 6.18: Strain Gauge Installation on the Cross Frame
(a) Cross Frame Prior to Sensor Installation; (b) Strain Gauge Installation

Some typical strain gauge measurements under the traffic loading are illustrated in Figure 6.19. A total of three datasets were collected during this field visit. The durations of these datasets were around 5 minutes, 5 minutes, and 1 minute, respectively. The black lines represent the raw signals while the red lines represent the signals after applying a low-pass filter. As can be seen in the figures, the pulse-like responses are provoked by the passing vehicles. These pulse-like responses can be clearly observed in the detailed views such as the second column in Figure 6.19. In addition, there are some high frequency oscillations in the measurements (shown in the last column of Figure 6.19). These high frequency oscillations may be attributed to the self-vibration of the cross frame where the strain gauge was installed.

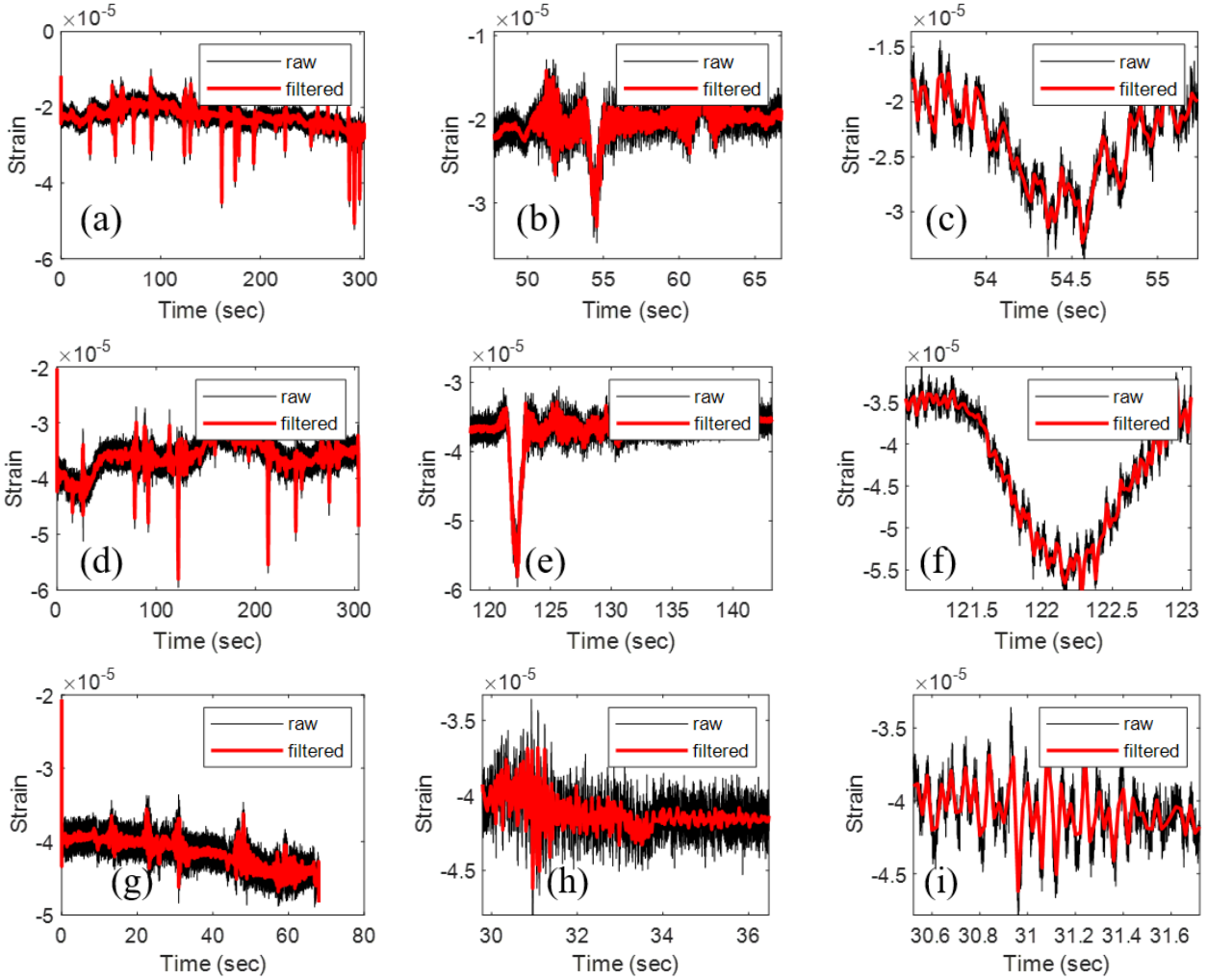

Figure 6.19: Typical Strain Gauge Measurements Under Traffic Loads

The three sample measurements are demonstrated as the first, second, and third rows. First column is the original data; second and third columns are close-up views. Black lines are raw signals and red lines are filtered signals.

6.4.4 Deployment of Wireless Capacitive Sensing Boards

The manufactured sensor boards were shipped from the Arizona team to the University of Kansas (KU). The sensor boards were all tested for quality assurance at KU as well. During a field visit, we measured the nominal capacitances of all SECs installed on the bridge mid-span. We used the measured nominal capacitances to pre-balance all the sensor boards and calculate their shunt calibration coefficients. Thus, in our final deployment, we would just need to connect the SECs to the sensor boards. Figure 6.20 presents the schematic of sensor deployment on the bridge for the exterior and interior sides of the girder together with their nominal capacitances. Table 6.1 shows the assigned pre-balanced sensor board to each SEC sensor and their corresponding shunt calibration coefficients obtained in the lab.

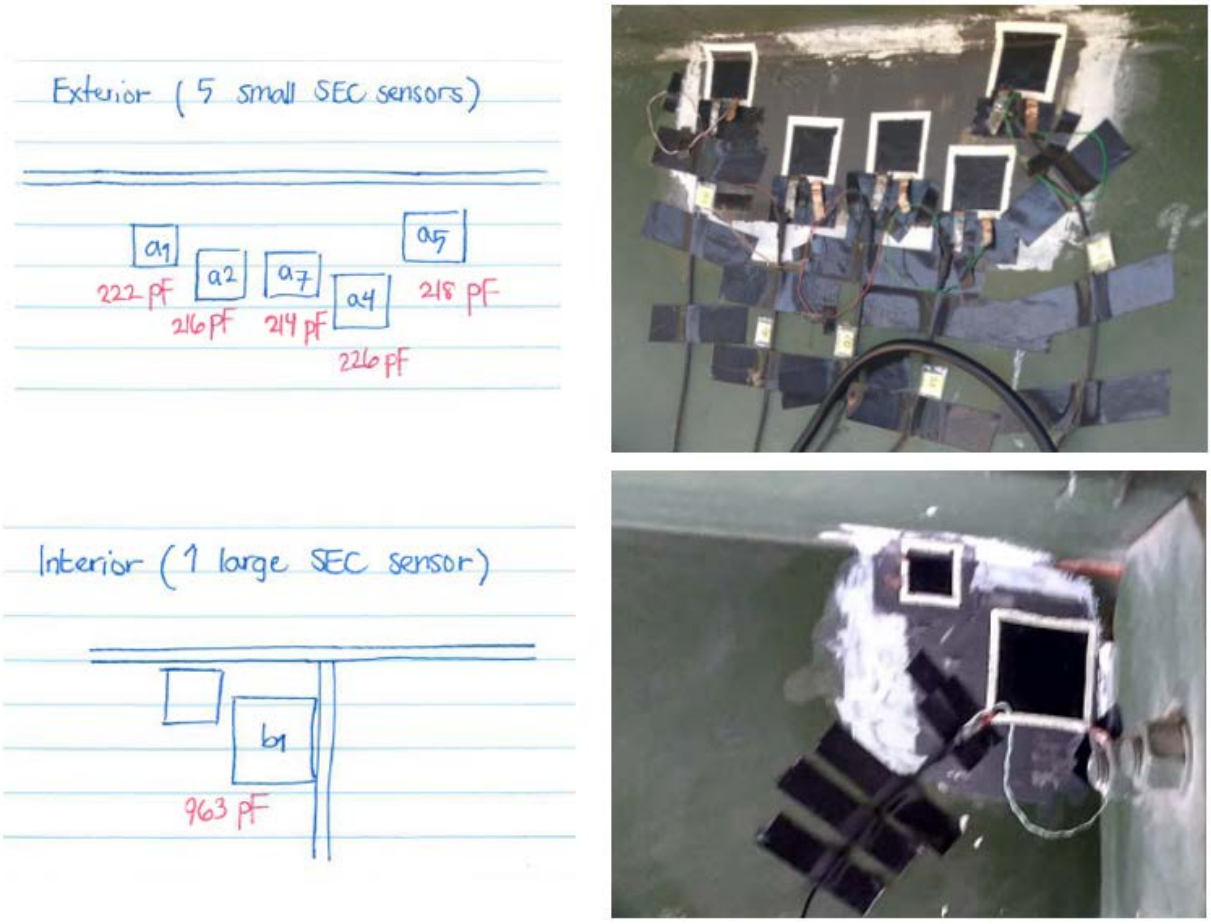

Figure 6.20: Schematic of Sensor Layout on the Bridge

Table 6.1: Connection Details for the Final Deployment on the Test Bridge

Girder face	SEC Sensor		Sensor board	Shunt calibration coefficient (V/pF)	Breakout box	Breakout box calibration	Xnode	Channel number
Exterior	Small SEC	a1	S4	0.005109	No. 2	7.6613	Node 5	4
		a2	S8	0.008775				5
		a5	S3	0.031253				8
		a7	S10	0.043672				6
	Strain	-	-	-				7
Interior	Large SEC	b1	L2	0.001211	No. 1	7.6725	Node 1	8
	Strain	-	-	-				7

The final task before the field deployment was to incorporate the breakout box to connect the Xnode's sensing channels to the sensor boards for wireless data collection. Figure 6.21 shows the interface board inside the breakout box. This board works as an interface between Xnode and sensor boards to allow integration of the sensor boards to the external channels of Xnode. The breakout box itself has a calibration coefficient for voltage measurements. To calculate the coefficient, we first took measurements from one SEC sensor using the Xnode through the breakout box and the NI-DAQ, respectively. We then matched these two measurements to compute the calibration coefficient. An example of measurements from both Xnode and NI-DAQ are shown in Figure 6.22 before and after applying the calibration coefficient. For this particular breakout box, the coefficient is equal to 7.66. It can be seen that after applying the coefficient, the measured signal from Xnode and the breakout box matches pretty well with the measurement from NI-DAQ. Note that the plotted signal after the calibration coefficient is a zoom-in version of the original signal.

Figure 6.21: Breakout Box

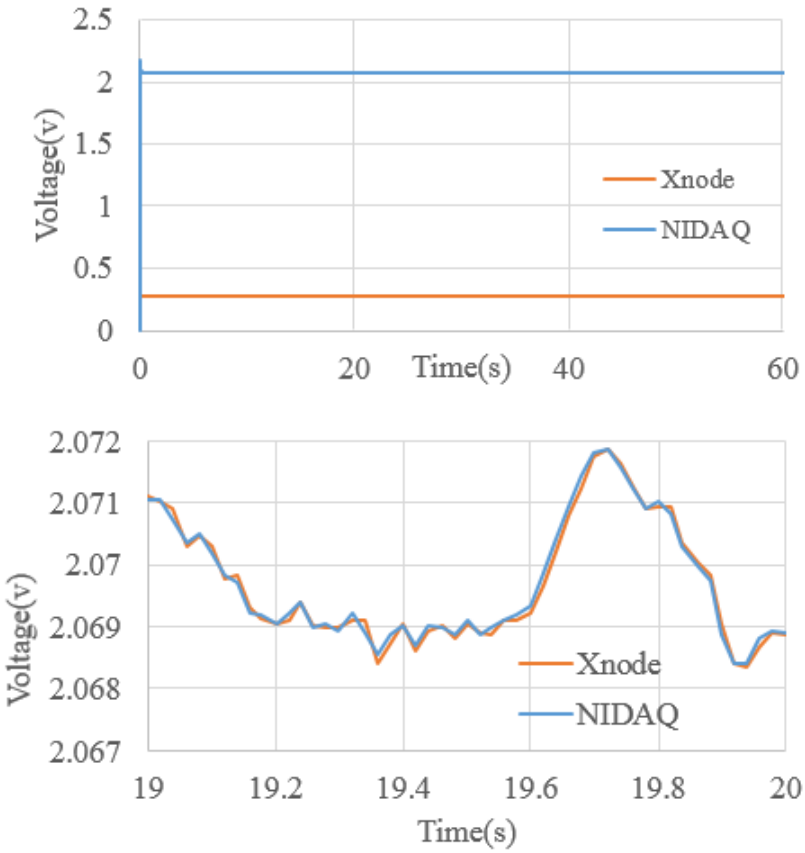

Figure 6.22: An Example of Calculation of the Breakout Box Calibration Coefficient

Figure 6.23 shows how we used the breakout box to make all the connections required between the Xnode and the sensor boards. The breakout box is connected to the Xnode through a cable, and the sensor boards are connected to the breakout box through a series of jumper wires.

In the field, we would just need to connect the SEC sensors to the sensor boards. The details of the connections between the sensor boards, breakout boxes, and Xnode channels for the final deployment are described in Table 6.1.

Figure 6.23: Connection of Sensor Boards to Xnode Through the Breakout Box

Figure 6.24 shows a picture of the final sensor deployment on the bridge. For this deployment on the facial side of the girder, voltage measurements are taken from four small SEC sensors and one strain gauge.

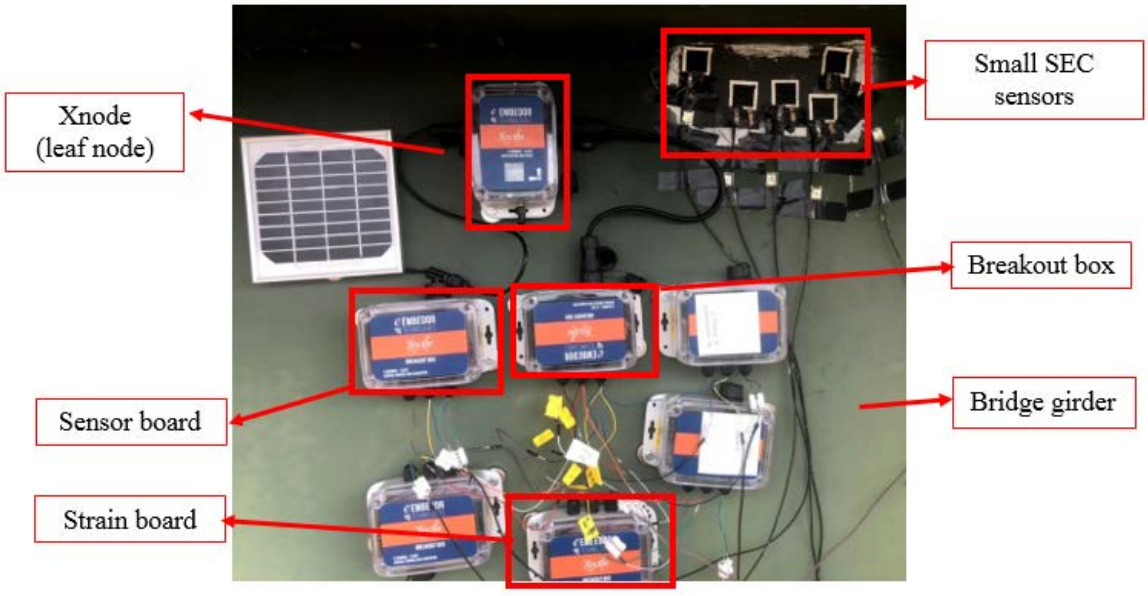

Figure 6.24: Sensor Layout of the Field Deployment on 07/16/2018 (Exterior Side of the Girder)

6.5 Analysis of Data Collected from the Field Deployment

6.5.1 Results from the Exterior Side of the Girder

Once the monitoring system was deployed on the steel bridge, autonomously triggered by the passing vehicles, measurements were collected from the Xnodes between July 16th and 17th, 2018. The datasets collected in the exterior side of the girder include: (1) measurements of strain gauge on the cross frame; (2) measurements of SEC a1, a2, a3, and a5 on the fatigue-susceptible region; and (3) the accelerometer installed on the exterior side of the girder. All measurements are synchronized with a duration of 1 minute.

Figure 6.25 shows a typical dataset from the exterior side of the girder while more measurements can be found in Appendix D.1. The acceleration measurement is demonstrated in Figure 6.25(a), where several peak responses induced by passing vehicles can be found in the 1-minute measurement. Similarly, the strain measurement also shows peaks at approximately the same locations. These results indicate that vehicle-induced bridge vibrational responses were successfully captured by both the accelerometer and strain gauge. Notice that strain measurement has low resolution (quantization error) compared with the acceleration measurement, which could be attributed to the lack of an amplification circuit in the strain sensor board.

Figure 6.25(b) to Figure 6.25(f) show the capacitance measurements of SECs. As can be seen in the figures, SEC a5 produces a very small response compared with other three SECs. On the other hand, SEC a1, a2, and a3 have larger responses but the signals contain two major components, including (1) high frequency peaks at approximate locations where acceleration and strain measurements have cyclic responses induced by the traffic loads; and (2) repetitive components throughout the entire time histories. The first component could be attributed to the traffic load, while the source of the second component is not definitely determined, but could be the environmental interference from the field, which is not relevant to the load-induced SEC responses.

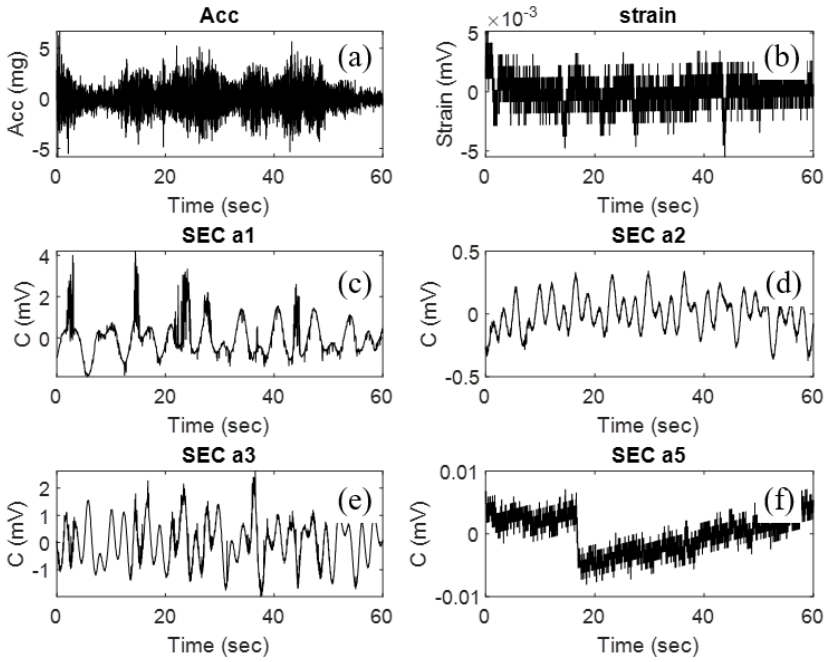

Figure 6.25: Typical Measurements from the Exterior Side of the Girder
(a) Acceleration; (b) Strain; (c) SEC a1; (d) SEC a2; (e) SEC a3; (f) SEC a5

To remove the noise content while keeping the high frequency responses, a curve fitting is first performed to fit the trend of the repetitive component. The fitted curve is shown as the red line and the original data of SEC a1 is illustrated as blue dots in Figure 6.26(a). Next, by subtracting the original data with fitted curve, the signal of SEC a1 can be extracted, as shown in Figure 6.26(b). The high frequency peaks are kept after the above procedure, while the repetitive noise content is significantly reduced.

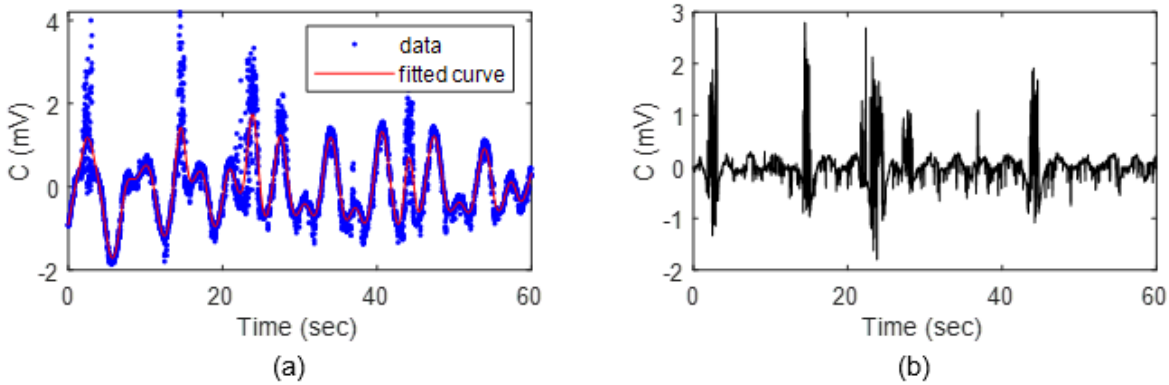

Figure 6.26: (a) Curve Fitting of SEC a1; (b) Signal of SEC a1 After Processing

Using this strategy, the capacitance measurement of SEC a2 can be processed and its signal processing procedure and result can be found in Figure 6.27(a) and Figure 6.27(b), respectively. The response of SEC a2 becomes small after processing. This is probably because the monitoring system did not capture high amplitude response caused by the passing vehicles. Figure 6.28 shows the processed data of SEC a3. The high frequency peaks can be preserved, as shown in Figure 6.28(b).

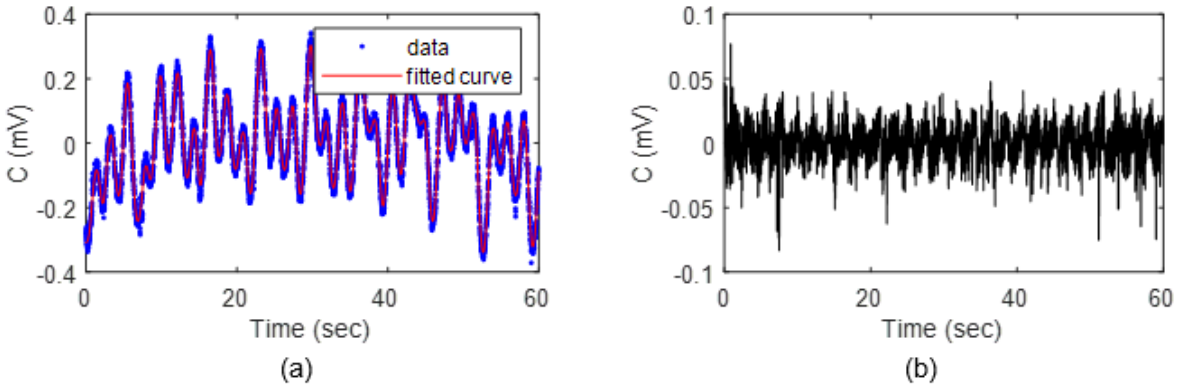

Figure 6.27: (a) Curve Fitting of SEC a2; (b) Signal of SEC a2 After Processing

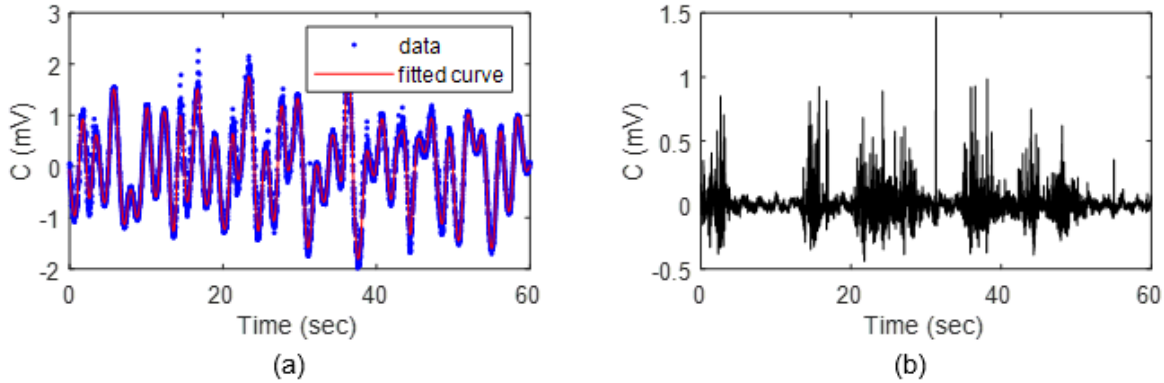

Figure 6.28: (a) Curve Fitting of SEC a3; (b) Signal of SEC a3 After Processing

6.5.2 Results from the Interior Side of the Girder

The datasets collected from the interior side of the girder include: (1) measurements from the strain gauge on the cross frame; (2) measurements from a large SEC at the fatigue-susceptible region; and (3) accelerations from the accelerometer installed on the interior side of the girder. All measurements are synchronized with total duration of 1 minute.

Figure 6.29 shows a typical result from interior side of the girder while more measurements can be found in Appendix D.2. Several vehicle-induced responses can be found in the acceleration measurement, as shown in Figure 6.29. Similarly, the strain and SEC signals also demonstrate responses with higher amplitudes. Low frequency drifts can be found in the SEC and strain measurements.

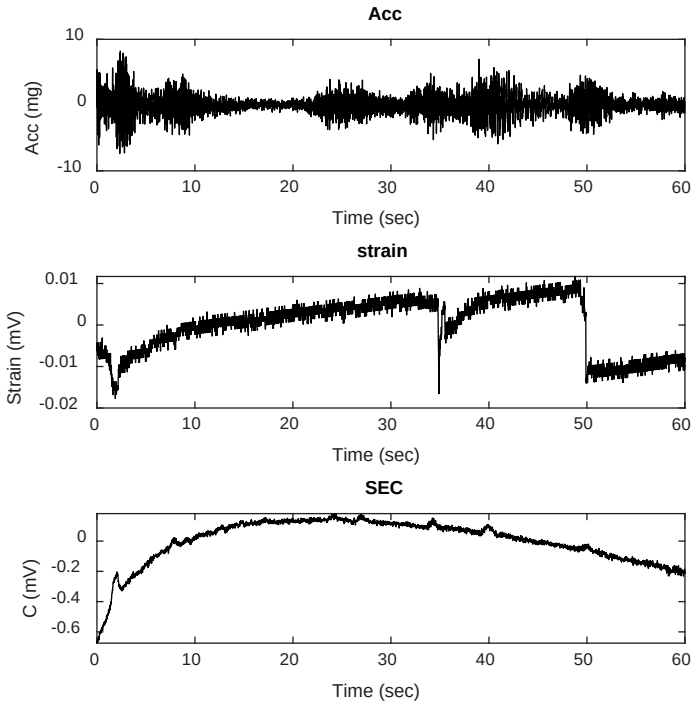

Figure 6.29: Typical Measurements from the Interior Side of the Girder
Top: Acceleration; Middle: Strain; Bottom: SEC

6.5.3 Crack Growth Index

Utilizing the method proposed in Chapter 3, Crack Growth Indices (CGIs) can be extracted from the field measurements of the SECs. For the SEC measurements in the exterior side of the girder, periodic responses exist in the measurements caused by the noise content. Extracting CGIs would be challenging as the SEC responses provoked by the traffic loads share similar frequency content with the noise. Further investigation is needed to address the challenge. Hence, in this subsection, only CGIs from the large SEC at the interior side of the girder are extracted.

Using the dataset mentioned in Section 6.5.2, the procedure of the CGI computation is briefly explained here. First, the power spectral densities (PSDs) of acceleration, strain, and SEC measurements are extracted. As shown in Figure 6.30, a peak is located in the higher frequency range of the PSD curve of the acceleration, while peaks in the PSDs of the strain and SEC are at lower frequency ranges. Note that these lower PSD peaks in the strain and SEC data are caused by the passing traffic loads and drifts in the time series signals.

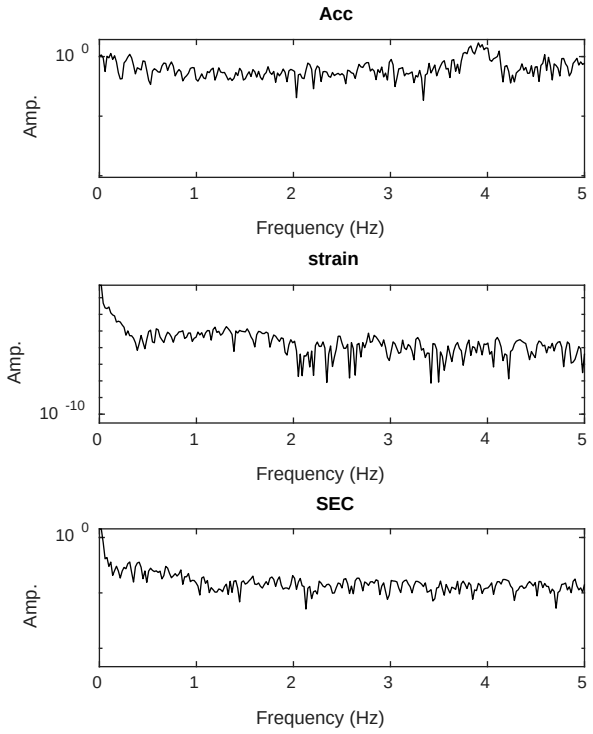

Figure 6.30: Power Spectral Densities (PSDs) of Acceleration, Strain, and SEC Measurements

To remove the effect of drifts, a cut-off window is applied to the PSD results of the strain and SEC measurements, respectively. The range of the cut-off window is from 0.2 Hz to 0.8 Hz. The cut-off window would keep the meaningful portion in the data caused by the passing traffic loads. In the meantime, the extremely low frequency content can be removed through the lower bound of the window. The PSD of strain and the SEC measurements after the cutoff are shown in Figure 6.31(a) and Figure 6.32(a), respectively. Next, a moving-average low-pass filter is further

applied to the PSD results, generating smoothed PSD curves so that the magnitude of PSD curves can be more accurately estimated. Results after applying the moving average filter can be seen in Figure 6.31(b) and Figure 6.32(b).

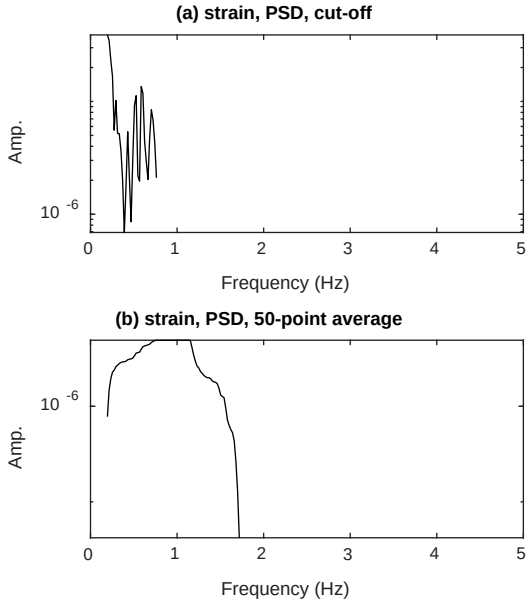

Figure 6.31: (a) PSD Result of the Strain Measurement After Cut-Off; (b) Result After Applying a Low Pass Filter

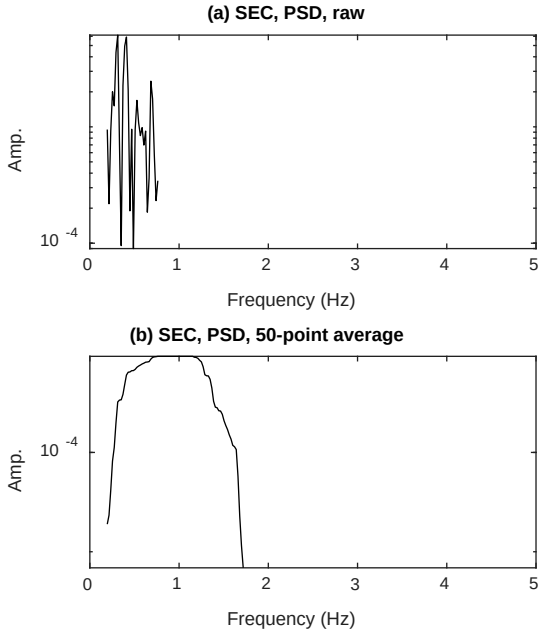

Figure 6.32: (a) PSD Result of the SEC Measurement After Cut-Off; (b) Result After Applying a Low Pass Filter

Once the filtered PSD curves of the strain and SEC measurements are obtained, the CGI can be calculated through the algorithm established in Chapter 3. Figure 6.33 shows the final CGI result of the large SEC. Notice that only the flat region around 1 Hz is meaningful, as this frequency range is corresponding to the passing traffic loads. In this regard, the CGI of the large SEC is about 14 for this particular dataset.

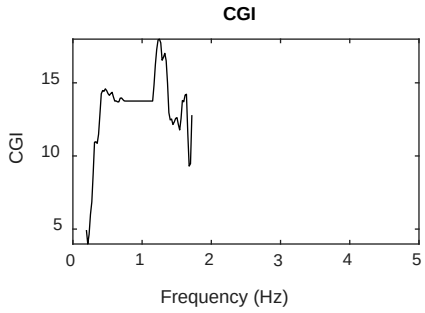

Figure 6.33: CGI of the Large SEC

6.5.4 Statistical Analysis of the Crack Growth Index

During the field visits on July 16th and 17th, 2018, a total of 817 datasets of the large SEC on the interior side of the girder were collected. Section 6.5.3 presents the CGI computation procedure for one dataset. Utilizing the same approach, the 817 datasets are processed to obtain the CGIs of all datasets. Figure 6.34 shows the CGI results where most CGIs have magnitudes around 20, while a few datasets produce significantly smaller or larger CGI values. The variation could be caused by the noise content and the low frequency drifts in the strain and SEC measurements.

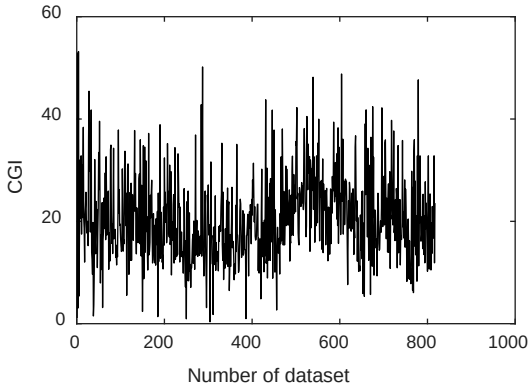

Figure 6.34: CGIs of All 817 Datasets of the Large SEC

Figure 6.35 shows the histogram of the CGIs presented in Figure 6.34. As can be seen in the figure, the majority of CGIs are between 10 and 30, with a mean value around 20. The result indicates that the proposed CGI approach is able to extract meaningful features from the field measurements. By continuing data collection in the field over long-term, it would be feasible to establish multiple histogram of CGIs at different data collection stages. The fatigue crack growth would be monitored through the change of histogram of the CGIs.

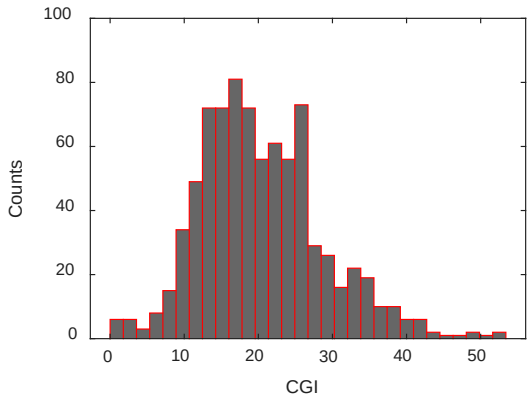

Figure 6.35: Histogram of CGI Results

6.6 Conclusions

In this chapter, the integrated fatigue crack monitoring system was deployed in the field. In particular, SECs were installed on both sides of a girder on a steel highway bridge for covering fatigue-susceptible regions. A strain gauge was installed on the cross frame in order to provide indirect loading information to normalize the SEC measurements. The system was powered by the wireless sensing platform Xnode for wirelessly transferring the field data to the base station. A number of datasets were collected from the field. The field data was processed to extract CGIs from the measurements, which is a fatigue-sensitive feature for indicating the crack growth over the long-term. While variation was observed in the CGIs, most CGIs of the large SEC collected from the field have values around 20. The findings in this chapter form the basis for long-term field monitoring of fatigue cracks in steel bridges.

Chapter 7 Conclusions and Recommendations

7.1 Conclusions

This report investigated fatigue crack detection of steel highway bridges through wireless elastomeric skin sensors. The report began with a literature review and a discussion on the issue of fatigue damage in steel highway bridges in the United States and the challenges for fatigue detection and inspection. The state-of-the-art fatigue crack sensing technologies and their limitations were also reviewed.

After the literature review, the report then focused on the SEC technology, which serves as the fundamental sensing unit of the wireless elastomeric skin sensor for fatigue crack monitoring. The investigation spanned from the theoretical sensing principle to the practical bridge engineering applications, including the following three aspects: (1) numerically simulating the response of the SEC under fatigue cracking; (2) developing and validating a long-term, robust crack-monitoring algorithm using the SEC through small-scale tests; and (3) large-scale validation for monitoring large fatigue susceptible regions through SEC arrays.

In terms of numerical study, a computational approach was established for numerically predicting the response of the SEC. Results validated that the proposed approach is able to simulate the capacitance response of the SEC under fatigue cracking with high accuracy. Using the developed numerical approach, the effect of changing the size of the SEC sensor on its ability to detect fatigue cracks was investigated. For the same crack size, smaller sensors are less sensitive in terms of peak-to-peak capacitance change, but more sensitive in terms of peak-to-peak percentage capacitance change. However, the coverage area may be greatly reduced by using a smaller sensor. The size of sensor therefore needs to be optimized to cover strategic areas at the desired resolution. The established approach directly links the signal of the sensor to a fatigue crack geometry, which will be very useful for infrastructure operators and managers in carrying out condition-based maintenance procedures.

In the development of the crack-monitoring algorithm, a novel sensing algorithm was developed through frequency analysis, which enabled a robust fatigue crack monitoring methodology that is insensitive to long-term signal drifts and varying fatigue loading characteristics. The proposed crack monitoring methodology was validated through a series of

small scale C(T) specimens subject to a series of high-cycle fatigue loadings. Results indicated the proposed method could robustly identify the fatigue crack growth under a variety of loading characteristics. The developed crack monitoring method would lead to more reliable fatigue monitoring over the long term.

In the large-scale experimental validation, a large-scale bridge-girder-to-cross-frame connection model was adopted for the investigation. An SEC array, coupled with a data visualization method for spatially representing the fatigue damage though CGIs was proposed to monitor the growth of fatigue damage over a large structural area. Experimental results validated that the proposed data visualization method could effectively identify the fatigue crack growth. The findings from the large-scale testing served as the basis for the field applications of the SEC technology on full-scale steel bridges.

Next, the research work was presented on developing a wireless capacitive sensor board to enable wireless sensing of the SEC sensors. The sensor board was developed by incorporating an AC Wheatstone bridge circuit, high-precision bridge balancer, two-step signal amplification, and AM demodulation with low-pass filtering. Using the developed sensor board, low-level dynamic capacitance variation of the SEC was successfully measured. A novel two-step shunt-calibration circuit was proposed, which enabled the calibration of the SEC capacitance variation without being affected by the lead wire induced error. In addition, utilizing the breakout box with some modifications, multi-channel sensing was successfully achieved using the Xnode. A series of lab validation tests were also performed to demonstrate the effectiveness of the developed capacitive sensor board.

Finally, we integrated the SEC technology with the wireless capacitive sensor board and validated the integrated monitoring system through a field deployment on a steel highway bridge. Six SECs were installed at two typical fatigue-susceptible locations in a web-gap region of the exterior steel girder. Data collected in the field showed that, through the trigger-based sensing mechanism, the wireless crack monitoring system was able to collect data continuously and autonomously from the SEC sensors and the strain gauge under the traffic loading. By processing the raw measurements using the proposed algorithm, CGIs of each monitored

location could be continuously collected and statistically monitored for long-term monitoring of fatigue cracks of steel bridges.

7.2 Recommendations for Future Work

Over the course of the project, while great success has been achieved in fulfilling the project objectives in terms of developing the integrated wireless skin sensor network and algorithms for continuous and autonomous fatigue crack monitoring, several further development needs were also identified to achieve more robust, accurate, and flexible crack monitoring. First, an improved understanding of the SEC sensor behavior under folded configuration is needed to strategically adjust the CGI algorithm when the SECs are attached to corners and joints. Second, the capacitance sensor board is currently based on analogy circuits, meaning the balancing and shunt calibration are performed manually. Converting the analog circuit to a digital one will enable software control and automation of these processes, hence greatly improving the efficiency and flexibility of the wireless sensing. Third, deployment of the sensor network at more diverse structural configurations and more extensive analyses of long-term field data are necessary to ensure adaptability of the proposed CGI algorithm.

References

Alavi, A. H., Hasni, H., Jiao, P., Borchani, W., & Lajnef, N. (2017). Fatigue cracking detection in steel bridge girders through a self-powered sensing concept. *Journal of Constructional Steel Research, 128*, 19-38.

American Society of Civil Engineers (ASCE). (2017). *2017 Infrastructure report card: Bridges*. Retrieved from https://www.infrastructurereportcard.org/wp-content/uploads/2017/01/Bridges-Final.pdf

ASTM E1820-15. (2015). *Standard test method for measurement of fracture toughness*. West Conshohocken, PA: ASTM International. doi: 10.1520/E1820-18, www.astm.org.

Bao, Y., Kunnath, S. K., El-Tawil, S., & Lew, H. S. (2008). Macromodel-based simulation of progressive collapse: RC frame structures. *Journal of Structural Engineering, 134*(7), 1079–1091.

Bennett, C., Matamoros, A., Barrett-Gonzalez, R., & Rolfe, S. (2014). *Enhancement of welded steel bridge girders susceptible to distortion-induced fatigue* (Report No. FHWA-KS-14-03; TPF-5[189]). Topeka, KS: Kansas Department of Transportation.

Biezma, M. V., & Schanack, F. (2007). Collapse of steel bridges. *Journal of Performance of Constructed Facilities, 21*(5), 398–405.

Blunt, D. M., & Keller, J. A. (2006). Detection of a fatigue crack in a UH-60A planet gear carrier using vibration analysis. *Mechanical Systems and Signal Processing, 20*(8), 2095–2111.

Cai, L., Song, L., Luan, P., Zhang, Q., Zhang, N., Gao, Q., … Xie, S. (2013). Super-stretchable, transparent carbon nanotube-based capacitive strain sensors for human motion detection. *Scientific Reports, 3*, 3048.

Connor, R. J., & Fisher, J. W. (2006). Identifying effective and ineffective retrofits for distortion fatigue cracking in steel bridges using field instrumentation. *Journal of Bridge Engineering, 11*(6), 745–752.

Dai, H., Thostenson, E. T., & Schumacher, T. (2015). Processing and characterization of a novel distributed strain sensor using carbon nanotube-based nonwoven composites. *Sensors, 15*(7), 17728–17747.

Dassault Systèmes. (2013). *Abaqus 6.13 user's manual*. Providence, RI: Author.

Dey, P. P., Chandra, S., & Gangopadhaya, S. (2006). Speed distribution curves under mixed traffic conditions. *Journal of Transportation Engineering, 132*(6), 475–481.

Downey, A., Laflamme, S., & Ubertini, F. (2016). Reconstruction of in-plane strain maps using hybrid dense sensor network composed of sensing skin. *Measurement Science and Technology, 27*(12), 124016.

Fisher, J. W. (1984). *Fatigue and fracture in steel bridges: Case studies*. New York, NY: Wiley.

Fu, Y., Hoang, T., Mechitov, K., Kim, J. R., Zhang, D., & Spencer, B. F., Jr. (2018). Sudden event monitoring of civil infrastructure using demand-based wireless smart sensors. *Sensors, 18*(12), 4480. https://doi.org/10.3390/s18124480

Fu, Y., Mechitov, K. A., Hoskere, V., & Spencer, B. F. (2016). Development of RTOS-based wireless SHM system: Benefits in applications. In *Transforming the future of infrastructure through smarter information: Proceedings of the International Conference on Smart Infrastructure and Construction, ICSIC 2016* (pp. 149–154). London, UK: ICE Publishing.

Fu, Y., Zhu, L., Hoang, T., Mechitov, K., & Spencer, B. F. (2018). Demand-based wireless smart sensors for earthquake monitoring of civil infrastructure. In *Sensors and smart structures technologies for civil, mechanical, and aerospace systems 2018*. Bellingham, WA: SPIE.

Ghahremani, K., Sadhu, A., Walbridge, S., & Narasimhan, S. (2013). Fatigue testing and structural health monitoring of retrofitted web stiffeners on steel highway bridges. *Transportation Research Record, 2360*, 27–35.

Glisic, B., & Inaudi, D. (2012). Development of method for in-service crack detection based on distributed fiber optic sensors. *Structural Health Monitoring, 11*(2), 161–171.

Gupta, S., & Ray, A. (2007). Real-time fatigue life estimation in mechanical structures. *Measurement Science and Technology, 18*(7), 1947–1958.

Haghani, R., Al-Emrani, M., & Heshmati, M. (2012). Fatigue-prone details in steel bridges. *Buildings, 2*(4), 456–476.

Haight, F. A., & Mosher, W. W., Jr. (1962). A practical method for improving the accuracy of vehicular speed distribution measurements. *Highway Research Board Bulletin, 341*, 92–116.

Holmberg, P. (1995). Automatic balancing of linear AC bridge circuits for capacitive sensor elements. *IEEE Transactions on Instrumentation and Measurement, 44*(3), 803–805.

Holusha, J., & Chang, K. (2007, August 2). Engineers see dangers in aging infrastructure. *The New York Times*. Retrieved from https://www.nytimes.com/2007/08/02/us/01cnd-engineer.html

Ihn, J.-B., & Chang, F.-K. (2004). Detection and monitoring of hidden fatigue crack growth using a built-in piezoelectric sensor/actuator network: I. Diagnostics. *Smart Materials and Structures, 13*(3), 609–620.

Jajich, D., & Schultz, A. E. (2003). Measurement and analysis of distortion-induced fatigue in multigirder steel bridges. *Journal of Bridge Engineering, 8*(2), 84–91.

Jang, S., Jo, H., Cho, S., Mechitov, K., Rice, J. A., Sim, S.-H., … Agha, G. (2010). Structural health monitoring of a cable-stayed bridge using smart sensor technology: Deployment and evaluation. *Smart Structures and Systems, 6*(5–6), 439–459.

Jo, H., Park, J.-W., Spencer, B. F., Jr., & Jung, H.-J. (2013). Develoment of high-sensitivity wireless strain sensor for structural health monitoring. *Smart Structures and Systems, 11*(5), 477–496.

Jo, H., Sim, S.-H., Nagayama, T., & Spencer, B. F., Jr. (2012). Development and application of high-sensitivity wireless smart sensors for decentralized stochastic modal identification. *Journal of Engineering Mechanics, 138*(6), 683–694.

Kang, I., Schulz, M. J., Kim, J. H., Shanov, V., & Shi, D. (2006). A carbon nanotube strain sensor for structural health monitoring. *Smart Materials and Structures, 15*(3), 737–749.

Kharroub, S., Laflamme, S., Song, C., Qiao, D., Phares, B., & Li, J. (2015). Smart sensing skin for detection and localization of fatigue cracks. *Smart Materials and Structures, 24*(6), 065004.

Kong, X., Li, J., Bennett, C., Collins, W., & Laflamme, S. (2016). Numerical simulation and experimental validation of a large-area capacitive strain sensor for fatigue crack monitoring. *Measurement Science and Technology, 27*(12), 124009.

Kong, X., Li, J., Bennett, C., Collins, W., Laflamme, S., & Jo, H. (2019). Thin-film sensor for fatigue crack sensing and monitoring in steel bridges under varying crack propagation rates and random traffic loads. *ASCE Journal of Aerospace Engineering, 32*(1). https://doi.org/10.1061/(ASCE)AS.1943-5525.0000940

Kong, X., Li, J., Collins, W., Bennett, C., Jo, H., Jeong, J.-H., & Laflamme, S. (2018). Dense capacitive sensor array for monitoring distortion-induced fatigue cracks in steel bridges. In *Sensors and smart structures technologies for civil, mechanical, and aerospace systems 2018*. Bellingham, WA: SPIE.

Kong, X., Li, J., Collins, W., Bennett, C., Laflamme, S., & Jo, H. (2017). A large-area strain sensing technology for monitoring fatigue cracks in steel bridges. *Smart Materials and Structures, 26*(8), 085024.

Kong, X., Li, J., Laflamme, S., & Bennett, C. (2015). *Fatigue crack monitoring using large-area, flexible capacitive strain sensors*. Paper presented at the Joint Conference of 6th International Conference on Advances in Experimental Structural Engineering (6AESE) and 11th International Workshop on Advanced Smart Materials and Smart Structures Technology (11ANCRiSST). University of Illinois at Urbana-Champaign, Urbana, IL.

Kong, X., Li, J., Laflamme, S., Bennett, C., & Matamoros, A. (2015). Characterization of a soft elastomeric capacitive strain sensor for fatigue crack monitoring. In *Sensors and smart structures technologies for civil, mechanical, and aerospace systems 2015*. Bellingham, WA: SPIE.

Kong, X., Shi, T., & Cheng, S. (2014). A numerical simulation method for steel structure collapsing under rare earthquake base on the material damage and failure law. *China Civil Engineering Journal, 47*(9), 38–44.

Laflamme, S., Kollosche, M., Connor, J. J., & Kofod, G. (2012). Robust flexible capacitive surface sensor for structural health monitoring applications. *Journal of Engineering Mechanics, 139*(7), 879–885.

Laflamme, S., Saleem, H. S., Vasan, B. K., Geiger, R. L., Chen, D. J., Kessler, M. R., & Rajan, K. (2013). Soft elastomeric capacitor network for strain sensing over large surfaces. In *IEEE/ASME Transactions on Mechatronics, 18*(6), 1647–1654.

Laflamme, S., Ubertini, F., Saleem, H., D'Alessandro, A., Downey, A. R. J., Ceylan, H, & Materazzi, A. L. (2014). Dynamic characterization of a soft elastomeric capacitor for structural health monitoring. *Journal of Structural Engineering, 141*(8).

Loh, K. J., Kim, J., Lynch, J. P., Kam, N. W. S., & Kotov, N. A. (2007). Multifunctional layer-by-layer carbon nanotube–polyelectrolyte thin films for strain and corrosion sensing. *Smart Materials and Structures, 16*(2), 429–438.

Lu, Q., Harvey, J., Le, T., Lea, J., Quinley, R., Redo, D., & Avis, J. (2002). *Truck traffic analysis using weigh-in-motion (WIM) data in California* (Report No. UCPRC-RR-2002-01). Berkeley, CA: University of California, Berkeley.

Mantenuto, P., De Marcellis, A., & Ferri, G. (2014). Novel modified De-Sauty autobalancing bridge-based analog interfaces for wide-range capacitive sensor applications. *IEEE Sensors Journal, 14*(5), 1664–1672.

McLean, J. R. (1979). Observed speed distributions and rural road traffic operations. In *Proceedings from the Ninth Australian Road Research Board Conference, Brisbane, August 21-25, 1978* (Part 5, pp. 235-244). Vermont South, Victoria, AU: Australian Road Research Board.

Mohammad, I., & Huang, H. (2010). Monitoring fatigue crack growth and opening using antenna sensors. *Smart Materials and Structures, 19*(5), 055023.

Moreu, F., Jo, H., Li, J., Kim, R. E., Cho, S., Kimmle, A., … LaFave, J. M. (2015). Dynamic assessment of timber railroad bridges using displacements. *Journal of Bridge Engineering, 20*(10), 04014114.

Moreu, F., Li, J., Jo, H., Kim, R. E., Scola, S., Spencer, B. F., & LaFave, J. M. (2016). Reference-free displacements for condition assessment of timber railroad bridges. *Journal of Bridge Engineering, 21*(2), 04015052.

Movahhedy, M., Gadala, M. S., & Altintas, Y. (2000). Simulation of the orthogonal metal cutting process using an arbitrary Lagrangian–Eulerian finite-element method. *Journal of Materials Processing Technology, 103*(2), 267–275.

National Bridge Inspection Standards, 69 Fed. Reg. 74419 (Dec. 14, 2004) (to be codified at 23 CFR Part 650).

Roberts, T. M., & Talebzadeh, M. (2003). Acoustic emission monitoring of fatigue crack propagation. *Journal of Constructional Steel Research, 59*(6), 695–712.

Saleem, H., Downey, A., Laflamme, S., Kollosche, M., & Ubertini, F. (2015). Investigation of dynamic properties of a novel capacitive-based sensing skin for nondestructive testing. *Materials Evaluation, 73*(10), 1384–1391.

Saxena, A., & Hudak, S. J., Jr. (1978). Review and extension of compliance information for common crack growth specimens. *International Journal of Fracture, 14*(5), 453–468.

Sim, S.-H., Spencer, B. F., Jr., Jo, H., & Carbonell-Márquez, J. F. (2011). Decentralized random decrement technique for data aggregation and system identification in wireless smart sensor networks. In *IUTAM Symposium on Nonlinear Stochastic Dynamics and Control* (pp. 305-314). Dordrecht, Netherlands: Springer.

Simonsen, B. C., & Törnqvist, R. (2004). Experimental and numerical modelling of ductile crack propagation in large-scale shell structures. *Marine Structures, 17*(1), 1–27.

Song, J.-H., Wang, H., & Belytschko, T. (2008). A comparative study on finite element methods for dynamic fracture. *Computational Mechanics, 42*(2), 239–250.

Spencer, B. F., Jr., Park, J.-W., Mechitov, K. A., Jo, H., & Agha, G. (2017). Next generation wireless smart sensors toward sustainable civil infrastructure. *Procedia Engineering, 171*, 5–13.

Spencer, B. F., Jr., Ruiz-Sandoval, M. E., & Kurata, N. (2004). Smart sensing technology: opportunities and challenges. *Structural Control and Health Monitoring, 11*(4), 349–368.

Staszewski, W. J., Lee, B. C., & Traynor, R. (2007). Fatigue crack detection in metallic structures with Lamb waves and 3D laser vibrometry. *Measurement Science and Technology, 18*(3), 727–739.

Tikka, J., Hedman, R., & Siljander, A. (2003). Strain gauge capabilities in crack detection. In *Structural Health Monitoring 2003: From Diagnostics & Prognostics to Structural Health Management* (pp. 812-819). Lancaster, PA: DEStech Publications, Inc.

Ubertini, F., Laflamme, S., Ceylan, H., Materazzi, A. L., Cerni, G., Saleem, H., … Corradini, A. (2014). Novel nanocomposite technologies for dynamic monitoring of structures: a comparison between cement-based embeddable and soft elastomeric surface sensors. *Smart Materials and Structures, 23*(4), 045023.

Vrouwenvelder, A. C. W. M., & Waarts, P. H. (1993). Traffic loads on bridges. *Structural Engineering International, 3*(3), 169–177.

Yao, Y., & Glisic, B. (2015). Detection of steel fatigue cracks with strain sensing sheets based on large area electronics. *Sensors, 15*(4), 8088−8108.

Yazdi, N. A., Kulah, H., & Najafi, K. (2004). Precision readout circuits for capacitive microaccelerometers. In *Proceedings of the IEEE Sensors 2004* (pp. 28–31). Piscataway, NJ: Institute of Electrical and Electronics Engineers, Inc.

Yi, X., Cho, C., Cooper, J., Wang, Y., Tentzeris, M. M., & Leon, R. T. (2013). Passive wireless antenna sensor for strain and crack sensing – Electromagnetic modeling, simulation, and testing. *Smart Materials and Structures, 22*(8), 085009.

Yu, D., Bennett, C., & Matamoros, A. (2017). Retrofitting distortion-induced fatigue in skewed girders to cross-frame connections. In *Structures Congress 2017: Bridges and Transportation Structures* (pp. 149–161). Reston, VA: American Society of Civil Engineers.

Yu, J., Ziehl, P., Matta, F., & Pollock, A. (2013). Acoustic emission detection of fatigue damage in cruciform welded joints. *Journal of Constructional Steel Research, 86*, 85–91.

Zhao, Y., & Roddis, W. M. K. (2004). *Fatigue prone steel bridge details: Investigation and recommended repairs* (Report No. K-TRAN: KU-99-2). Topeka, KS: Kansas Department of Transportation.

Zhao, Z., & Haldar, A. (1996). Bridge fatigue damage evaluation and updating using non-destructive inspections. *Engineering Fracture Mechanics, 53*(5), 775-788.

AD ASTRA PER ASPERA

Kansas

Department of Transportation